Title
Fundamental Mechanisms of Load Transfer in the Human Vertebral Body Following Lumbar Total Disc Arthroplasty

Author
Bonnheim, Noah

Publication Date
2020

Peer reviewed|Thesis/dissertation

Fundamental Mechanisms of Load Transfer in the Human Vertebral Body Following Lumbar Total Disc Arthroplasty

by

Noah Bonnheim

A dissertation submitted in partial satisfaction of the

requirements for the degree of

Doctor of Philosophy

in

Engineering — Mechanical Engineering

in the

Graduate Division

of the

University of California, Berkeley

Committee in charge:

Professor Tony M. Keaveny, Chair
Professor Lisa A. Pruitt, Co-chair
Professor Grace D. O'Connell
Professor Thomas J. Carlson

Summer 2020

Fundamental Mechanisms of Load Transfer in the Human Vertebral Body Following Lumbar Total Disc Arthroplasty

by

Noah Bonnheim

Abstract

Fundamental Mechanisms of Load Transfer in the Human Vertebral Body Following Lumbar Total Disc Arthroplasty

by

Noah Bonnheim

Doctor of Philosophy in Mechanical Engineering

University of California, Berkeley

Professor Tony M. Keaveny, Chair
Professor Lisa A. Pruitt, Co-Chair

The overall goal of this research is to provide insight into the bone biomechanics of human lumbar vertebrae implanted with total disc arthroplasty (TDA) implants. The research elucidates fundamental mechanisms by which lumbar TDA implants alter the yield strength of the vertebral body, stress in the bone tissue, and trabecular-cortical load-sharing behavior. The findings could have broad clinical and scientific implications related to pre-operative assessment of bone quality, *in vitro* test protocols for device development and regulation, the development of new implant designs, and clinical exclusion criteria. Ultimately, the hope is that this insight can be used to improve clinical outcomes for this class of device, and, in turn, contribute to the broad effort of addressing the global health burden associated with degenerative spinal pathologies.

This dissertation comprises a series of computational experiments conducted on human cadaveric lumbar vertebrae using a combination of high-resolution micro-computed tomography image data with parallel linear and nonlinear finite element analysis implemented on a peta-scale supercomputing cluster. The goals of these studies are to assess mechanisms of load transfer and stress development in the bone, including how tissue-level stress depends on the loading mode of the implant, its size and material characteristics, and inter-individual variations in the structural features of the vertebral body.

The primary results indicate that the load-transfer behavior in the underlying vertebral bone is substantially altered by TDA, causing high levels of trabecular bone stress, diminishing the role of the cortical shell, and substantially reducing the whole-bone yield strength. These findings were assessed in relationship to the vertebral bone's morphology and microstructure, enabling mechanistic insight into bone sub-failure and failure behavior. A key finding was that small declines in trabecular bone volume fraction can have a magnified effect on whole-bone yield strength following TDA; therefore, pre-operative assessment of bone quality should optimally focus on the trabecular centrum.

Another important finding was that when the footplate of a TDA implant is loaded through its anterior or posterior rim, representing load-transfer into the bone following impingement induced by flexion or extension, bone stress near the impinged region increases substantially. This

localized stress increase causes a reduction in whole-bone yield strength, suggesting that subsidence might be caused, in some cases, by impingement-type loading. Pre-clinical subsidence testing of TDA implants should therefore include some form of evaluation of bending-induced impingement if the implant enables this type of loading *in vivo*. As a possible strategy to help reduce the risk of implant subsidence, future research might be directed at whether an implant could be designed to reduce the frequency or strength-reduction effects of impingement loading.

In closing, this dissertation elucidates fundamental mechanisms by which the vertebral bone tissue resists the loads applied by lumbar TDA implants. This mechanistic insight was used to identified possible targets—including pre-clinical tests and implant design considerations—that might help to improve clinical outcomes for this class of device.

To Professor James Fleming at Colby College,
who first introduced me to the practice and pleasure of research.

Table of Contents

Abstract ---------- 1
Table of Contents ---------- ii
List of Figures ---------- iv
List of Tables ---------- vi
Acknowledgements ---------- vii
1. Introduction ---------- 1
1.1 Disc degeneration and degenerative disc disease ---------- 2
1.2 Surgical intervention for end-stage degenerative disc disease ---------- 3
1.3 TDA to preserve segmental motion ---------- 4
1.4 Impingement ---------- 6
1.5 The composition, structure, and mechanics of bone tissue ---------- 6
1.5 The vertebral body ---------- 8
1.6 Micro-computed-tomography-based finite element modeling ---------- 8
1.7 Objectives and scope of the dissertation ---------- 10
2. The effects of implant size and stiffness on trabecular-cortical load-sharing behavior and tissue-level stress ---------- 21
2.1 Introduction ---------- 21
2.2 Methods ---------- 21
2.3 Results ---------- 24
2.4 Discussion ---------- 25
3. The role of bone porosity and loading mode on tissue-level stress in the human vertebral body following lumbar total disc arthroplasty ---------- 36
3.1 Introduction ---------- 36
3.2 Methods ---------- 37
3.3 Results ---------- 39
3.4 Discussion ---------- 40
4. The role of bone microstructure and loading mode on vertebral strength following lumbar total disc arthroplasty ---------- 48
4.1 Introduction ---------- 48
4.2 Methods ---------- 49
4.3 Results ---------- 51
4.4 Discussion ---------- 52

5. Conclusions----------64
6. Works Cited ----------67
7. Appendix----------82
7.1 Assessing the impact of a higher fidelity implant model on load-sharing outcomes (Chapter 2)----------82
7.2 Assessing the sensitivity of load-sharing outcomes to uncertainties in bone tissue elastic modulus (Chapter 2) ----------82
7.3 Assessing the impact of a higher fidelity implant model on the maximum stress levels (Chapter 3)----------82
7.4 Assessing the sensitivity of the maximum stress levels to uncertainties in bone tissue elastic modulus (Chapter 3) ----------82
7.5 Estimating QCT-measured volumetric bone mineral density from micro-CT-measured trabecular bone volume fraction (Chapter 3)----------83
7.6 Assessing the impact of a higher fidelity implant model on yield strength predictions (Chapter 4)----------83
7.7 Assessing the impact of finite element size on yield strength predictions (Chapter 4)-83
7.8 Assessing the impact of modeling an intervertebral disc instead of PMMA on yield strength predictions (Chapter 4) ----------84
7.9 Experimental data supporting the validity of the micro-CT-based finite element approach ----------84

List of Figures

Figure 1–1 Modern lumbar disc replacements----------13

Figure 1–2 Lateral radiograph showing implant subsidence into the vertebral body----------14

Figure 1–3 Lateral radiograph and retrieval photograph demonstrating impingement induced by flexion and extension----------15

Figure 1–4 Retrieved polyethylene inserts showing severe damage caused by impingement loading----------16

Figure 1–5 The hierarchical structure of bone tissue----------17

Figure 1–6 Typical stress-strain curve of cortical bone tissue----------18

Figure 1–7 Transverse and sagittal cross-sections of a human lumbar vertebral body as imaged with micro-computed tomography----------19

Figure 1–8 Axial stress within the trabecular tissue as computed from micro-CT-based finite element analysis----------20

Figure 2–1 Mid-sagittal cross-section showing boundary conditions and displaced shapes for the intact disc in compression and flexion, as well as the implant in compression and flexion----------30

Figure 2–2 Flexion of an implanted segment was modeled by applying a force through an arc, simulating impingement----------31

Figure 2–3 The cortical load fraction and relative high-risk tissue volume for compression and flexion along the axial and anterior-posterior directions, respectively----------32

Figure 2–4 Minimum principal stress in the bone tissue at a mid-sagittal cross section for the intact disc and metallic implant models in compression and flexion----------33

Figure 2–5 The 98th percentile of minimum principal stress in the bone tissue by compartment (trabecular, cortical, and endplate)----------34

Figure 2–6 Mid-sagittal cross-section showing the percent difference in von Mises stress between the intact disc model and implant models----------35

Figure 3–1 Mid-sagittal cross-section showing boundary conditions and displaced shapes for implanted and intact models in compression and flexion----------45

Figure 3–2 Maximum stress level as a function of trabecular bone volume fraction----------46

Figure 3–3 Mid-sagittal cross-section showing the spatial distribution of high-risk tissue for each loading mode (compression, flexion, and extension) for a model loaded via a TDA implant and an intervertebral disc----------47

Figure 4–1 Boundary conditions used to calculate vertebral yield strength when loaded via an implant and via PMMA----------58

Figure 4–2 Representative force-apparent strain curve for one vertebra loaded via an implant and via a TDA implant in compression----------59

Figure 4–3 Yield strength as a function of loading mode and the mean reduction in yield strength for the models loaded via a TDA implant in compression, flexion-, and extension-induced impingement relative to the same models loaded via PMMA in compression----------60

Figure 4–4 Yield strength and yield strength change as a function of bone microarchitectural parameters----------62

Figure 4–5 Results from stepwise linear regression analysis showing the combined effects of microarchitectural metrics on the predicted yield strength and yield strength reduction----------63

Figure 7–1 The cortical load fraction and high-risk tissue volume were not sensitive to the choice of tissue material properties within a realistic physiologic range, or the addition of small implant protrusions----------85

Figure 7–2 Data collected by others demonstrating that the specialized micro-CT based finite element approach used here accurately predicted experimentally-measured strength of human thoracic vertebrae, proximal femurs, and trabecular bone cores from across anatomic sites----------86

List of Tables

Table 1–1 The contraindications to TDA cited in clinical studies----------12

Table 3–1 Sample demographic data (n = 12) and implant sizes----------44

Table 4–1 Sample demographic data (n = 12), bone morphologic and microarchitectural parameters, and computed yield strength results----------57

Table 4–2 The Pearson correlation coefficient quantifying the independent associations between the computed yield strength with age, bone mineral content, and bone microarchitectural parameters----------61

Acknowledgements

First and foremost, I would like to thank my research advisors, Professors Tony Keaveny and Lisa Pruitt, for their mentorship during my time at Berkeley. Professor Keaveny's guidance in identifying key conceptual questions and insights—from the highest levels of problem-identification to the finer points of data interpretation and writing—have provided invaluable wisdom that will inform my thinking for years to come. His direct yet kind style of questioning, enthusiasm for research, and good humor also helped to deepen my thinking while keeping things fun along the way. Professor Pruitt's unconditional support during my years-long exploration of various research topics enabled me to clarify my interests and provided a foundation upon which to build. Her lab will always feel like home base.

I also owe thanks to Professors Grace O'Connell and Thomas Carlson. When I arrived at Berkeley, Professor O'Connell's lab provided my initial exposure to the mechanical behavior of the intervertebral disc and the spinal motion segment; that early work was instrumental in my education and informs many aspects of this dissertation. Professor Carlson's anatomy course was also helpful and enjoyable—both times I took it.

I'm indebted to the research team that developed the finite element framework *Olympus*, upon which this dissertation is built. The continued relevance of the *Olympus* code after nearly two decades is a testament to their ingenuity. In particular, I owe a great deal of thanks to Dr. Mark Adams who patiently guided me through the debugging process and whose work has enabled this research and that of many others. Likewise, my research would not have been possible without the computational resources and technical support funded by XSEDE and provided by the Texas Advanced Computing Center at the University of Texas at Austin (the virtual portal to Texas also felt a little bit like visiting home).

My colleagues in the Orthopedic Biomechanics Lab and Medical Polymer Group were a joy to work with—leaving this community makes completing my dissertation bittersweet. I especially want to thank Dr. Saghi Sadoughi, Dr. Farzana Ansari, and Tongge Wu for their close collaboration and friendship. Giuliana Davis and Shannon Emerzian were also terrific peers and friends whom I will miss.

I would like also to thank my parents for instilling in me a curiosity which has added immeasurable richness to my life. My siblings, in-laws, nephews, and niece—Ana and Asher, Julia and Marc, Laura and Paco, John and Lisa, Anne and Bill, Micah and Jonas, and Asa and Zoe—filled the time spent away from this dissertation with emotional nourishment.

Finally, I owe thanks to my wife, Hannah, who helped show me that a PhD was both possible and far less important than other things. It's fitting that the final sentences of this dissertation are being written on our one-year anniversary; both marking a present accomplishment and pointing to an exciting future.

1. Introduction

Spinal pathologies cause substantial pain and disability worldwide. A recent study calculated that over 3% of the world's population (266 million individuals) likely suffer from a degenerative spinal disease such as degenerative disc disease, spondylolisthesis, or spinal stenosis each year [1]. Data from the Global Burden of Disease 2017 study indicate that low back pain (for any reason) is the leading cause of years lived with disability globally and in 13 of 21 world regions [2]. Lumbar degenerative disc disease is the most common diagnosis prior to spinal fusion surgery, which has associated hospital charges of roughly $34 billion each year in the United States alone [3]. The prevalence of degenerative spinal pathologies may grow in association with an aging population: the proportion of the world's population aged 60 years and older is expected to double by 2050 [4].

The critical global health burden associated with degenerative spinal diseases is due in part to limited understanding of the pathologies themselves and in part due to limitations in the efficacy and availability of clinical treatment [5]. Research is therefore required on at least two fronts: one to uncover the mechanisms of disease behavior and another to develop and refine treatments to improve clinical outcomes. Broadly, this dissertation aims to contribute to the latter by elucidating fundamental biomechanical behavior of the vertebral bone supporting a lumbar total disc arthroplasty (TDA) implant, a surgical treatment for severe disc degeneration. The overall goal of this work is to provide insight into the bone biomechanics of TDA-implanted vertebrae, which in turn could motivate new implant designs and *in vitro* test protocols for device development and regulation, identify pre-operative assessment criteria, clarify appropriate clinical indications, and ultimately help improve clinical outcomes for this class of device.

Lumbar total disc arthroplasty (TDA) is intended to alleviate pain and restore compromised function associated with end-stage disc degeneration [6]. The procedure was developed as an alternative to spinal fusion (one of the most prevalent and costly orthopedic surgeries [3]), due to concerns related to fusion-induced damage to surrounding tissues. In contrast to the rigid union of vertebral bodies induced by a fusion surgery, the intent of TDA is to restore physiologic patterns of load-transfer by permitting relative motion between adjacent vertebral bodies [7].

Modern TDA implants have been implanted by spine surgeons in Europe since the 1980s and the United States since the 1990s with mixed clinical success [6]. Problems including implant subsidence [8–11], dislocation [12–14], heterotopic ossification [15–19], and adjacent-level vertebral fracture [9,20–24] have limited clinical efficacy in many cases and provoked substantial contra-indications to TDA (Table 1–1) [25]. For example, the majority of fusion patients (> 90 % according to some studies [26–28]) have at least one contraindication to TDA; this suggests that TDA may not substantially improve the long-term outcomes for those patients otherwise requiring a fusion, at least with current device designs and surgical techniques. However, there is also evidence, including meta-analyses [29–31], that TDA measurably improves pain and disability scores relative to fusion, suggesting that TDA may yet be a promising approach to address fusion's limitations, provided the aforementioned clinical problems (such as subsidence, fracture, etc.) can be addressed.

However, little information exists on how TDA implants affect the bone biomechanics within the vertebral body supporting an implant, representing a barrier to the development of devices that reduce the risk of complications such as subsidence. Unanswered questions include: How does the stress in the underlying vertebral bone tissue change as a function of implant size or material? How does the development of high bone stress depend on the loading mode of the implant (e.g. compression versus bending), or on typical inter-individual variations in the porosity of the vertebral body? Finally, does the presence or loading mode of an implant alter the overall yield strength of the vertebral body; and, if so, what morphological features (for example, the overall bone mineral content or relative mass of the cortical shell) are associated with a reduction in yield strength? This dissertation attempts to address each of these questions via a series of experiments utilizing high-resolution imaging of cadaveric human lumbar vertebrae coupled with linear and nonlinear finite element analysis, solved in parallel on a high-performance supercomputing cluster.

The remainder of this chapter helps contextualize the overall dissertation research by providing more background information related to degenerative disc disease, fusion, TDA, the properties of bone tissue and the vertebral body, and the method of experimental investigation: micro-computed tomography- (micro-CT-) based finite element analysis. The section concludes by defining the objectives and scope of the dissertation.

1.1 Disc degeneration and degenerative disc disease

Changes to the intervertebral discs separating the vertebra of the spine occur in most people as they age [32]. Normal age-related changes include a diminished ability of the disc to retain water, thus inhibiting the development of the hydrostatic pressure essential to the disc's biomechanical function [33]. Specifically, a hydrostatic pressure—occurring primarily within the disc's nucleus—helps prevent buckling of the annulus, maintains separation between vertebral bodies, and evenly distributes load to them [33–35]. Thus, age-related changes can cause both a gradual loss in disc height and alter the way in which load is transferred to underlying bone. In middle age, for example, disc height typically declines by approximately 0.6% per year [36] while vertebral body load-transfer increasingly occurs through the disc's periphery, via the annulus instead of the nucleus [33,34].

Mechanistically, these changes are caused by increased disc-cell senescence and related biochemical changes in the disc's extracellular matrix [35,37]. At the cellular level, the cause of deterioration is not known with certainty but could be precipitated by structural damage from mechanical loads [34,38]. Regardless of the cause, the cells of aged discs cannot synthesize extracellular matrix as effectively as those of younger ones; thus, over time, the hydrophilic proteoglycan chains comprising the extracellular matrix become fragmented, reducing the ability of the nucleus to retain water [39]. Collagen molecules and fibrils within the disc's extracellular matrix also become increasingly crosslinked with time for two reasons: 1) reduced matrix turnover enables crosslinks to develop and stabilize and 2) the interaction between collagen and glucose can cause non-enzymatic crosslinks to accumulate (i.e. advanced glycation end products [AGEs]) [34,35]. These biochemical changes are thought to embrittle the disc tissue and cause structural defects beginning as early as the second decade of life [34,40].

The extent and effect of disc degeneration among the adult population is highly variable. By age sixty-five, nearly all adults likely demonstrate the aforementioned changes to the disc to some degree, as measured by magnetic resonance imaging (MRI) [32]. Age is a primary factor predicting the presence or absence of degenerative changes, yet adults of any age can exhibit degenerative changes with a range of severity [41]. Aside from age, studies using identical twins suggest that heredity can explain a signification portion (50–70%) of the variation in disc degeneration among adults [41,42].

Degeneration of the discs does not imply pain or other symptoms. Severe radiographic degeneration of the lumbar discs is associated with a two-fold increase in the odds of suffering from chronic low back pain [32]; however, radiographic pathology does not explain pain intensity. For those with discogenic chronic low back pain, the severity of disc degeneration (as measured by MRI) is not necessarily associated with the severity of pain [32,43]. This suggests that the nature of discogenic pain is not fully explained by disc degeneration and limits the utility of radiography in the clinical assessment of pain.

The degenerative structural changes in the disc can also lead to gross injury including annular tears and nuclear prolapse (herniation) [34]. These events can be painful and can affect neurologic function [44]. Both degeneration itself and gross injury to the disc can cause instability (a kinematic response under a given physiologic load in excess of the response found in the healthy condition [45]), which can contribute to the degenerative process. Patients with asymptomatic degenerate discs are not necessarily considered to have a pathology: degenerative disc disease refers only to pathological changes such as advanced structural failure coupled with discogenic pain [34]. The pain associated with degenerative disc disease often requires medical intervention.

1.2 Surgical intervention for end-stage degenerative disc disease

A primary treatment for end-stage degenerative disc disease—that is, a treatment frequently suggested when non-surgical treatments such physical therapy have not adequately alleviated pain—involves removing the disc and fusing the adjacent vertebral bodies [46]. Once the disc is excised, a fusion procedure involves the implantation of a “cage” seeded with osteogenic material derived either from a patient’s own living bone cells (for example, harvested from a patient’s ilium) or from bone morphogenic proteins derived from recombinant DNA [47–49]. The cage is designed for two primary purposes: to provide stability and vertebral body separation in the immediate post-operative period; and to serve as a scaffold for the eventual bony union of the vertebral bodies (arthrodesis), which takes three to six months [47,49]. Metal rods and screws are often used to bridge the pedicles of adjacent vertebrae to provide an additional route of load transfer, further stabilizing the motion segment [50]. The goal of fusion in the treatment of degenerative disc disease is to eliminate relative motion between spinal structures, thereby alleviating pain cause by nerve compression [47,51].

Like disc degeneration itself, the effects of fusion are variable. In a review of randomized controlled trials, Mirza et al [52] found that lumbar fusion was not measurably more effective than structured rehabilitation coupled with psychotherapy in the treatment of discogenic back pain. Mannion et al [53] reviewed different randomized controlled trials and reached the same

conclusion. Surgical indication may, in part, explain why fusion appears to benefit some patients more than others. A meta-analysis by Yavin et al [54] found that fusion was particularly beneficial in the treatment of spondylolisthesis but less effective for other degenerative conditions. In a study on 58 patients who received a lumbar fusion for degenerative disc disease and were followed for a minimum of two years, Moore et al [55] concluded that the return-to-work rate (88%), reduction in narcotic use (29%), and frequency of pain improvement (86%) post fusion justified the procedure's continued use. However, despite a 95% rate of radiographic arthrodesis in that study, nearly 20% of patients required long-term narcotic use for back pain and 14% had either the same or worse pain severity following fusion. The same study also indicated that arthrodesis—the surgical goal of fusion—does not necessarily address its clinical goal of alleviating pain [55]. Overall, there is no consensus on the use of lumbar fusion in the treatment of degenerative disc disease; some authors describe the procedure as justifiable, while others describe the risks to the patient as being unacceptable in light of variable long-term clinical outcomes and high rates of complication and revision [5,56].

The controversy regarding fusion in the treatment of degenerative disc disease is related, in large part, to fundamental biomechanical behavior of the fused spine. In particular, fusion at one level can cause a compensatory increase in motion at adjacent levels; this has been demonstrated in cadaveric, radiographic, and computational experiments [57–59]. The increase in adjacent-segment motion is associated with higher loads in the adjacent tissues [57,59–63]; for example, the pressure within the intervertebral discs adjacent to a fusion has been shown to increase in proportion to the number of segments fused [57,60]. It's hypothesized that, following fusion, an increase in motion and load might exceed the healthy physiologic range, and therefore accelerate degeneration at adjacent levels. This phenomenon has been termed adjacent-segment disease and has been extensively documented in the literature [61,62].

Despite the established biomechanical changes following fusion, it's unclear whether adjacent-segment disease is iatrogenically induced or the result of natural disease progression; in other words, the adjacent discs may degenerate regardless of a fusion. Discriminating the factors causing adjacent-segment disease has proven difficult since the typical fusion patient has both elevated adjacent-segment motion and a pre-existing, genetically-moderated musculoskeletal disease (such as degenerative disc disease), thus confounding the issue [62]. The clinical implications of adjacent segment disease are also a topic of controversy. It has been suggested that the adjacent segments degeneration at an accelerated rate may not necessarily alter patient outcomes [64].

Though the extent and clinical sequelae of adjacent-segment disease are not known with certainty, the variable long-term clinical outcomes of fusion and the numerous meta-analyses and randomized trials showing its limited efficacy compared to non-surgical options has motivated interest in alternative treatments to degenerative disc disease. Particular attention has been given to those approaches which preserve segmental motion and therefore, in theory, better replicate the motion and load-transfer patterns of the healthy spine.

1.3 TDA to preserve segmental motion

Total disc arthroplasty (TDA, also referred to as total disc replacement or artificial disc replacement) is a surgical treatment for degenerative disc disease that involves removing the native intervertebral disc at the painful level and replacing it with a prosthetic component. The objective of this approach is for the implant to partially replicate the primary biomechanical functions of the healthy disc; that is, maintain vertebral-body separation (disc height), provide segmental stability, and enable typical levels of relative motion between adjacent vertebrae [7,65–70]. These functional objectives must be accomplished while also protecting the facet joints from unusually high stress, since injury to or degeneration of the fact joints can be painful and debilitating, and TDA can alter facet-joint forces [67,71,72]. The overall rationale of TDA is that, if the implant enables a pseudo-physiologic pattern of segmental motion, then it should generate pseudo-physiologic levels of stress in the surrounding hard and soft tissues, and should not, therefore, accelerate adjacent segment disc disease [68–70].

The functional objectives of TDA have inspired many approaches to implant design. The first TDA devices, implanted in the 1950s and 1960s, were monobloc spheres cast from stainless steel or vitallium: these simple metal balls were effective in some patients, but frequently subsided (displaced into the underlying vertebral body) [6,65,73]. Little development occurred for the next two decades, until surgeons at the Charité Hospital in East Berlin developed the SB Charité implant circa 1982 [6,74]. Unlike the monobloc metal balls, the SB Charité was comprised of three components: two metal footplates with a central spherical cavity, separated by a convex spherical ultra-high-molecular-weight (UHMWPE) insert (Figure 1–1A). The design philosophy of the SB Charité was that the metal-on-UHMWPE articulation would replicate the joint-level kinematic behavior of the native anatomy, similar to total knee and hip replacements [75]. While other implant approaches have also been described and developed, including elastomeric interbody devices [76,77], multi-component articulated designs are typical of modern implants (Figure 1–1).

Despite the theoretical advantages with respect to adjacent segment degeneration and substantial enthusiasm for the approach [78], TDA has not been widely adopted. In 2004, it was estimated that within five years TDA would replace nearly 50% of the fusion market [78]; however, in reality, procedure volume declined from 3,650 cases in 2005 to 1,863 cases in 2010 [79]. In part, this “failure to launch” (as one author put it [79]) may relate to the extensive contraindications to TDA (Table 1–1) [25,28]. These contraindications, in part, relate to the implant’s biomechanics (for example, patients with low bone density are contraindicated for TDA due to concerns that the implant will subside or fracture the vertebral bone [25]).

Clinical results following lumbar TDA are mixed. A number of meta-analyses based on randomized controlled trials indicate that TDA is safe, effective, and non-inferior or superior to fusion two years post-operatively with respect to outcomes including patient satisfaction, level of pain, and level of disability [30,80–83]. A comprehensive meta-analysis that included robust treatment of bias [30] found a statistically significant benefit of TDA relative to fusion at a follow-up of two years; however, the magnitude of the benefit (< 5% change in Oswestry Disability Index) did not meet the pre-defined threshold for clinical relevance. A meta-analysis by Yajun et al [81] found a measurable benefit for TDA relative to fusion at a follow-up of two years but outcomes were equivalent after five years, consistent with other data [31]. Fewer data are available for follow-up periods greater than five years. Tropiano et al [84] found that 75%

(41/55) of TDA patients had good or excellent results after 7–11 years, though the remaining 25% (14/55) had poor clinical results. Siepe et al [85] found that 64% (115/181) of patients were highly satisfied after 5–10 years with an overall complication rate of 14% (26/181). Lu et al [10] recently published a study reporting 15 year follow-up data for 30 patients, finding that levels of pain and disability were significantly lower than pre-operative levels in 93% of patients. Those authors also found a prevalence of subsidence of 11% [10]. A study on 53 patients with an average follow-up of 17 years [16]—the longest to date—found that 60% of patients experienced heterotopic ossification and spontaneous ankylosis related to the TDA, suggesting that the implant did not restore normal function or segmental motion in those patients. Reported complications that relate to the implant's biomechanics include subsidence [8–11], dislocation [12–14], heterotopic ossification [15–19], and adjacent-level vertebral fracture [9,20–24]. Subsidence (Figure 1–2), in particular, will be discussed in each of the following chapters.

1.4 Impingement

Implant impingement—that is, contact between the rim of the polyethylene component and the metal footplate, or contact between two metal footplates (Figure 1–3)—can occur in both lateral and sagittal bending [14,86,95–97,87–94]. This loading mode is thought be relatively common following TDA, and can damage the ultra-high molecular weight polyethylene (UHMWPE) inserts used in many devices (Figure 1–4) [14,86,95,96,87–94]. The severity of damage to implant components, as well as *in vitro* [94] and *in silico* [95] experiments indicate that large loads can be transmitted through the impinged regions.

The effects of impingement on the underlying vertebral bone are unclear [71,98]. A central aim of this dissertation is to study how impingement loading affects the stress in the bone tissue, the cortical-trabecular load-sharing behavior, and the whole-bone yield strength.

Presented next are the composition, structure, and mechanics of bone tissue and the vertebral body.

1.5 The composition, structure, and mechanics of bone tissue

Bone tissue is a composite material consisting mainly of the calcium phosphate mineral hydroxyapatite (approximately 65% by mass) surrounding fibrous collagen protein [99]. There are also other constituents, including water, non-collagenous proteins, and living bone cells. Three types of bone cells are responsible for either deposition, resorption, or maintenance of bone tissue: osteoblasts form new bone tissue by depositing collagen-rich organic material (osteoid) which binds to minerals; osteoclasts resorb bone tissue by secreting hydrochloric acid, dissolving the mineral; and osteocytes help maintain bone homeostasis, likely by directing tissue remodeling (e.g. osteoblast and osteoclast activity) via mechano-sensation, although the specific mechanisms are not fully understood [99–101].

The collagen fibrils surrounded by mineral (Figure 1–5, 0.1 μm size scale) organize typically into stacked sheets of lamellae (10 μm size scale), with fibrils that arrange unidirectionally in regions of a single sheet and vary directionally both within and between sheets [101,102]. Non-lamellar, randomly oriented bone called woven bone can also form,

typically during skeletal growth and fracture healing. In the case of lamellar bone, the stacked sheets organize next into either osteons (concentric rings of lamellae with a central canal [the Haversian canal] for vascularization and innervation) or stratify into a network of rods and plates (100–1000 μm size scale) [101,102]. Osteons organize roughly in parallel to comprise cortical bone, the solid-appearing exterior of most whole-bones. While appearing solid macroscopically, cortical porosity is typically 5 to < 30%, with small (< 200 μm) voids for Haversian canals, canaliculi, cells, and erosion cavities [102,103]. In contrast to cortical bone, trabecular bone is comprised of mostly non-osteonal lamellar bone which organizes into a series of interconnected three-dimensional rods and plates, forming the internal structure of many whole bones (e.g. the vertebral body) and bone regions (e.g. the proximal femur) [99]. The trabecular network includes large pores, typical 500–1500 μm thick, with an overall apparent porosity of 50–95% [102]. The porous regions of the trabecular bone typically fill with marrow *in vivo*, though this is not thought to have a substantial mechanical effect at physiologic strain rates [104].

The microscopic structural differences between cortical and trabecular bone tissue yield different mechanical properties. Most cortical bone exhibits approximately transversely isotropic behavior; that is, it has one set of mechanical properties along an axis of symmetry (oriented longitudinally along the axis of the osteons) and a different set of mechanical properties orthogonal to this long axis (Figure 1–6). Less is understood about the mechanical properties of trabecular bone tissue, primarily due to difficulties with experimental techniques of material characterization (such as uniaxial tension or compression tests) on small individual trabeculae [103,105]. Trabecular tissue is often assumed to be approximately isotropic (characterized by a single elastic modulus and Poisson ratio applicable to all loading direction) [106–108], partly because it lacks the parallel osteonal organization found in most cortical bone and partly because little data exist characterizing trabecular tissue anisotropy [104,109]. Data suggest that trabecular bone exhibits linearly elastic behavior [110], though reports of the trabecular tissue's elastic modulus are highly variable, spanning roughly 1–20 GPa (typically ranging 10–20 GPa) [105,109,111,112].

Regardless of the isotropy or anisotropy of the trabecular tissue itself, the structural organization of the trabecular tissue yields highly anisotropic whole-bone mechanical behavior associated with the direction of principal mechanical loads [105,111]. The ability of whole bones to resist mechanical loads depends on the trabecular orientation relative to the applied load [113], and trabecular bone re-models and re-orients in response to mechanical loading [114,115]. The organization of the trabecular bone tissue into a three dimensional, spatially variable network is referred to as the bone's microstructure (or microarchitecture), which can be quantified using standard metrics. The microarchitectural metrics used here in the study of TDA-implanted vertebrae include trabecular bone volume fraction (BV/TV), mean trabecular thickness (Tb.Th), mean trabecular spacing (Tb.Sp), trabecular connectivity density (Conn.D), and mean ellipsoid factor (Tb.EF; a relatively new metric which quantifies the relative rod- versus plate-like geometry more accurately than structural model index [SMI], the historic predicate [116,117]). Each parameter is described in more detail in the following chapters.

Bone tissue yields at a low magnitude of strain (≤ 1%) that depends on the loading mode [110]. Strength is lower in tension than in compression, with a tension-compression strength-asymmetry ratio of approximately 0.4–0.7 [109,110,118,119]. Though the strength is

asymmetric, the elastic modulus of bone tissue is approximately symmetric in tension versus compression (Figure 1–6) [102,110].

Other important aspects of bone-tissue mechanical behavior relate to viscoelasticity, monotonic fracture, and fatigue fracture. Briefly, bones are hydrated *in vivo* and this hydration is essential to normal mechanical function; dry bones are stiffer and more brittle than wet bones [103]. However, viscoelastic effects are small over typical variations in physiologic rates of strain. For example, a one-thousand-fold increase in strain rate results in less than a 50% change in elastic modulus and strength [103,104], suggesting that bone-tissue material properties should be relatively constant for many physiologic activities but could change appreciably the event of high-strain rate event such as a car accident or other trauma. Consistent with its viscoelastic nature, creep deformation can also occur in bone tissue [104]. In fatigue loading, trabecular bone cores display S–N type behavior; the number of cycles to failure relates closely to the apparent stress normalized by the initial apparent elastic modulus [104].

1.5 The vertebral body

The vertebral body—referring to the anterior weight-bearing region of the vertebra excluding the posterior elements—is comprised primarily of trabecular bone with an external cortical shell and covered on both ends with osseous endplates (Figure 1–7). The cortical shell and endplates are thin, typically less than 0.5 mm thick [120]. Despite being referred to as cortical bone, the vertebral cortex does not usually contain the same osteon density as cortical bone elsewhere in the body [121] and may therefore not follow a transversely isotropic constitutive tissue material model rooted in osteon orientation. It has been suggested that the cortical bone in the vertebral body better resembles condensed trabecular bone histologically [120,122]; this observation motivates the tissue-level modeling assumptions used in the finite element experiments described later.

1.6 Micro-computed-tomography-based finite element modeling

Micro-CT-based finite element analysis has been used extensively in the bone biomechanics field to provide insight into a diverse class of problems including the estimation of bone-tissue elastic and failure properties, and mechanisms of osteoporotic fracture in the hip and spine [107,108,123–127]. The main advantage of micro-CT versus other computed-tomography-based finite element approaches (such as those based on quantitative-computed tomography) is that the spatial resolution of micro-CT (< 1 to ~80 μm) is such that the accurate geometric details of the trabecular microstructure are captured in three dimensions; thus, finite element models based on micro-CT image data intrinsically incorporate the contributions of the complete morphometry of the calcified bone tissue, including the structural anisotropy and connectivity of the trabecular microstructure. Typically in this approach, the voxels comprising the micro-CT data are converted directly into hexahedral finite elements, bypassing the need for a more complex mathematical description of the trabecular bone geometry as required for isoparametric and smoothed meshes [128].

A key advantage of this high-resolution approach is that it enables estimation of the micromechanics, including stress, within the bone tissue itself (Figure 1–8) [107,129,130]. When

first implemented, micro-CT-based finite element analysis represented a major methodological advance in bone biomechanics [128] relative to quantitative-computed tomography- (QCT-) based finite element models. QCT-based finite element models use population-based-statistical material models to relate apparent bone mineral density to apparent elastic modulus at the continuum level, neglecting the realistic morphometric details of the microstructure [71].

A second advantage of finite element modeling—not unique to micro-CT-based models—is that, unlike many physical biomechanical tests, finite element analysis is non-destructive. The non-destructive nature enables highly controlled parameter studies (typically involving repeated measurements taken on the same specimen) to investigate the independent roles of key variables, such as loading mode, implant size, or material properties. The accuracy of all finite element models depends on the accuracy of the geometric representation of the data, constitutive model, choice of boundary conditions, and the extent of numerical convergence [131]. Details of the validity of the method used in this dissertation are provided in the subsequent chapters and supporting experimental data collected by others is included in the appendix (Appendix 7.9).

One challenging aspect of micro-CT-based finite element analysis relates to the model size; that is, the number of degrees of freedom, or algebraic equations that must be solved. Convergence studies [132,133] have recommended that approximately four finite elements (on average) span the thickness of the individual trabeculae: to meet this criterion, small human trabecular bone cores (8 mm diameter, 20 mm length) require millions of elements, presenting substantial technical challenges related to computational time [119,126,134]. High-resolution whole-bone models based on this approach are therefore infeasible with serial finite element codes implemented using conventional computer hardware [134]. However, parallel finite element approaches implemented on high-performance supercomputing clusters make the study of larger regions of interest possible; for example, studies on entire human vertebral bodies and proximal femurs with over 100 million elements, and which account for geometric and material nonlinearites in the bone tissue, have been conducted in parallel on high-performance supercomputers [135]. On a single modern processor the same study would have required an equivalent computational time of over 300 years [135].

The micro-CT-based finite element approach used here utilizes a parallel finite element framework (*Olympus* [134]) implemented on a 18-petaflop supercomputing cluster (Stampede2; Texas Advanced Computing Center; Austin, TX). This supercomputing cluster contains 4,200 Intel Xeon Phi 7250 compute nodes, each with 68 cores and 96 GB RAM; plus 1,736 Intel Xeon Platinum 8160 compute nodes, each with 48 cores and 192 GB of RAM—making it one of the largest civilian supercomputers in the world [136].

Olympus's numerical methods involve a parallel mesh partitioner to construct sub-problems on each processor so that the overall finite element problem can be solved in parallel, utilizing thousands of processors simultaneously. Each sub-problem—typically comprising ~150,000–300,000 mesh nodes (based on computational-time optimization studies)—is solved in serial using a standard finite element code; in other words, each processor computes the entire stiffness matrix and residual vector for the mesh nodes partitioned to that processor [134]. As the smaller sub-problems are solved on each processor, the *Olympus* code uses an inexact Newton

method to control the overall solution process: each Newton iteration is solved using a parallel algebraic multigrid solver. When implemented on a high-performance scientific supercomputing cluster such as Stampede2, this finite element approach can simulate whole bone models that incorporate both material nonlinearties (e.g. tissue yielding and plastic deformation) as well as geometric nonlinearities (e.g. finite strain assumptions, wherein the stiffness matrix is updated based on changes in the mesh's orientation). In the modeling of human bone, accounting for both of these nonlinearities is required in order to accurately capture the large-deformation mechanisms in bone tissue; these large-deformation effects can be substantial in bones with low volume fractions [119].

The work presented here is the first of its kind to apply this high-resolution modeling approach to the bone biomechanics of whole human vertebrae implanted with TDA implants. The fundamental insight enabled by this approach has substantially advanced the bone biomechanics field; likewise, applying this approach to TDA implants has the potential to substantially advance the study of bone-implant systems in the human spine.

1.7 Objectives and scope of the dissertation

The goal of this dissertation is to elucidate the biomechanical behavior of the vertebral bone supporting a lumbar TDA implant. The work comprises three separate but related *in silico* experiments conducted on pre-existing micro-CT data of 12 human lumbar vertebrae from male and female cadavers spanning a wide range of ages (51–89 years), bone volume fractions (0.060–0.145), and overall vertebral morphologies.

The first study (Chapter 2) addresses the need to understand how bone tissue stress varies as a function of the size and material properties of the implant footplate (the implant component directly loading the bone), as well as the loading mode of the implant (axial compression versus forward flexion). Understanding the role of footplate size on bone tissue stress is essential because smaller implant footplates have been linked to implant subsidence [8], though the mechanisms in the bone governing this behavior are unclear. For example, it's not known whether the implant's loading mode changes the relationship between implant size and bone-tissue stress. A second goal is to understand how the implant's size, material properties, and loading mode alter the way in which load is shared between cortical and trabecular compartments, a fundamental biomechanical issue which may help mechanistically explain implant-induced alterations in whole-bone strength or tissue remodeling.

The second study (Chapter 3) addresses the role of bone porosity and morphologic heterogeneity on bone tissue stress following TDA using a clinically reasonable footplate size. Low apparent bone mineral density (porosity = 1 – trabecular bone volume fraction, proportional to apparent bone mineral density) has been linked to implant subsidence and vertebral fracture [9,137], yet it's unclear how the stress in the bone depends on the porosity of the underlying vertebral body. In part, this study was also designed to assess whether the results from Chapter 2 are generalizable to a larger set of human lumbar vertebrae; therefore, n = 12 bones were included in this study.

The third study (Chapter 4) addresses the independent and combined roles of the vertebral morphology and microarchitecture—such as the trabecular bone volume fraction, mean trabecular thickness, mean cortical thickness, etc.—on whole-bone yield strength. A central goal of this study was to assess whether the yield strength of the vertebral body is altered by the presence of an implant (relative to loading via bone cement, typical in biomechanical experiments) or on the loading mode of the implant. Studying the roles of bone morphology and microarchitecture on whole-bone yield strength is essential to help identify the features of the bone associated with a lower overall strength when load is applied via a TDA implant, which could relate to implant subsidence. In turn, this insight could motivate device designs that reduce the risk of subsidence, identify new *in vitro* test protocols for device development and regulation, and help clarify discrepancies in clinical guidelines such as whether osteopenia or osteoporosis is a more appropriate clinical exclusion criteria.

The final chapter (Chapter 5) summarizes the conclusions and suggests topics for further research.

Table 1–1. Contraindications to TDA cited in clinical studies. Adapted from [25].

Anatomic/inherent

- Pars defects
- Fracture at L4, L5, compromised vertebral body
- Disc height < 3mm
- End stage disc resorption and collapse
- Facet ankylosis
- Facet joint arthrosis/degeneration
- Retrolisthesis
- Posterior element insufficiency
- Pseudoarthrosis
- Scoliosis or major deformity
- Irregular vertebral body endplate shape
- Spondylosis
- Spondylolisthesis
- Isthmic spondylolysis / olisthesis
- Lumbosacral joint anomalies
- Instability
- Prior decompressive laminectomy
- Previous fusion
- Postsurgical deficiency of posterior elements, or prior posterior lumbar surgery with significant morbidity

Subsidence or dislocation risk

- Osteoporosis
- Endocrine or metabolic disorder known to affect osteogenesis
- Metabolic bone disease
- Osteopenia
- Osteopathy
- Paget disease
- Chronic steroid use

General

- Infection
- Active hepatitis
- Active malignancy
- 3 or more Waddell signs
- Autoimmune disorder
- Pregnancy
- Psychosocial disorder
- Osteomyelitis
- Spondylodiscitis
- Chronic disease of a major organ – cardiac failure, hepatitis, diabetes
- Neuromuscular disease
- Ankylosing spondylitis
- Spinal tumor

Implant-related

- History of hypersensitivity to protein pharmaceuticals or collagen
- History of implant rejection
- Metal allergy
- History of anaphylaxis

Approach-related

- Obesity – definition varied with study
- Vascular anatomy that is aberrant
- Vascular calcification
- Previous abdominal surgery
- Abdominal wall hernia
- Previous iliofemoral phlebitis
- Abdominal pain profile
- Previous vascular surgery
- Prior retroperitoneal radiation
- Prior surgery at the involved level

Pathology

- Nerve root compression
- Positive straight leg raise
- Radicular pain symptomology
- Straight leg raise producing pain below knee
- Noncontained herniated nucleus pulposus
- Scarring from previous surgery
- Arachnoiditis
- Stenosis
- Multilevel degeneration beyond 1 or 2 levels specified for TDR
- Previous spinal surgery at affected level – except for discectomy, laminotomy/ectomy, without accompanying facetotomy, or intradiscal procedures at the level to be treated
- Fibromyalgia
- Cervical myelopathy

Other

- Previous exposure to any or all bone morphogenetic proteins (human or animal)

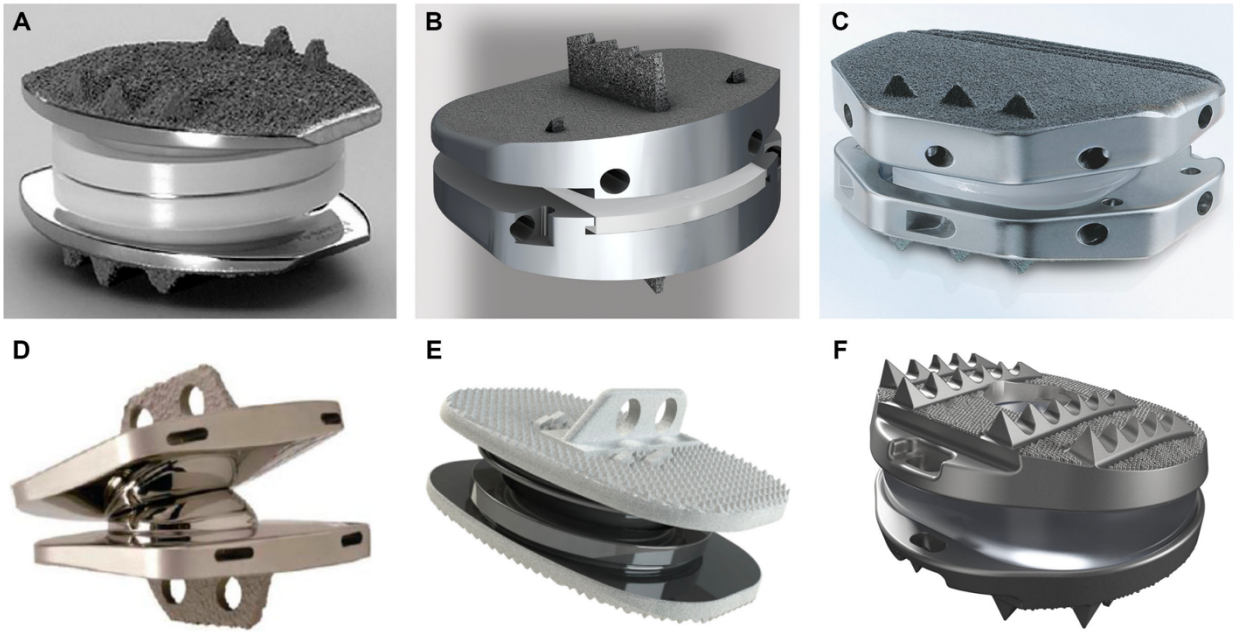

Figure 1–1. Modern lumbar total disc replacement devices. (A) Charité III, DePuy Synthes Spine (B) ProDisc-L, Centinel Spine (C) activL, Aesculap Implant Systems (D) Maverick, Medtronic (E) Kineflex, Simplify Medical (F) Freeedom, KIC Ventures. Reproduced from [6].

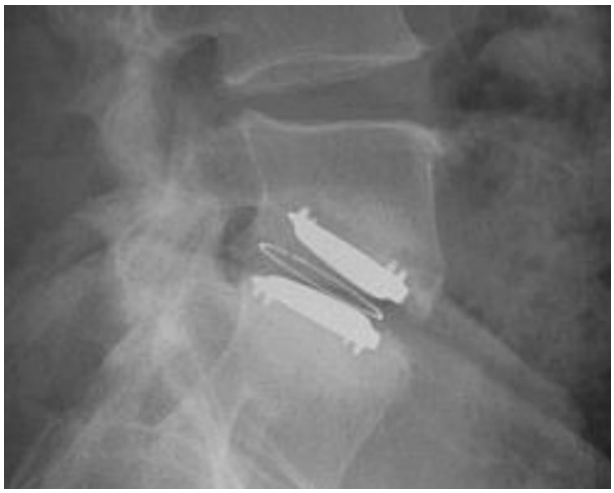

Figure 1–2. Lateral radiograph showing implant subsidence into the vertebral body, one of the most frequently reported complications following TDA. Reproduced from [11].

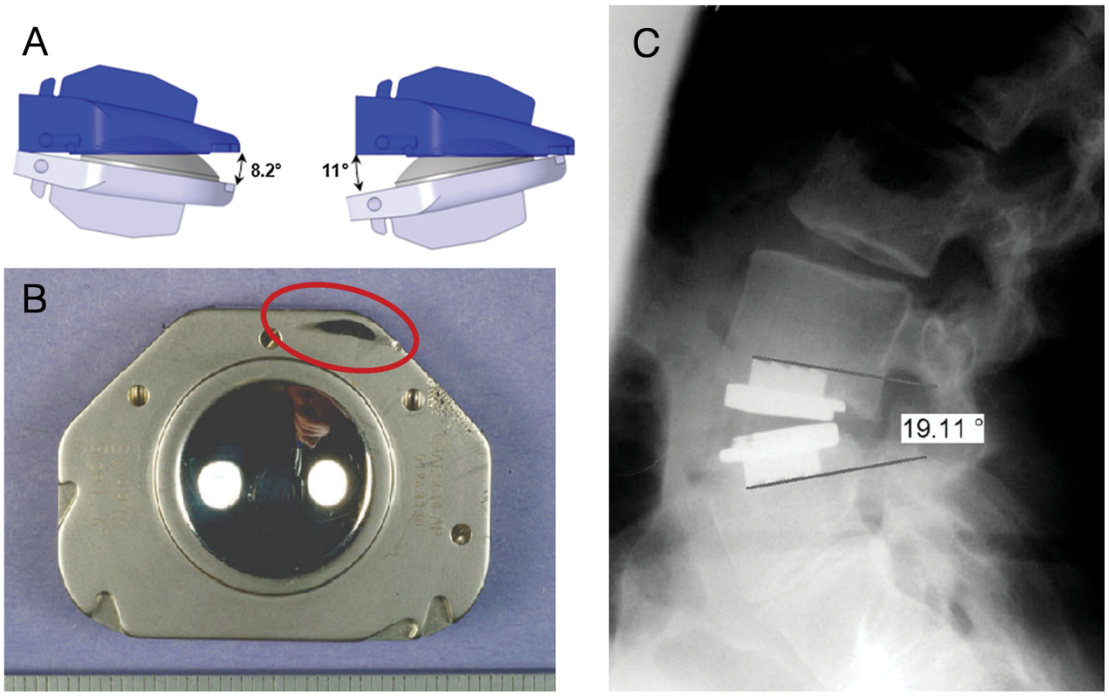

Figure 1–3. (A) Illustration of impingement induced by sagittal bending. (B) An explanted TDA footplate demonstrating anterior flexion-induced impingement damage (red). (A) and (B) reproduced from [93]. (C) Lateral radiograph showing extension-induced impingement *in vivo*. Reproduced from [92].

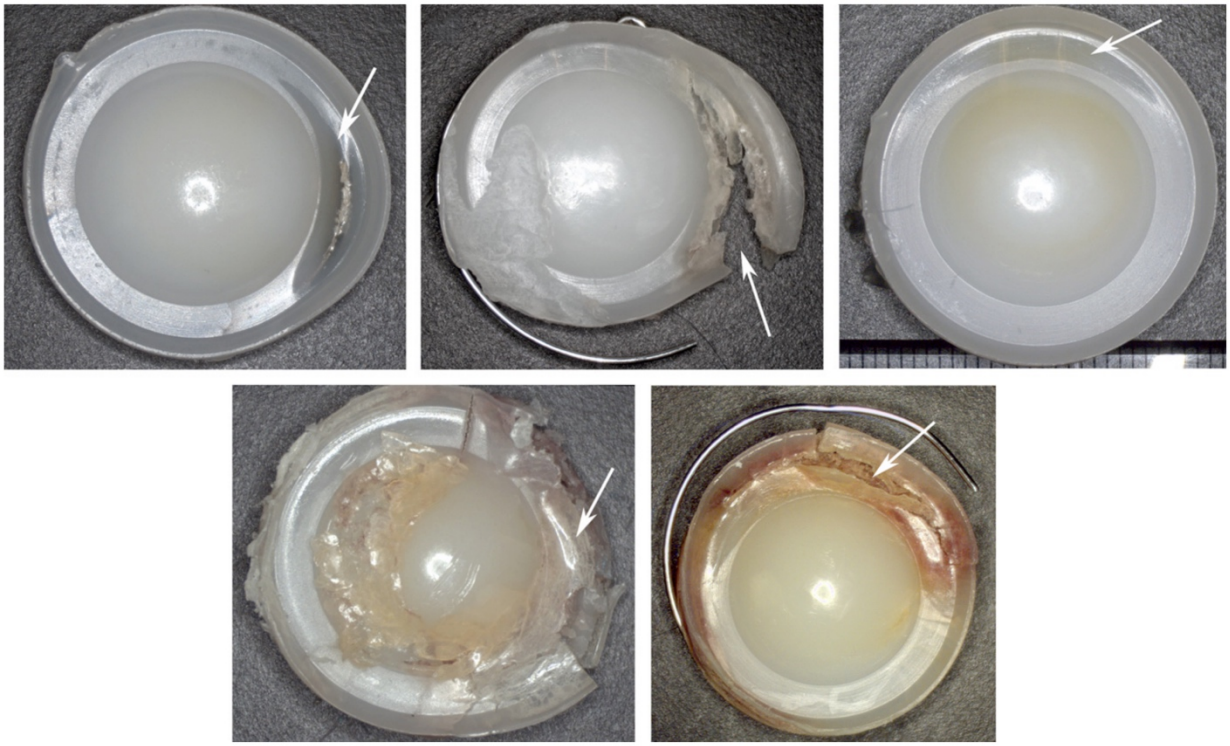

Figure 1–4. Retrieved ultra-high molecular weight polyethylene inserts damage by impingement *in vivo*. The severity of damage indicates that large loads can be transmitted through the impinged regions. Reproduced from [14].

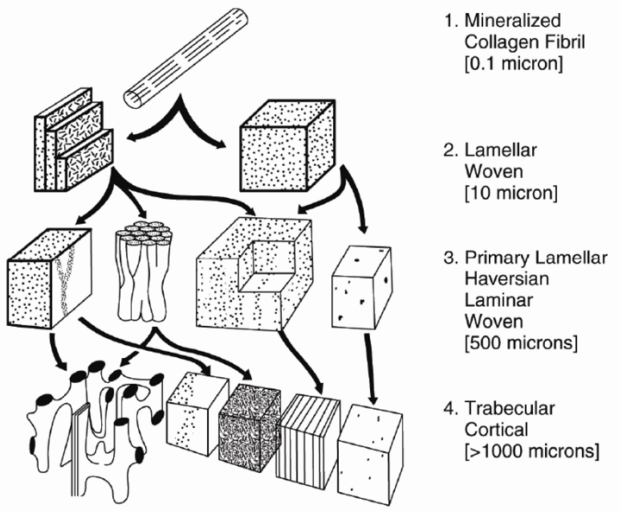

Figure 1–5. The structural hierarchy of bone tissue from 0.1 to >1000 μm. Reproduced from [102].

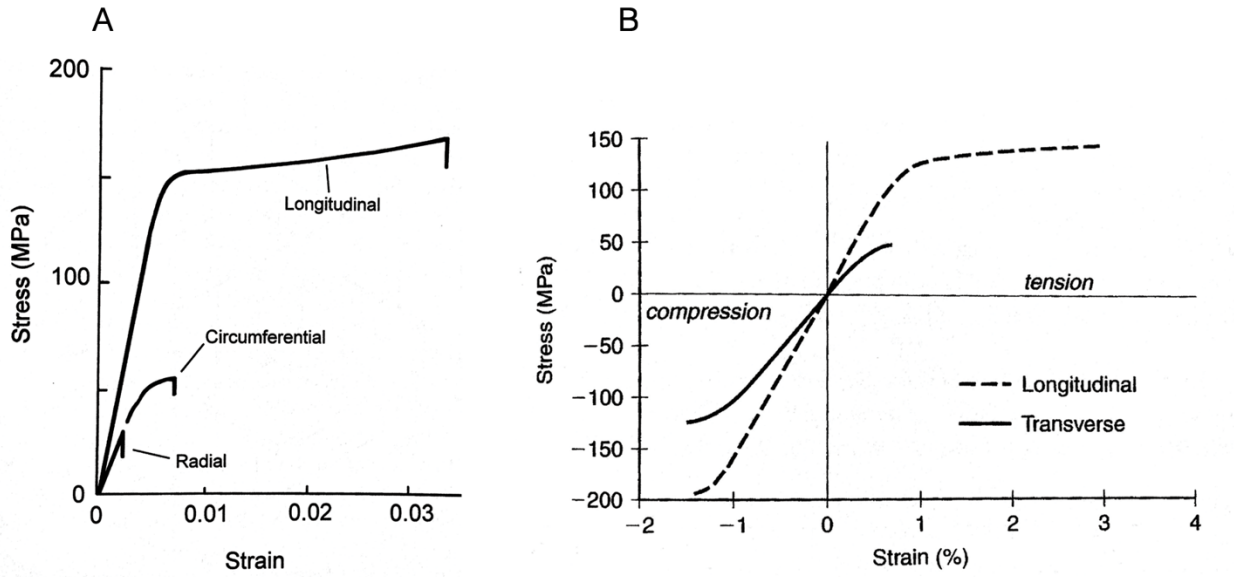

Figure 1–6. Idealized stress-strain curves of typical cortical bone tissue depicting transverse elastic isotropy (separate elastic modulii for the longitudinal versus circumferential or radial [transverse] directions). Unlike most cortical bone, vertebral cortical bone does not have many osteons and its behavior is not necessarily transversely isotropic. (A) Reproduced from [103], data derived from [138]. (B) The elastic modulus of bone tissue is similar in compression and tension, though the yield strengths are asymmetric. Reproduced from [102].

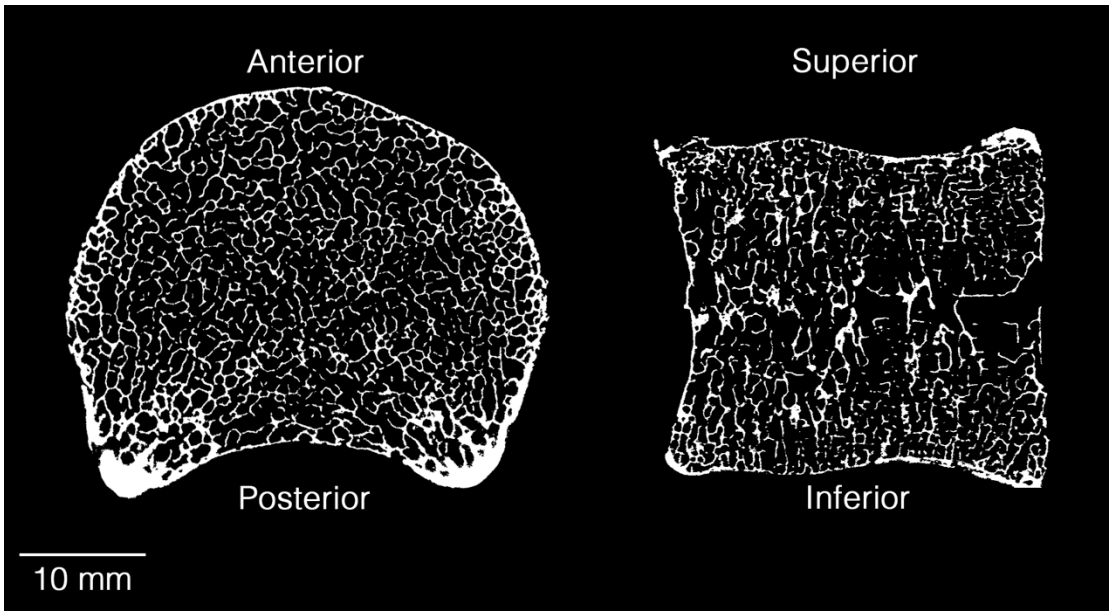

Figure 1–7. A transverse (left) and sagittal (right) cross-section of a human lumbar vertebral body from a 54-year-old male cadaver as imaged with micro-CT (thickness = 37 μm = isotropic scan resolution). The vertebral body is comprised primarily of trabecular bone with a thin cortical shell and thin endplates (each typically < 0.5 mm thick [120]). A global threshold was applied to segment the marrow and soft tissue from the calcified bone.

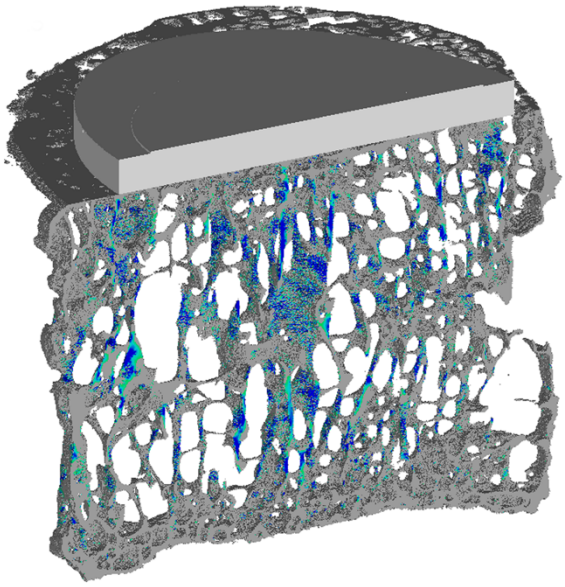

Figure 1–8. A mid-sagittal cross-section of a human lumbar vertebral body virtually implanted with an elliptical TDA footplate. Micro-CT based finite element analysis (in which the bone geometry is based on a one-to-one mapping of voxels to finite elements) was used to calculate bone tissue stress (colors).

2. The effects of implant size and stiffness on trabecular-cortical load-sharing behavior and tissue-level stress

2.1 Introduction

Reduced implant coverage—a smaller footprint of the implant on the vertebral endplate—is associated with elevated interfacial stresses [139] and a higher incidence of implant subsidence [8], suggesting that small implants may cause high stresses and failure of underlying bone. Implants that cover an equivalent percentage of the vertebral endplate but have different shapes can require different forces to subside into the bone because they recruit different regions of the endplate and underlying trabecular microstructure [140]. Despite this understanding, the fundamental load-transfer behavior within a vertebral body supporting a TDA implant remains largely unknown. For example, it's not known whether implant-induced changes in stress occur in local regions adjacent to the implant and then dissipate in deeper regions, or whether the extent of the vertebral body is impacted. Similarly, it's not known how stresses within the trabecular microstructure change as a function of implant size or material. The etiology of subsidence also remains unclear. Data from Punt et al [8] show that for 60% (21/35) of clinically diagnosed cases of subsidence, the implant footprint did not subside in a parallel manner but rather rotated by at least 5° relative to the bony endplate. This suggests that bending could be involved in subsidence, though this link has not been previously established.

In part, these uncertainties arise because of the structural complexity of the human vertebral body, including the spatially variable trabecular microarchitecture and thin cortical shell and endplates. Addressing this issue, the goal of this study was to elucidate the role of implant size and stiffness on load-transfer behavior within the vertebral body following TDA, accounting for realistic multi-scale geometric features of human vertebral bone. Micro-computed tomography- (micro-CT)-based finite element analysis was used to capture and analyze these features. The high resolution and mechanistic nature of micro-CT-based finite element analysis has provided unique insight into the mechanisms of osteoporotic wedge-fracture [107], the mechanical role of the trabecular microstructure [108], *in vivo* structural changes to bone [127], and fundamental properties of bone tissue [123,124] and is therefore well suited to investigate tissue-level mechanics following TDA. Specifically, for both uniform compression and flexion-induced anterior impingement, the effects of implant size and stiffness on trabecular-cortical load-sharing behavior, stress and stress changes in the vertebral bone tissue, and the spatial distribution of tissue at the highest risk of failure were investigated. The resulting insight can help elucidate fundamental biomechanical behavior for this class of device, including how implant design may facilitate the replication of a natural biomechanical environment in adjacent vertebrae.

2.2 Methods

Study Design

This study comprised parametric, high-resolution, micro-CT-based finite element analysis of a human vertebral body virtually implanted with generically shaped elliptical TDA implants of varying sizes and stiffness and loaded in compression and flexion-induced anterior

impingement. Generic implant footplates were modeled as 3-mm-thick elliptical plates with varying major and minor diameters. This simplified implant model assumes that subtle details of the implant geometry have only a secondary effect on tissue-level stresses within the vertebral body relative to footplate size (Appendix 7.1). Implant models were compared against an intact (no-implant) case, which simulated loading via a disc-like material covering the superior and inferior endplates.

Specimen Preparation and Micro-CT Scanning

Existing micro-CT image data from one human L1 vertebral body from a de-identified 80-year-old male cadaver with no history of metabolic bone disorder was analyzed in this study. The bone volume fraction (BV/TV) was 0.23 for the entire vertebral body (cortical shell included). This value is higher than has been reported for osteoporotic vertebrae [141] and is therefore typical of what would be expected for a TDA candidate. The micro-CT scan had an isotropic pixel size of 37 μm and the posterior elements were removed to isolate the vertebral body. To reduce computational cost, the scan was coarsened to 74 μm before the hard-tissue and marrow were segmented using a global threshold value. Bone tissue was then compartmentalized into trabecular, cortical, and endplate tissue using custom algorithms described elsewhere (Figure 2–1A) [142]. A planar surface was virtually created superiorly to mimic surgical preparation [143,144] prior to TDA implantation. This required resection through parts, but not all, of the osseous endplate.

Finite Element Analysis

Each 74 μm voxel in the coarsened scan was converted into an 8-noded hexahedral finite element [142]. A TDA implant, also modeled using voxels, was placed such that the implant center coincided with anterior-posterior (A/P) and medial-lateral (M/L) midpoint of the vertebral body (the A/P dimension was measured from the vertebral foramen).

To simulate compressive loading of an intact disc, a uniform compressive displacement boundary condition was applied to the superior disc (Figure 2–1A). Following calculation of the finite element solution, results were scaled linearly to produce a net reaction force of 800 N (approximately 1x body weight [145]), a typical force at that spinal level for static standing [146]. To simulate flexion of an intact disc, a displacement boundary condition was used to rotate the disc in the mid-sagittal plane about the far posterior-superior point, simulating flexion over a single motion segment (Figure 2–1B) [107,147]. Results were then scaled linearly to produce an overall reaction force of 800 N. While flexion can increase loads on the spine two- to three-fold compared to what was modeled here [146,148], a reaction force of 800 N was maintained in order to facilitate comparison across models. Compression of an implanted segment was modeled by applying a uniform force of 800 N to the superior implant footplate (Figure 2–1C). Flexion of an implanted segment was modeled by assuming impingement between the footplate and the insert (Figure 2–1D). There is substantial evidence that impingement occurs *in vivo* in flexion/extension and lateral bending for both unconstrained (e.g. Charité) and semi-constrained (e.g. ProDisc-L, activL) devices [14,86,91–96]. Analysis of retrieved implants and *in vitro* experiments suggests that large loads are transmitted through the impinged regions during bending [14,86,94]. Therefore, flexion of an implanted segment was

modeled by applying a net force of 800 N to a 2 mm thick, 90° arc of the footplate, representing load-transfer through the footplate induced by impingement (Figure 2–2). The distance from the implant center to the impinged region (r) was set as 40% of the footplate A/P diameter and was chosen because it represents a typical impingement moment arm for devices used clinically. For all models, an intervertebral disc-like material was modeled inferiorly using a roller-type (symmetry) boundary condition applied to the base of a 4-mm-thick disc, thereby simulating an 8-mm-thick disc with unconstrained bulging.

All bone elements were assigned the same elastic material properties ($E = 10.3$ GPa, $\nu = 0.30$ [149]). While absolute values of stress in the bone directly depend on the choice of tissue material properties, the relative outcomes described here are insensitive to uncertainties in tissue modulus over a realistic physiologic range (Appendix 7.2). Disc elements were assigned material properties consistent with the measured effective (homogenized) modulus of the disc at a low loading rate ($E = 8$ MPa, $\nu = 0.45$ [106]). Implant modulus was parametrically varied as described below ($\nu = 0.33$). Perfect bonding was assumed at all interfaces, thereby modeling full footplate fixation in the bone [71,150].

As described below, a total of twenty analyses were run. Depending on implant size, individual models had 36–46 million elements and 141–174 million degrees of freedom. All analyses were linearly elastic and were solved on a supercomputing cluster (Stampede2, Austin, TX) using a custom finite element code that included a parallel mesh partitioner and an algebraic multi-grid solver [134]. A typical analysis utilized 1,100 processors, 3,000 GB of memory, and required over 200 CPU hours.

Parametric Variation

Both implant size and elastic modulus were parametrically varied. Three implant sizes were modeled to represent small, medium, and large implants. The major and minor implant diameters were defined as 50%, 75% and 100% of the M/L and A/P dimensions of the vertebral body (44.6 mm M/L, 31.5 mm A/P) for the cases of small, medium, and large implants, respectively. A survey of lumbar TDA implants (Charité III, Maverick, ProDisc-L, MobidiscL, activL) showed dimensional ranges of 28.5–42.5 and 23.0–36.0 mm (M/L and A/P, respectively, min–max). Thus, the medium implant in the current study is within the range of clinically used implants, while the small and large implants represent dimensional extremes. For each implant size, three implant materials were analyzed. Elastic moduli of 100 GPa, 1 GPa, and 0.01 GPa were chosen to represent generic metallic, polymeric, and hypothetical tissue-engineered implants, respectively [106,151].

Outcomes

The primary outcomes were: 1) trabecular-cortical load-sharing behavior; 2) the spatial distribution of tissue at the highest risk of initial failure; and 3) stress and stress changes in the bone tissue relative to the intact model. Trabecular-cortical load-sharing was quantified using the cortical load fraction, which was calculated at each transverse slice as the ratio of axial force in the cortical bone to that in the whole vertebra; trabecular load fraction equals unity minus cortical load fraction [142]. High-risk tissue was defined as the 10% of bone tissue at the highest

risk of initial failure [107]. This was quantified by taking the ratio of the maximum and minimum principal stresses of each bone element (calculated at the element centroids) to its tensile (61 MPa) or compressive (150 MPa) yield stress [119], respectively, then taking the higher value of this ratio. After ranking values across all elements, high-risk tissue was defined as the top 10% of values [106,107]. To evaluate tissue-level stress in the bone, the minimum principal stress (calculated at the element centroids) was visually plotted and compared. To quantify changes in stress compared to normal physiologic loading, the von Mises stress (calculated at the element centroids) for each implanted model was subtracted, element-by-element, from the intact model.

2.3 Results

In both axial compression and flexion-induced anterior impingement, the presence of an implant altered the trabecular-cortical load-sharing behavior and spatial distribution of high-risk tissue relative to the intact disc both adjacent to the implant and also deep into the vertebral body (Figure 2–3). These alterations depended more on implant size than material.

In compression, the cortical shell experienced less overall load relative to the intact disc for all implant sizes and materials (Figure 2–3A). Among the implant models, the large implant transferred the most load into the cortical shell and thus best replicated the intact disc in compression. In flexion, on the other hand, the cortical load fraction for the implant models could be either less than or greater than that of the intact disc, depending on implant size (Figure 2–3B). Small and medium implants decreased, while large implants increased, the cortical load fraction relative to the intact disc, regardless of implant material. For the large size, the cortical load fraction exceeded that of the intact disc by up to 23% (this occurred 9 mm away from the bone-implant interface, at an axial position of 70%). At most axial positions, the medium implant best replicated the load-sharing behavior of the intact disc in flexion.

Flexion of medium and large implants shifted high-risk tissue anteriorly in a way that flexion with an intact disc did not (Figure 2–3D). For the intact disc, flexion skewed the high-risk tissue distribution anteriorly; however, the high-risk tissue was also distributed over the A/P extent of the bone. Conversely, for the medium and large implants, flexion induced a spike in high-risk tissue anteriorly (6 mm from the bone's anterior edge, at a relative A/P position of 18%). The peaks of the high-risk distribution for medium and large implants were 170 and 200% larger, respectively, than that of the intact disc (this a measure of how localized the high-risk tissue is, since the area under all curves is equivalent by definition). Thus, in flexion, bone at the highest risk of failure was concentrated anteriorly for medium and large implants whereas it was distributed over the A/P extent of the bone for the intact disc. The small implant did not shift high-risk tissue to anterior regions or increase the peak value of the distribution relative to the intact disc. In flexion, the small size best replicated the intact disc with respect to the A/P distribution of high-risk tissue.

The magnitude of the minimum principal stress in the bone tissue was higher in flexion than in compression and tended to increase as implant size decreased (Figure 2–4, Figure 2–5). For the intact disc, flexion increased the 98th percentile of minimum principal stress in the bone by 18% (17 versus 20 MPa, compression versus flexion. In contrast, flexion of the medium

implant increased trabecular stress by 49% (35 versus 52 MPa, compression versus flexion, median between implant materials) and cortical stress by 150% (12 versus 30 MPa, compression versus flexion, material median, Figure 2–5). The high stress values that developed within the trabecular bone for the medium implant in flexion were similar to those that developed for the small implant in compression (medium: range 48–58 MPa, small: range 50–52 MPa across materials). The large implant was most similar to the intact disc in compression; it increased trabecular and cortical stresses by 24% and 17%, respectively (trabecular: 21 versus 26 MPa, cortical: 12 versus 14 MPa, intact disc versus large implant in compression, material median). In flexion, however, the large implant increased trabecular and cortical stresses by 80% and 214%, respectively, relative to the intact disc in flexion (trabecular: 25 versus 45 MPa, cortical: 14 versus 44 MPa, intact disc versus large implant in compression, material median). The large implant thus overloaded the cortical shell in flexion.

Tissue-level changes in von Mises stress between the implanted and intact models showed that implants altered stress deep into the vertebral body (Figure 2–6). At a mid-sagittal location, flexion of the medium and large implants increased stresses in the anterior cortex by at least 100% throughout the S/I extent of the vertebra. For the small implant, stress in the trabecular centrum both adjacent to the implant and also in deeper regions of the vertebral body increased by at least 100% in both compression and flexion.

In compression, large implants caused 34 ± 1% of bone tissue to experience von Mises stress changes greater than ± 50% relative to the intact model, compared with 51 ± 2 and 58 ± 0% of bone tissue for medium and small implants, respectively (material median ± range). In flexion, on the other hand, large implants caused 57 ± 3% of bone tissue to experience von Mises stress changes greater than ± 50% relative to the intact model, compared with 51 ± 1 and 53 ± 8% for medium and small implants, respectively (material median ± range).

2.4 Discussion

These results indicate that the presence of a TDA implant can substantially alter cortical-trabecular load-sharing, the spatial distribution of high-risk tissue, and stress in bone tissue throughout the vertebral body relative to an intact disc. Implant size has a larger effect on these alterations than implant material in both compression and flexion-induced anterior impingement. The differences in load-transfer behavior between the intact model and the implant models were much larger for flexion-induced anterior impingement than for compression. In other words, flexion to the point of impingement with an implant caused much larger deviations from the natural biomechanical environment compared to compression with an implant. Specifically, flexion with an implant caused local increases in stress anteriorly and shifted the tissue at the highest risk of failure to local anterior regions. This behavior was accentuated as implant size increased but did not depend much on implant material properties.

The medium implant in this study is of particular interest because it's most representative of devices used clinically: the dimensions of the implant and dimensional mismatch between the implant and the underlying vertebra are both within the range found clinically [152]. Results suggest that implants of this size recruit less overall cortical bone than the intact disc in compression, thereby overloading the trabecular centrum, at nearly all axial positions in the

vertebral body. For flexion-induced anterior impingement, the medium implant substantially elevated load in the anterior cortex and anterior trabecular centrum relative to flexion with the intact disc (> 100% change in minimum principal and von Mises stress) and concentrated the tissue at the highest risk of failure anteriorly. Thus, most TDA implants, regardless of their overall stiffness properties, likely diminish the load-bearing role of the cortical shell in compression, rely more on anterior trabecular regions and the anterior cortex to resist the loads that develop in flexion, and otherwise re-distribute stress in a large portion of the underlying vertebral body. Further, the large increases in stress and anterior concentration of high-risk tissue in flexion suggests that, for implants of this size, bending to the point of impingement may be a causal factor for subsidence *in vivo.*

The mechanisms underlying the anterior shift in high-risk tissue and the elevated stresses in the anterior cortex when the medium and large implants are loaded in flexion relate to the boundary conditions induced by impingement. For a given implant size and applied force, the stress distribution was impacted much more by the loading mode of the implant (compression versus flexion-induced anterior impingement) than by the implant's material properties. Impingement, defined as contact between secondary, nonbearing surfaces [153] (for example, between the rim of the articulating insert and the metallic footplate, or between two metallic footplates) has been reported to occur in 9–66% of cases [88,89,92] and has been documented for nearly all major device designs (Charité [87,89,90], ProDisc-L [88,92,97], activL [91,93], MobidiscL [91]). When impingement occurs, large loads can be transmitted through the impinged region [14,90,94,96]. Both anterior and posterior impingement are possible for flexion and extension, respectively [88,92,94,96,97]. The current data show that for anterior impingement induced by flexion, the anterior portions of the cortex and underlying trabecular bone must accommodate nearly all of the load for medium and large implants. This shifts the tissue at the highest risk of initial failure to regions adjacent to the impingement. For small implants, the anterior cortex is not involved in load-redistribution induced by flexion.

The geometric detail with which the vertebral body supporting a TDA implant was modeled is novel and enables insight that both complements and extends prior understanding. The impact of implant size has been previously explored by Auerbach et al [139] using pressure film analysis; they found that larger implants decrease contact stress at the bone-implant interface in axial compression compared with smaller implants. Their representative pressure film data appear similar to the current results for a similarly sized implant with respect to the magnitude and spatial distribution of axial stress at the endplate (after linear scaling to an equivalent applied force), thus providing external experimental support for the validity of the model used here. Their results, however, are limited to the analysis of stress for a single loading mode (axial compression) at a superficial region (the bone-implant interface). In contrast, a strength of this study is the elucidation of the stress distribution throughout the vertebral bone tissue as a function of implant size, as well as the interaction between implant size and loading mode. Rundell et al [71] used a quantitative-CT-based finite element model to assess the impact of axial compression, flexion/extension, and lateral bending on vertebral body strains. Their data, consistent with the stress data reported here, suggest that extensive strain redistribution within the vertebral body can occur following TDA for implants of normal clinical size, regardless of loading mode. In particular, they found anterior strain maxima following flexion with an implant which did not occur for flexion with an intact disc, thus corroborating one of the findings of this

study. However, their finite element approach employed elements with 1 mm edge lengths, thereby modeling the vertebral body as an analogous continuum structure and not one comprised of a trabecular structure. While the former may be sufficient to assess macroscopic properties such as vertebral body strength, the latter is more realistic in estimating actual physiologic tissue-level behavior. Further, their boundary conditions included fully fixing the inferior endplate, which neglects the impact of the adjacent disc on strains within the vertebral body. Prior studies have shown that fixing the inferior endplate (e.g. potting in PMMA), will result in a different stress distribution within the vertebra than when loaded via an intact disc [107]. Thus, their reported strain distributions may better approximate *in vitro* experiments in which the vertebral body is potted in PMMA as opposed to *in vivo* behavior in which the bone is loaded inferiorly via a disc, as was done here. Taken together, the fidelity with which the spatially variable trabecular microstructure and thin cortical shell and endplate were modeled, coupled with the combination of implant size, material parameters, and boundary conditions, provides unique insight into the mechanical behavior of the human lumbar vertebral body for this class of implants.

The primary limitations of this study are its use of just a single vertebra and its theoretical nature. Microarchitectural parameters, such as bone volume fraction, vary between specimens and can impact mechanical behavior [119]. However, studies on n = 22 [107] and n = 13 [142] non-osteoporotic human vertebrae show a consistent pattern of cortical-trabecular load-sharing, which was also exhibited by the vertebra studied here. Thus, these results should likely extend to most non-osteoporotic vertebrae, though a larger sample size is necessary to confirm their generality. A substantially lower bone volume fraction representative of osteoporosis might result in different behavior, since structural redundancy is lost with osteoporosis [154]. In part, this may help explain the contraindication of TDA for osteoporotic patients.

A second limitation stems from the purely computational nature of this study. The finite element approach used here has been shown to accurately predict whole vertebral-body and trabecular-core strength compared to experimental values (Appendix 7.9), implying that the dominant structural mechanisms in the bone are well-captured [119,154]. The disc was also modeled as a homogenous isotropic elastic material, thereby neglecting the details of the gelatinous nucleus pulposus and lamellar annulus fibrosus. However, with degeneration, compressive loads are thought to transmit directly through the annulus [102] as the nucleus shifts from a fluid-like to solid-like structure [155]. Thus, in terms of loads experienced by the vertebral body, the annulus-type material properties assigned to the disc should reasonably simulate a state of disc degeneration associated with the aged nature of the vertebra. Further, the prediction of the high-risk tissue distribution for the intact model is consistent with the location of bone failure observed for cadaveric vertebrae loaded via degenerated discs [156,157]. Finally, the implant model omitted the protrusions (such as the spikes or teeth used for fixation) found on real implants. A sensitivity study (Appendix 7.1) indicated that using a higher fidelity implant model that includes protrusions had a negligible effect on reported results and would not alter the conclusions. However, some implants utilize a keel instead of a series of teeth for fixation. Since these keels are large and can extend deep into the vertebral body, it's possible that keeled implants could exhibit fundamentally different behavior than that reported here. Therefore, interpretation of these results should be limited to non-keeled implants.

A planar surface was created superiorly to replicate a TDA procedure [143], which included resection through parts of the osseous endplate. There is clinical agreement that the osseous endplate should be preserved and that only the disc and cartilaginous endplate should be resected during TDA [143,144]. However, it was not possible to create a planar surface without resecting parts of the osseous endplate due to its inherent irregularity. This raises the question of whether complete endplate preservation might have enabled the implants to better replicate the intact model. Results from a prior study (n = 5 L1 vertebrae) indicate that, compared with full endplate preservation, full endplate resection only minorly altered maximum cortical load fraction (decrease of 4%, $p < 0.01$) and had a similarly small effect on high-risk tissue distribution [158]. Therefore, resection likely did not have a large effect on the results. Some endplate resection may be clinically relevant, since the extent to which the cartilaginous endplate (approximately 0.80 mm thick [159,160]) can be intra-operatively resected while fully preserving the osseous endplate (approximately 0.50 mm thick [120]) is unclear. While preserving all of the osseous endplate would result in a slightly larger cortical load fraction, this would not alter the conclusions.

Despite these limitations, these results may have clinical implications. Clinical evidence suggests an etiologic link between implant subsidence and implant impingement [14,87,91,93]. However, the mechanisms underlying this phenomenon are not understood. It has been suggested (but not experimentally demonstrated) that the implant subsidence causes impingement [14,86,91,93]. In other words, it's been suggested that the implant position changes following subsidence which then increases its proclivity to impinge. However, these data suggest the opposite is also feasible—that impingement causes subsidence. The data suggest that flexion-induced anterior impingement substantially increased stress in the bone and concentrated the high-risk tissue to local anterior regions. The 800 N force applied in both compression and bending (approximately 1x body weight [145]) facilitated comparison between models since it enabled isolation of the interaction between size and loading mode. However, the forces on the vertebral body generated *in vivo* during flexion can be two to three times body weight [146,148], since the moment arm caused by the weight of the trunk must be balanced by increasing forces in the erector spinae muscles [161], which increases the reaction force at the vertebra. Scaling the values of stress in flexion two- to three-fold to those better representing the *in vivo* environment (permitted by the linear elastic nature of the study) would generate tissue-level stresses high enough to be of concern for both monotonic and fatigue-related tissue failure [162]. The failure of the bone tissue supporting an implant may be a causal factor for implant subsidence. Therefore, if the magnitude and distribution of tissue-level stress reported here are similar to those which develop *in vivo*, implant designs which impinge may inherently be at risk of overloading the bone in the regions near the impingement. One implication of this finding is that benchtop subsidence tests should incorporate bending-induced impingement to better replicate *in vivo* behavior.

In summary, these findings suggest that implant size has a larger effect on load-transfer behavior within the vertebral body than implant material in both compression and flexion. If impingement following flexion occurs *in vivo*, local stresses in the bone tissue can substantially increase anteriorly in the region adjacent to the impingement. This behavior is accentuated as implant size increases. For the medium implant, whose size is similar to those

used clinically, these elevated stresses are sufficiently high to warrant concern for monotonic or fatigue-related bone failure, which may contribute to clinically observed implant subsidence.

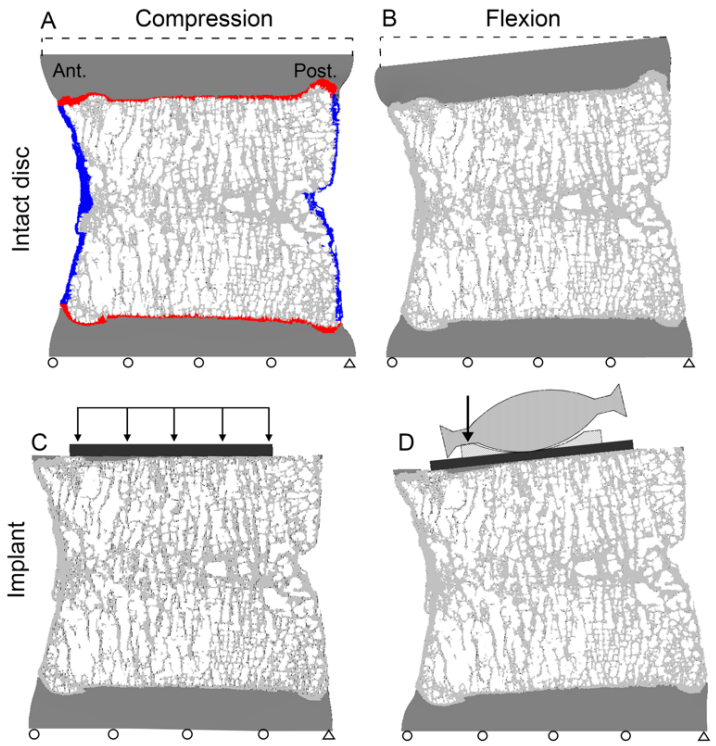

Figure 2–1. Mid-sagittal cross-section (0.5 mm thick) showing (A) the differentiation of trabecular (light grey), cortical (blue), and endplate (red) tissue. Boundary conditions and displaced shapes are shown for the (A) intact disc in compression (B) intact disc in flexion (C) implant in compression and (D) implant in flexion. The implant components depicted above the footplate in (D) were not explicitly modeled but are shown to illustrate impingement which motivates the flexion boundary conditions.

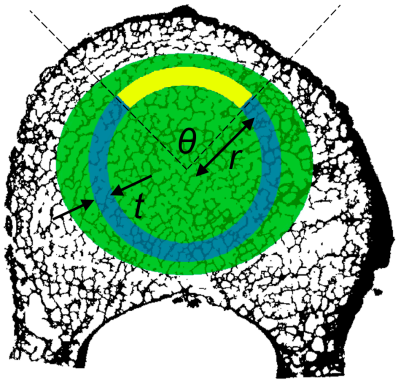

Figure 2–2. Flexion of an implanted segment was modeled by applying a force through an arc (yellow) to simulate impingement. θ = 90°, t = 2 mm, r = 40% of the footplate A/P diameter.

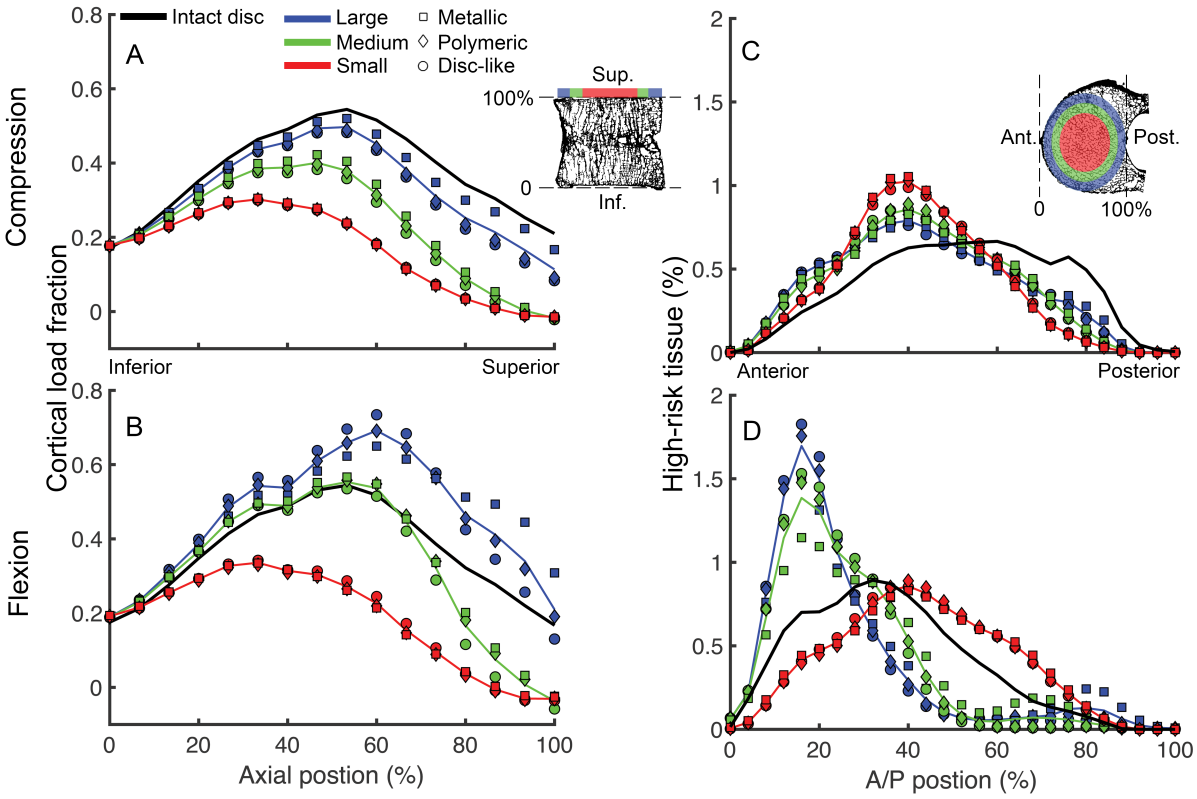

Figure 2–3. Left: The cortical load fraction for compression and flexion as a function of axial position in the vertebral body. Right: The relative volume of high-risk tissue for compression and flexion as a function of A/P position in the vertebral body.

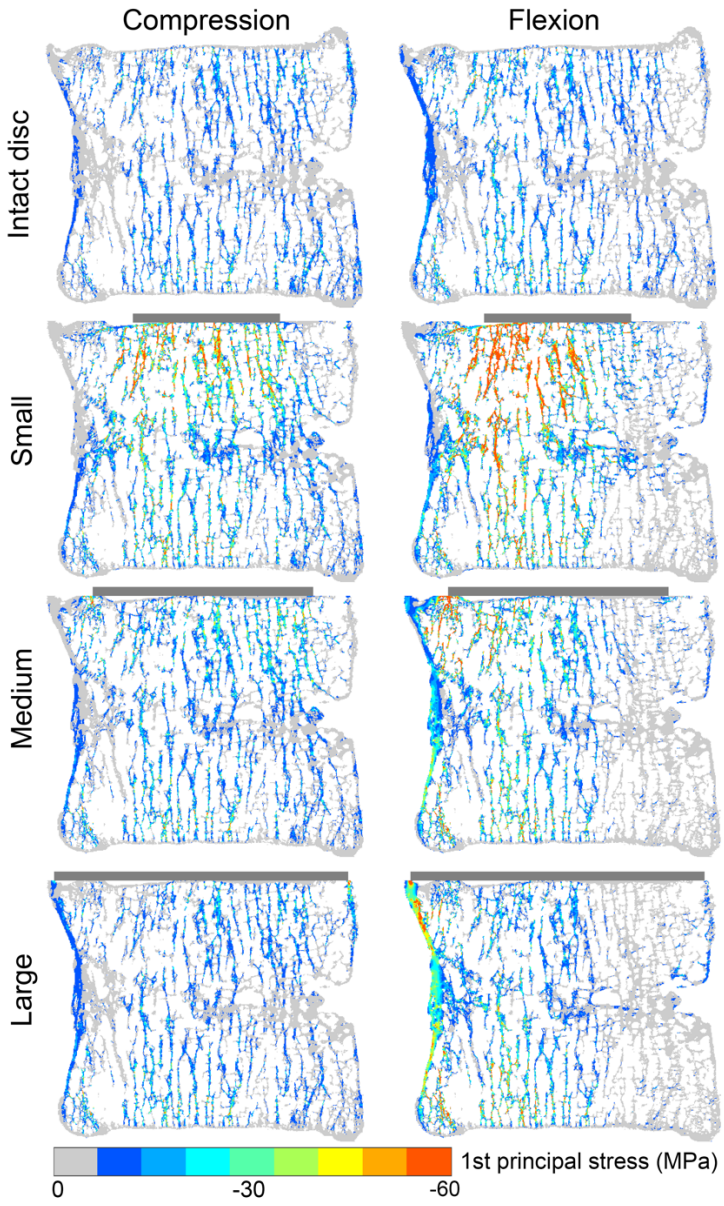

Figure 2–4. Minimum principal stress (MPa) in the bone tissue at a mid-sagittal cross-section (0.5 mm thick) for the intact disc and metallic implant models in compression (left) and flexion (right). Other implant materials were omitted for clarity.

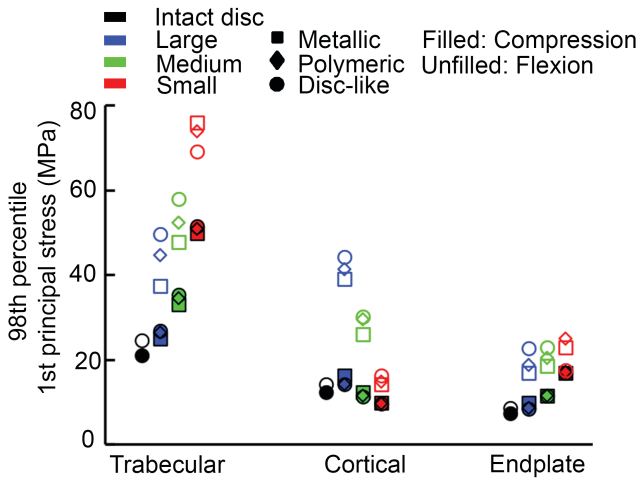

Figure 2–5. 98th percentile of the minimum principal stress (MPa) in the bone tissue, differentiated by compartment, for all models.

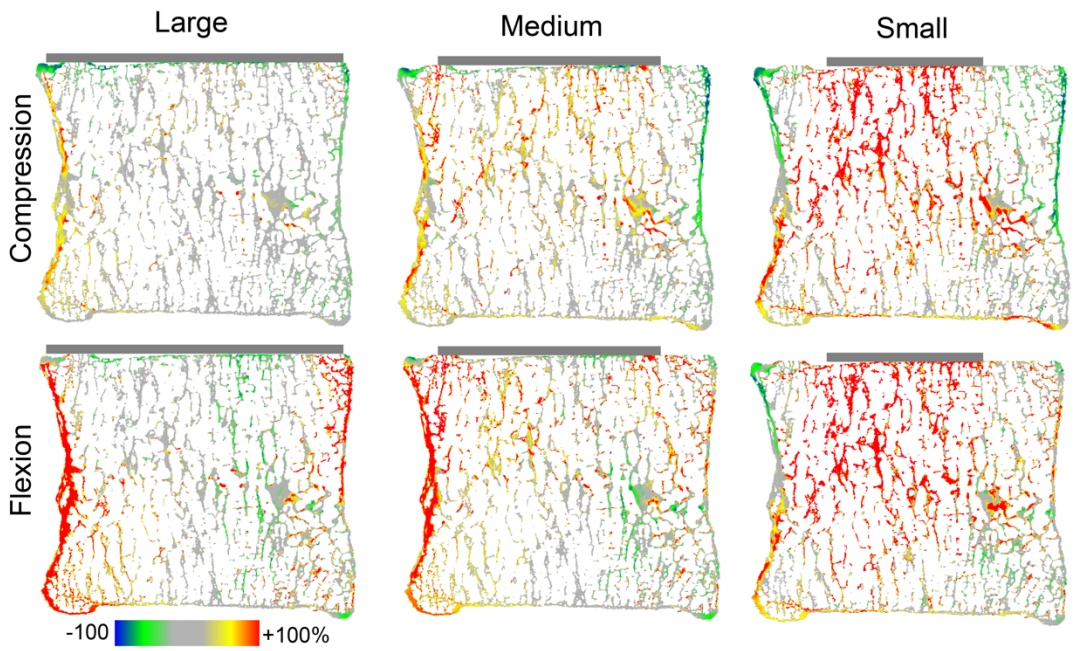

Figure 2–6. Mid-sagittal cross-section (0.25 mm thick) showing the percent difference in von Mises stress between the intact disc model and metallic implant models in compression (top) and flexion (bottom). Other implant materials were omitted for clarity. Positive differences denote higher stresses for the implant models compared to the intact disc.

3. The role of bone porosity and loading mode on tissue-level stress in the human vertebral body following lumbar total disc arthroplasty

3.1 Introduction

Lumbar total disc arthroplasty (TDA) implants are designed to treat the pain associated with end-stage degenerative disc disease while preserving segmental motion. Despite some evidence that TDA can improve clinical outcomes relative to lumbar fusion [29,30], the procedure is narrowly indicated [25–27] and has not been widely adopted in the United States [79]. Complications such as implant subsidence, migration, and fracture of the vertebral body or pedicles may be related to the bone biomechanics in the vertebral body supporting a TDA implant [8,9,165,13,20–22,24,150,163,164]. However, the bone biomechanics for this general class of implant are not fully understood; for example, it remains unclear how the stresses that develop in the underlying bone tissue depend on the loading mode (e.g. compression versus bending) or on typical inter-individual variations in the porosity of the vertebral body [71,98,165,166].

Low bone mineral density (BMD) can reflect increased porosity and has been associated with a lower vertebral failure force and implant subsidence [25,137,165,167,168]. Bone mineral density is therefore measured clinically prior to TDA surgery, typically using dual-energy x-ray absorptiometry (DXA) [167]. The DXA-based measurements of bone density then inform the clinical treatment; for example, osteoporosis (T-score < -2.5 SD, as measured by DXA [169]) is frequently considered a contra-indication for TDA [26,27,84,170]. However, other studies [24,171–173] have used osteopenia (T-score < -1.0 SD) instead of osteoporosis as the cutoff value for TDA, indicating a discrepancy in the literature as to the appropriate clinical exclusion criteria. DXA itself also has limitations; notably, DXA's projectional measurements summate the cortical-rich posterior elements with the trabecular-rich vertebral body, thereby obscuring changes within the vertebral body's trabecular centrum which could be important to implant subsidence behavior [165,166,169,174]. These issues highlight the need to more fully understand the biomechanical changes induced by TDA implantation on the underlying vertebral bone as well as the dependence of these changes on variations in vertebral morphology. To date there are no cadaver studies on human vertebrae that have related the presence and loading mode of a TDA implant with vertebral bone-tissue stress across a range of vertebral porosities and morphologies.

In the previous chapter, micro-computed tomography (micro-CT) data and finite element analysis was used to investigate flexion-induced impingement with a TDA implant in order to elucidate the mechanisms by which vertebral bone stresses develop after TDA [166]. The results suggested that bending-induced impingement may redistribute stress within the vertebral body and generate high levels of stress that could increase the risk of implant subsidence. However, that prior work was conducted on a single vertebral body and therefore did not address the role of vertebral porosity on bone stresses. The goals of the current study were to: (1) assess the relationship between bone porosity and maximum levels of bone stress within human lumbar vertebrae following TDA using high-resolution imaging coupled with finite element analysis; and (2) determine whether the loading mode of the TDA implant (axial compression versus

sagittal bending) alters the relationship between bone porosity and maximum levels of bone stress.

Elucidating these fundamental biomechanical issues may help inform implant designs and *in vitro* test protocols for device development and regulation. An improved biomechanical understanding may also help clarify appropriate clinical indications and could ultimately help improve clinical outcomes for this theoretically promising class of implant.

3.2 Methods

Study Design

Using existing data from micro-CT scans, twelve cadaveric human lumbar vertebral bodies were virtually implanted with generically shaped elliptical TDA footplates. Each implant was virtually loaded to 800 N of applied force in three separate ways via linearly elastic finite element analysis: axial compression, flexion-induced anterior impingement, and extension-induced posterior impingement. The main outcome was the maximum level of stress that developed in the underlying vertebral bone tissue. Elliptical plates were chosen to represent generic implant footplates, thereby assuming that subtle details of implant geometry have a secondary effect on tissue-level stress relative to footplate size (Appendix 7.3). For each vertebra, elliptical dimensions were chosen to represent a clinically reasonable footplate size for that specimen. To compare the effect of implantation with the expected physiologic distribution of stress in the bone tissue, compression, flexion, and extension of the un-implanted vertebrae were also simulated by loading the vertebral bodies via a disc-like material without an implant.

Specimen Preparation and Micro-CT Scanning

Pre-existing micro-CT data from twelve human L1 vertebral bodies from de-identified cadavers without a history of metabolic bone disorder (age = 71 [51 – 89] years of age, mean [range], Table 3–1) were analyzed in this study. The micro-CT image data had an isotropic voxel size of 37 μm. The posterior elements were virtually removed to isolate the vertebral body before the hard tissue and marrow were segmented using a global threshold value. Using the thresholded data, bone volume fraction (BV/TV = 1 – porosity) was measured using a 15 x 15 x 20 mm internal cuboid (length x width x height) of trabecular bone via the BoneJ plugin in ImageJ (v.2.0) [175,176].

Finite Element Analysis

Each 37 μm voxel in the thresholded scan was converted into an eight-noded hexahedral finite element. At this resolution, approximately four finite elements (on average) span the thickness of each individual trabecula (average trabecular thickness = 170 ± 37 μm, mean ± SD). This resolution both captures the geometrically complex, patient-specific trabecular microstructure and helps ensure the numerical convergence of tissue-level strains [132].

Elliptical TDA footplates (2.3 mm thick), also modeled using voxels, were placed on the inferior endplate of the vertebra such that the implant center coincided with the anterior-posterior (A/P) and medial-lateral (M/L) midpoint of the vertebral body. The footplates were assigned

material properties similar to cobalt-chromium (E = 210 GPa, ν = 0.33 [177]). A footplate size representing a likely clinical size was selected for each specimen. To do this, five footplate sizes were generated with major and minor diameters (corresponding to M/L and A/P dimensions, respectively) matching that of the five Charité implant sizes (Table 3–1) [152]. While the Charité implant is no longer used [6], it was chosen as the predicate model for two reasons: the clinically-used sizes span a larger dimensional range than other predicate devices (ProDisc-L, Maverick, ActivL, Mobidisc); and other predicate devices are only available in at most four sizes—a fifth size theoretically enables a higher fidelity fit for each verterbra [152]. Gstoettner et al [152] reported that clinically-used TDA footplates (of various designs) are diametrically smaller than the underlying bony endplate by an average of 8.5 mm in the A/P dimension. Therefore, after measuring the bony endplate using a similar methodology, the footplate size was selected which most closely replicated an 8.5 mm diametrical difference between the footplate and the underlying bony endplate.

To simulate compressive loading with a TDA implant, an 800 N uniform force (approximately 1**x** body weight and a typical force at that spinal level for static standing [145,146]) was applied to a central circular region of the footplate, representing load transfer into the footplate through an insert (Figure 3–1). To simulate bending with an implant, impingement between the footplate and the insert induced by flexion and extension was modeled. There is evidence that impingement occurs in sagittal bending for both unconstrained and semi-constrained devices [14,86,91–96]. Analysis of retrieved implants and *in vitro* experiments suggest that large loads can be transmitted through the impinged regions during bending and can damage the ultra-high molecular weight polyethylene (UHMWPE) inserts [14,86–91,94]. Therefore, flexion- and extension-induced impingement were modeled by applying a uniform compressive force of 800 N to a 2 mm thick, 90° arc of the footplate, as described in detail in Chapter 2.

To simulate compressive loading with an intact disc, a uniform compressive boundary condition was applied to the inferior disc (Figure 3–1). Following calculation of the finite element solution, results were scaled linearly to produce a net reaction force of 800 N. To simulate flexion and extension of an intact disc, a displacement boundary condition was used to rotate the disc in the mid-sagittal plane about the far posterior- or anterior-inferior point, thereby simulating flexion and extension, respectively, over a single motion segment [107,147]. Results were then scaled linearly to produce a net reaction force of 800 N. While bending (particularly flexion) can increase compressive forces on the spine two- to three-fold compared to what was modeled here [146,148], a fixed reaction force of 800 N was maintained for all loading modes in order to facilitate a controlled comparison across models.

For all models, an intervertebral disc-like material was modeled superiorly using a symmetry (roller-type) boundary condition applied to the top of a 4-mm-thick disc, thereby simulating an 8-mm-thick disc with unconstrained bulging. Disc elements were assigned homogenous material properties consistent with the measured effective modulus of an aged disc at a low rate of loading (E = 8 MPa, ν = 0.45) [106]. All bone elements were assigned the same linearly elastic material properties (E = 10.3 GPa, ν = 0.30) [149]. Perfect bonding was assumed at all interfaces, thereby modeling full footplate fixation in the bone.

On average, each analysis comprised approximately one billion degrees of freedom (range $5.6 \times 10^8 - 1.5 \times 10^9$ degrees of freedom, depending on the bone). Solving models of this size required a custom finite element code including a parallel mesh partitioner and an algebraic multi-grid solver [134] implemented on an 18-petaflop supercomputing cluster (Stampede2, Texas Advanced Computing Center, Austin, Texas). A typical analysis utilized 3600 Intel Xeon Platinum 8160 processors (75 compute nodes) in parallel and 14 terabytes of memory. A total of 72 analyses were run, consuming a total single-processor-equivalent CPU time of approximately 22 years.

Outcomes

The primary outcome was the highest magnitude of stress within the bone tissue of each implanted vertebra at three region-of-interest locations in the vertebral body: near the implant, in the middle of the vertebral body, and far from the implant (locations A, B, and C, respectively; Figure 3–1). At each location, the maximum stress was quantified by calculating the 98^{th} percentile of minimum principal stress in a 1 mm- (27 element-) thick entire transverse cross-section. The absolute change in maximum stress was calculated by subtracting the maximum stress values from the same vertebra loaded in the same loading mode but without an implant (positive values imply stresses increased for the TDA-implanted vertebra compared to the intact vertebra). A general linear regression model was then used to determine the dependence of this change in maximum stress on loading mode, bone volume fraction, and their interaction, at each location—A, B and C—in the vertebral body.

A second outcome was a quantitative measure of the proportion of "high-risk" tissue, and where that high-risk tissue occurred spatially in the bone. The high-risk tissue is interpreted as the bone tissue that is most likely to fail first and was identified by first taking the ratio of the maximum and minimum principal stresses of each bone element (calculated at the element's centroid) to the assumed tensile (61 MPa) or compressive (150 MPa) bone-tissue yield stress, depending on the sign of the principal stress (i.e., positive principal stresses were normalized by the tensile yield stress) [119]. For each bone element, the higher value of this ratio was then used to rank values across all bone elements: the high-risk tissue was identified as the top 10% of values within the entire vertebral body [107,129]. For each vertebra, the amount of high-risk tissue was then quantified for successive frontal sections along the A/P direction [107]. The mean ± 95% confidence interval values for all vertebrae were then plotted versus A/P position to describe how the spatial distribution of high-risk tissue was altered by TDA implantation and the implant's loading mode.

Statistical analyses were performed in JMP Pro (v. 15.0) and significance was reported for $p < 0.05$.

3.3 Results

For all loading modes and across all vertebrae, loading via a TDA implant increased the maximum stress levels that developed in the vertebral bone tissue relative to loading via an intact disc, particularly near the implant interface (location A, Figure 3–2 lower row). Near the interface, the absolute increase in maximum stress (implant value minus intact value) was greater

for vertebrae with lower bone volume fractions ($p = 0.002$); that is, implantation caused maximum stress to increase more in more porous bones. This change in maximum stress also depended on loading mode ($p < 0.001$), increasing across the 12 vertebrae by an average factor (implant value divided by intact value) of 1.7 (95% CI: 1.6–1.8), 2.1 (1.9–2.4), and 2.7 (2.3–3.1) for compression, flexion and extension loading, respectively. Representing a statistically significant interaction between the effects of bone volume fraction and loading mode ($p = 0.002$), maximum stress near the interface increased more in the more porous vertebrae loaded in bending (either flexion or extension).

Away from the implant interface, the effects of implantation persisted but were of much lower magnitude. For example, midway into the vertebral body (at location B) the maximum stress levels were significantly higher for the implanted relative to the intact models ($p < 0.001$ across loading modes) but the effect size was much small than near the interface (absolute change in maximum stress < 32 MPa across all vertebrae and loading modes).

Quantitative analysis of the spatial distribution of high-risk tissue indicated that loading via bending-induced impingement (either flexion or extension) accentuated the concentration of high-risk tissue towards the direction of bending (Figure 3–3). For the intact disc, bending skewed the high-risk tissue distribution in the direction of bending, and this effect was greater for the implanted models. These trends were similar for flexion and extension. Images of high-risk tissue within the vertebra indicated that flexion tended to increase the amount of high-risk tissue in the cortical shell. This general shift in the distribution of high-risk tissue was consistent across specimens despite the wide range of vertebral morphologies and bone volume fractions, as evident from the narrow nature of the 95% confidence intervals of the mean value of proportion of high-risk tissue at each A/P position (Figure 3–3).

3.4 Discussion

These results help elucidate how the stress that develops in the vertebral bone tissue supporting a TDA implant depends on inter-individual variations in bone porosity across patients, as well as the overall loading mode (e.g. compression versus bending-induced impingement with an implant). Results show that more porous bones (i.e. those with lower bone volume fractions) not only developed higher stresses than less porous bones but were preferentially affected by TDA implantation: the absolute increases in bone stress caused by implantation were of much larger magnitude for higher porosity vertebrae than for lower porosity vertebrae. This effect was accentuated for impingement induced by bending, even though a fixed 800 N compressive force was applied to all bones in both axial compression and sagittal bending. As expected, tissue-level bone stresses were higher in more porous vertebrae, presumably because those vertebrae have less bone tissue to sustain the applied force; this finding is consistent with clinical concerns about performing TDA in patients with low apparent bone density [25]. However, the data also suggest that for patients with already low bone density or those who may lose appreciable bone density with age, TDA may disproportionately increase already high levels of bone stress. In conclusion, a typically sized TDA implant can substantially increase local stresses in the underlying vertebral bone tissue compared to loading via an intact disc, and this effect is accentuated in patients with lower trabecular bone density, especially for impingement induced by sagittal bending.

Although this study was purely computational in nature, the geometric fidelity with vertebral bone was modeled and the parametric and comparative nature of the results supports the plausibility the main findings. The micro-CT data upon which these finite element models are based capture the primary structural (non-molecular) aspects of bone quality, such as the connectivity and structural anisotropy of the trabecular microstructure and the morphology of the non-uniform cortical shell and endplates. Modeling these features explicitly—and conducting repeated measurements on the same sample to calculate a specimen-specific difference in stress—make the relative predictions of tissue-level stress changes robust and also insensitive to uncertainties in bone-tissue elastic modulus (Appendix 7.4). As such, the model results represent a highly detailed biomechanical analysis of what should occur in the vertebral bone tissue for this class of implant.

Further support of these results is provided by the consistency of the findings with prior studies. In a computational study, Rundell et al [71] used a quantitative-computed tomography-based finite element model to assess the impact of axial compression, flexion/extension, and lateral bending on vertebral body strains. Their data indicate strain maxima at the anterior edge of the vertebral body following flexion with an implant, corroborating one of the findings of the current study. Based on those findings, the authors also suggested that subsidence may be caused by activities which put the segment in flexion [71]. In a physical biomechanical study, Semitela et al [98] measured strains on the exterior of a vertebral body surrogate model fabricated from polyurethane and loaded experimentally via a TDA implant. They found that implantation substantially increased cortical strain, also consistent also with the current findings related to elevated stress and high-risk tissue in the cortical shell. The current analysis extends those studies by accounting for the real microstructural details of the trabecular bone and the cortical shell, enabling a more accurate estimation of both stress and specimen-specific stress changes in the bone tissue caused by implantation. Additionally, the data presented here are novel in that they address heterogeneity across human vertebral bone, a potentially important clinical issue. Doing so enabled discovery that the magnitude of the stress increase caused by implantation depends on trabecular bone porosity; that is, the already high stress in more porous vertebrae is disproportionately increased by loading via an implant.

Despite these positive aspects of this study, there are some limitations and caveats. First, patient-specific loading was not accounted for. The 800 N force applied to all specimens facilitated a controlled comparison by enabling isolation of the effects of loading mode and bone volume fraction without a further confounding variable of load magnitude. *In vivo* stress levels across vertebrae would be expected to vary in live subjects along with the magnitudes of patient-specific *in vivo* forces acting on the vertebrae, likely in proportion to body weight and level of physical activity. However, since the main outcomes were reported as relative changes within the same vertebrae from intact to implanted states, these conclusions should remain robust in the light of these *in vivo* variations. Indeed, some estimates of maximum stress levels are likely conservative. For example, the compressive force acting through the disc on the vertebral body for certain weight-bearing bending activities can be two- to three-times the approximately one-times bodyweight applied here [146,148,161]. Scaling the values of stress in bending two- to three-fold (permitted by the linearly elastic nature of the study) would increase both the absolute value and the absolute difference in maximum tissue-level stress between compression and

bending, and between implanted versus intact conditions. Therefore, the current results are likely conservative and should reflect a lower bound of the possible effects.

A second caveat is that the main outcomes have not been experimentally validated due to the technical challenge of directly measuring tissue-level stresses or strains in trabecular bone within a vertebral body. However, this finite element approach has been shown to accurately predict whole vertebral-body and trabecular-core strength compared to experimental values, implying that the dominant structural mechanisms in the bone itself are well captured by this high-resolution modeling approach [119,154,178]. In modeling the disc, the effective elastic uniform and isotropic properties were used that were directly measured and validated in cadaver experiments conducted on aged discs at a low rate of loading [106]. Despite this simplified modeling of the disc, the prediction of high-risk tissue distribution for the intact model is consistent with the location of bone failure observed for cadaveric vertebrae loaded via degenerated discs [156,157], suggesting that the approach used adequately captures the primary effects of how human discs consistent with donor demographics load the underlying vertebral bone. In modeling the trabecular tissue, an assumed a uniform isotropic value of its effective elastic modulus was used, again based on results from biomechanical testing experiments [149]. While the bone-tissue material properties are not known with certainty, it was confirmed with additional parameter studies that the outcomes were insensitive to uncertainties in tissue modulus over a realistic physiologic range (Appendix 7.4).

A third limitation relates to the aged nature of the specimens. Nine of the twelve cadavers were older than sixty years-of-age, putting them above a commonly suggested upper age limit for TDA candidacy [25,179]. However, the micro-CT data used to construct the models are agnostic to all patient factors except the geometric properties of the bone and were assigned the same average tissue-level material properties. Thus, the data should reasonably represent general behavior within the range of vertebral geometries and bone volume fractions displayed in the sample. Regardless, patients who underwent TDA surgery prior to age sixty will advance in age and may lose bone mass; therefore, elucidating fundamental mechanisms relating bone density with vertebral bone stresses is important for specimens of all ages and on each side of the age- and density-related clinical cutoff criteria. Related, while the sample size was small (n = 12), it was sufficiently large to represent real variations in the micro- and macro-scale geometric properties of human lumbar vertebrae. In addition, the small confidence intervals on the main outcomes confirm the sample size was also sufficiently large to demonstrate statistically significant effects of the primary parameters.

Despite these limitations, these results may have clinical implications. The maximum stress level that developed for any un-implanted vertebra loaded via an intact disc did not exceed 85 MPa, regardless of the loading mode or bone volume fraction. Presumably, that level of stress represents an approximate upper limit of the physiologic stresses that can develop in the bone tissue for a fixed 800 N applied force over the range of volume fractions tested. When loaded via a TDA implant with the same fixed 800 N force, stresses typically exceeded 85 MPa whenever the vertebra had a bone volume fraction of 0.10 or below and was loaded in bending-induced impingement. This bone volume fraction of 0.10 corresponds to an estimated quantitative-computed-tomography- (QCT-) measured volumetric bone mineral density (vBMD) of approximately 106 mg/cm^3 (Appendix 7.5); which in turn corresponds clinically to osteopenia

per the American College of Radiology clinical practice criteria (osteopenia: > 80 to < 120 mg/cm^3; osteoporosis: ≤ 80 mg/cm^3) [169]. Without a TDA implant, the risk of a future vertebral fracture is high or increased in patients with osteoporosis or osteopenia, respectively [180]. Since the failure of the bone tissue supporting an implant may be a causal factor for implant subsidence, data indicating a disproportionate increase in bone stress for these low density patients with already compromised bone strength suggests that all osteoporotic patients may be at risk of implant subsidence, particularly if there is any bending-induced impingement. Notably, the data also suggest that patients with osteopenia may be at risk, consistent with other recommendations [25]. Prophylactic vertebroplasty can be done simultaneously with TDA implantation; this topic is a promising direction of future research since little information exists to date justifying the approach [137,165].

Related to the implant's design, the results suggest that pre-clinical testing of TDA implants might also include some form of evaluation of bending-induced impingement if such loading is possible *in vivo*. Several studies have suggested that impingement occurs following a change in implant position caused by subsidence [14,86,91,93]; however, the mechanistic etiologic factors linking impingement with subsidence have not been established experimentally. Whether subsidence occurs prior to impingement remains unclear and likely depends on details of the implant design as well as surgical placement. Regardless, the results shown here suggest that if impingement does occur, it can substantially increase the stress, especially in more porous vertebrae, and may therefore cause subsidence. Thus, as has been recommended for *in vitro* wear testing [86,94,96], *in vitro* subsidence testing for TDA implants should also include an impingement load case, and also account for variations in bone porosity, since the effects of TDA implantation depend on the combined effects of loading mode and bone porosity.

Table 3–1. Sample demographic data (n = 12) and implant sizes. The major and minor elliptical diameters of the footplates (M/L and A/P dimensions, respectively) correspond to the dimensions of the five Charité III footplate sizes. BV/TV = bone volume fraction.

Age (years)	Sex	BV/TV	TDA diameter (mm) M/L	A/P	Size
51	M	0.120	28.5	23.0	1
54	M	0.134	28.5	23.0	1
55	F	0.087	28.5	23.0	1
61	M	0.103	42.5	31.0	5
66	M	0.145	38.5	29.0	4
70	M	0.115	35.5	27.0	3
71	M	0.106	35.5	27.0	3
80	M	0.098	31.5	25.0	2
82	F	0.060	28.5	23.0	1
86	F	0.127	28.5	23.0	1
89	F	0.073	28.5	23.0	1
89	M	0.086	35.5	27.0	3

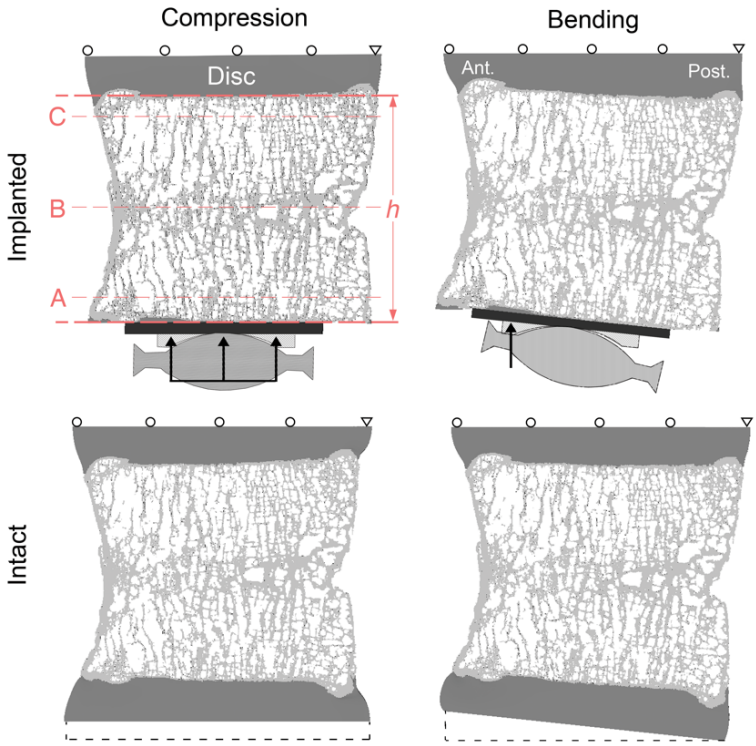

Figure 3–1. Mid-sagittal cross-section (0.5 mm thick) showing boundary conditions and displaced shapes for implanted (top) and intact (bottom) cases in compression (left) and bending (right [flexion pictured]). Locations A, B, and C (red) are located at a distance from the bone/implant interface equivalent 10%, 50%, and 90% of the vertebral body height, respectively (0.1h, 0.5h, and 0.9h). The implant components depicted above the footplate were not explicitly modeled but are shown to illustrate impingement motivating the bending boundary conditions.

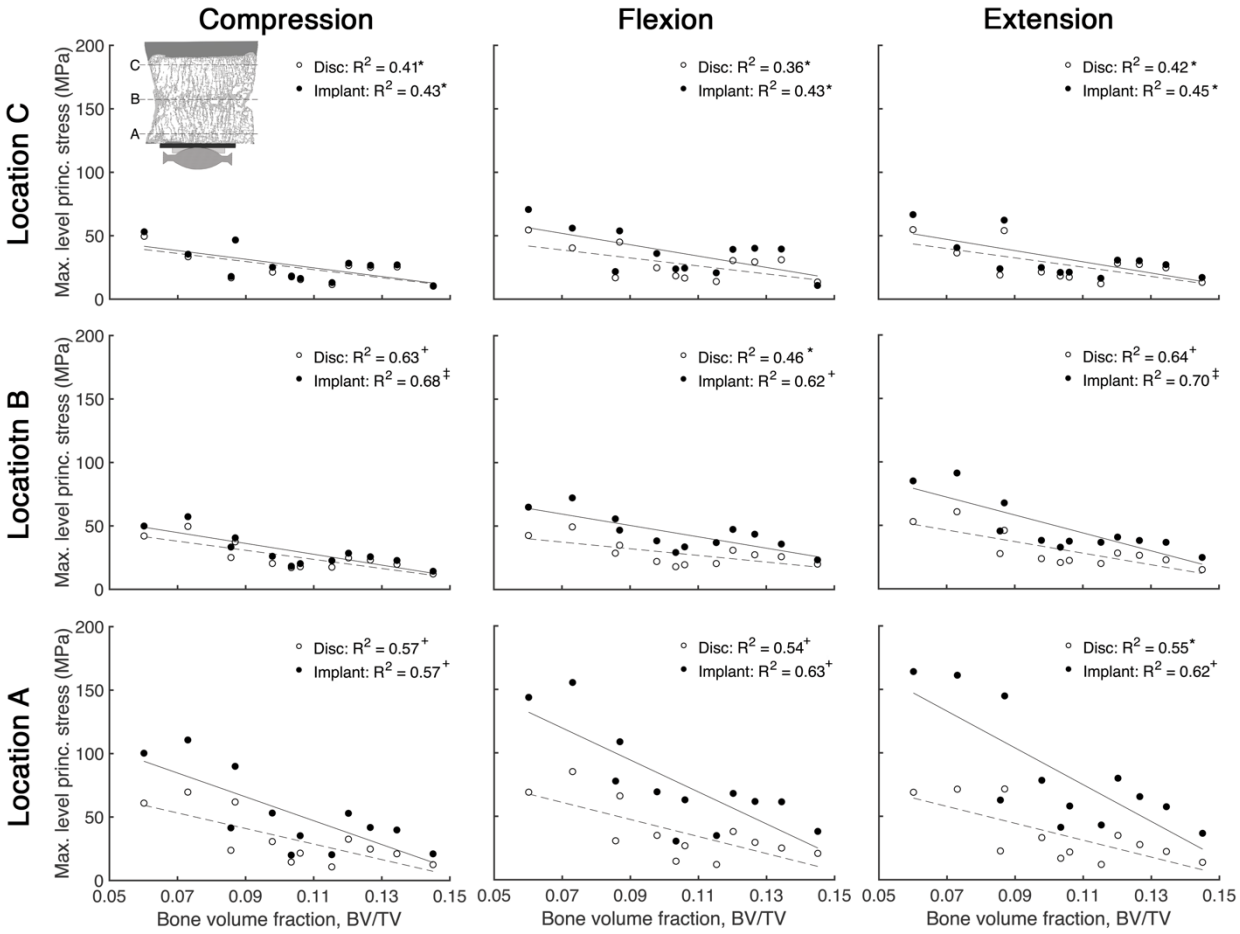

Figure 3–2. Maximum stress level (98th percentile of minimum principal stress) as a function of BV/TV for all loading modes, at three one-millimeter-thick transverse sections. Locations A, B, and C are located near the implant, in the middle of the vertebral body, and far from the implant, respectively (described in more detail in Figure 3–1). *, +, ‡ denote $p < 0.05$, 0.01, 0.001, respectively.

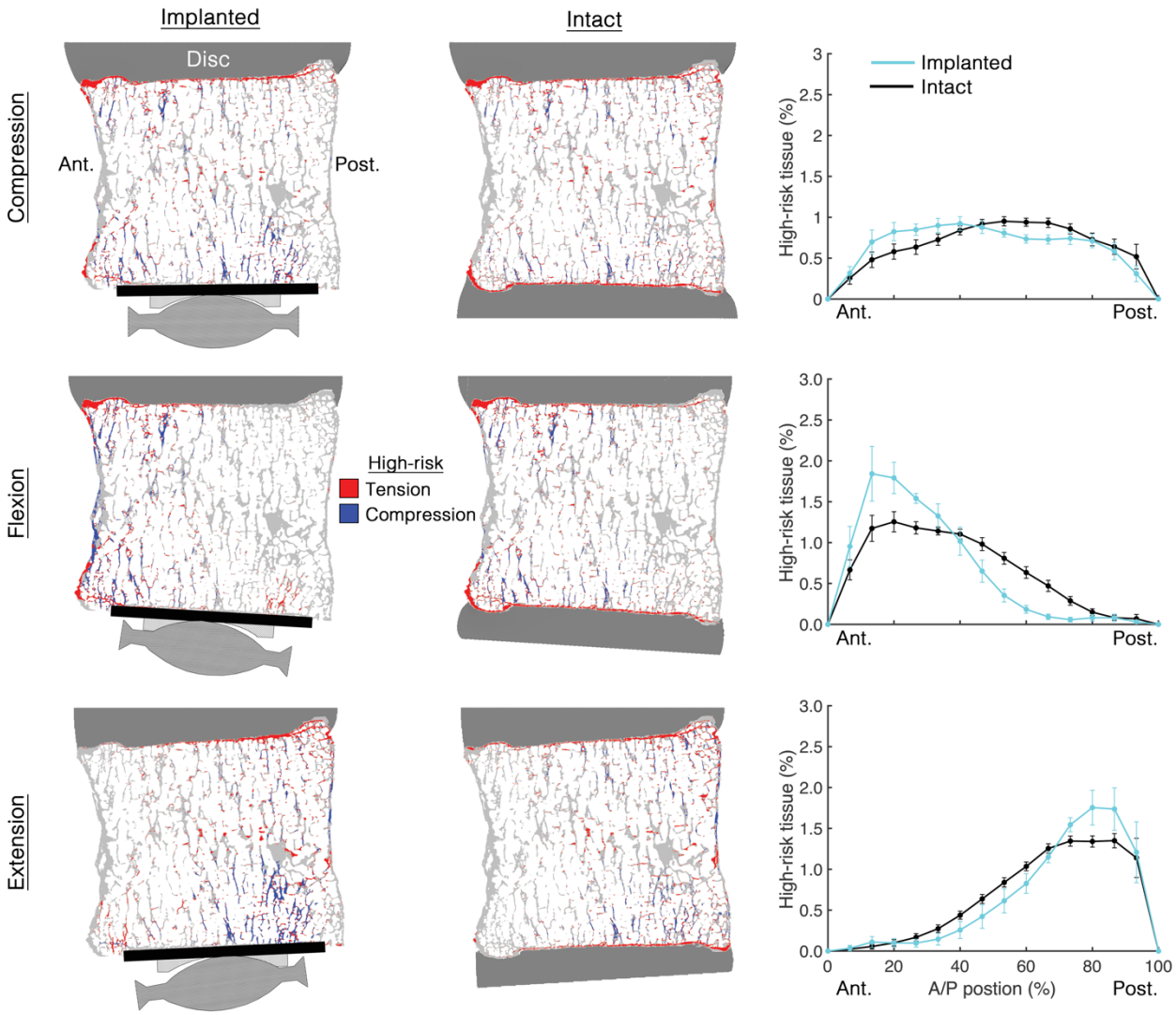

Figure 3–3. Mid-sagittal cross-sections (0.5 mm thick) showing the spatial distribution of the high-risk tissue for one specimen (BV/TV = 0.098) in each loading mode. Far right: Proportion of high-risk tissue (high-risk tissue volume relative to total tissue volume) as a function of A/P position. Values reported are the mean across all 12 specimens; error bars represent the 95% CI of the mean.

4. The role of bone microstructure and loading mode on vertebral strength following lumbar total disc arthroplasty

4.1 Introduction

Largely due to concerns related to implant subsidence and vertebral fracture, pathologically low bone density is a contraindication to total disc arthroplasty (TDA) [25]. However, there is no consensus as to the appropriate clinical exclusion criteria: many clinical trials and other studies have used osteoporosis [170,181–183] as the cutoff threshold (DXA T-score of < -2.5 SD according to the World Health Organization [184]) while others have used osteopenia (DXA T-score < -1.0 SD) [77,171,172,185]. In part, this discrepancy arises because it's unclear how the morphology of the vertebral body (including its trabecular bone volume fraction, total bone mineral content, cortical shell thickness, etc.) relates to the bone's failure strength when loaded by a TDA implant [71,139,140,165,186]. These uncertainties obscure possible strategies that could help reduce subsidence risk; indeed, subsidence remains one of the most frequently documented complications for this class of implant [9,10,23,30,187].

Low bone mineral density (BMD) is associated with a lower vertebral strength when the vertebral body is loaded via an intervertebral disc and via an interbody implant [139,165,174]. In clinical practice and in many biomechanical experiments, BMD is measured using either dual-energy x-ray absorptiometry (DXA) or quantitative computed tomography (QCT) [25,140,165,174,186]. While QCT may offer advantages over DXA in the study of bone-implant biomechanics [174]—namely, QCT can provide more focused measurements of the trabecular bone mineral density within the vertebral body itself—both QCT- and DXA-based measurements rely on region-averaged properties and do not accurately capture the three dimensional geometric details of the trabecular microarchitecture, thin cortical shell, or porous endplates [139]. There are no studies relating the yield strength of the vertebral body loaded via a TDA implant to the microstructural details of the underlying vertebral body; thus, it remains unclear which factors of the bone—aside from apparent bone mineral density—might pre-dispose a patient to subsidence.

Micro-computed tomography (micro-CT) is an established pre-clinical tool which, unlike QCT or DXA, can accurately image the geometric details of the vertebral microstructure in three dimensions. This imaging modality has had a substantial impact on the bone biomechanics field because finite element models based on micro-CT data intrinsically incorporate the complete morphometry of the calcified bone tissue, including the structural anisotropy, spatial heterogeneity, and connectivity of the trabecular microstructure [128]. Micro-CT based finite element models have been used to accurately predict whole-bone strength and relate microstructural metrics with bone failure behavior in the hip and the spine [108,119,178]. This approach has not been used previously to measure the yield strength of TDA-implanted vertebrae; such experiments could help elucidate the mechanisms of subsidence—for example, helping to explain why patients with similar QCT- or DXA-measured apparent bone mineral densities might have substantially different bone strengths following TDA.

The purposes of this study are to: (1) assess which morphological parameters of the human lumbar vertebral body are associated with whole-bone yield strength when loaded via a

TDA implant; (2) determine the parameters associated with a specimen-specific change in yield strength induced by implantation; and (3) assess whether the vertebral-body yield strength depends on the loading mode of the implant; that is, whether the yield strength differs when the implant is loaded in axial compression versus flexion- or extension-induced impingement.

4.2 Methods

Study Design

Using data from micro-CT scans, twelve cadaveric human lumbar vertebral bodies spanning a wide range of morphological characteristics were virtually implanted with single level, typically sized and generically shaped elliptical TDA footplates; potted at the opposite end in polymethyl methacrylate (PMMA) bone cement; and virtually loaded to failure via nonlinear finite element analysis. The yield strength of each vertebral body was calculated following loading via an implant in three separate loading modes: axial compression, flexion-induced anterior impingement, and extension-induced posterior impingement. Elliptical plates were chosen to represent generic implant footplates, thereby assuming that subtle details of the implant geometry have a secondary effect on whole-bone failure strength relative to footplate size (Appendix 7.6). For each vertebra, elliptical dimensions were chosen to represent a clinically reasonable footplate size for that specimen. To measure the change in yield strength caused by implantation, each vertebral body was also loaded to failure in compression via PMMA on both ends (without an implant) and the yield strength of this model was used as a specimen-specific control value.

Specimen Preparation and Micro-CT Scanning

The micro-CT data from a separate study* on twelve human L1 vertebral bodies from de-identified cadavers without a history of metabolic bone disorder (age = 71 [51–89] years, mean [range], Table 4–1) were used in this study. The micro-CT scans had an isotropic voxel size of 37 μm. The posterior elements were virtually removed to isolate the vertebral body before the hard tissue and marrow were segmented using a global threshold value.

Using the thresholded data and the native scan resolution of 37 μm, bone microarchitectural parameters including trabecular bone volume fraction (BV/TV), mean trabecular thickness (Tb.Th), mean trabecular spacing (Tb.Sp), mean trabecular connectivity density (Conn.D), and mean ellipsoid factor (Tb.EF > 0 denotes rod-like trabeculae whereas Tb.EF < 0 denotes plate-like trabeculae) were measured using a 15 x 15 x 20 mm internal cuboid of trabecular bone via the BoneJ plugin in ImageJ (v.2.0) [175,176]. Ellipsoid factor was chosen to quantify the rod- versus plate-like geometry of the trabecular bone because it is less sensitive than structural model index (SMI) to measurement errors caused by concave regions of the trabeculae [116,117]. The micro-CT data were segmented into trabecular, cortical, and endplate compartments using custom ray-based search algorithms described elsewhere (IDL v. 6.2) [142]. Using the segmented image information, the cortical shell mass fraction (Ct.M = cortical shell mass / total bone mass) was calculated in the transverse region excluding the

* Data not yet published

endplates [108,142]. The average cortical shell thickness (Ct.Th) was measured algorithmically (MATLAB R2018b) anteriorly, posteriorly, and laterally at each transverse cross-section of the micro-CT scan (also in the transverse region excluding the endplates) and then averaged [108,142]. The total bone mineral content (BMC) of each vertebral body was calculated by multiplying the bone tissue volume of the whole bone (trabecular bone, cortical shell, and endplates) by an assumed uniform tissue density of 1.90 g/cm^3 [105], the same tissue density being used for all specimens.

Finite Element Analysis

Parametric nonlinear finite element analysis was performed on each specimen to assess the yield strength of the vertebral body when loaded via an implant in axial compression, flexion-, and extension-induced impingement. The finite element approach was both geometrically and materially nonlinear, meaning it simulated both large-deformation failure mechanisms using finite strain theory and simulated yielding and plastic deformation of the bone tissue.

To reduce computational cost, the thresholded micro-CT data was coarsened from 37 μm to 74 μm before each voxel in the coarsened scan was converted into an eight-noded hexahedral finite element (Appendix 7.7). Elliptical TDA footplates (2.3 mm thick), also modeled using voxels, were placed on the inferior endplate of each vertebra such that the implant center coincided with the anterior-posterior (A/P) and medial-lateral (M/L) midpoint of the vertebral body. The footplates were assigned material properties similar to cobalt-chromium (elastic modulus 210 GPa, Poisson's ratio 0.33 [177]). A footplate size representing a likely clinical size was selected for each specimen, as described in detail in Chapter 3.

Nonlinear finite element analysis was used to compute the yield strength for each specimen (n = 12) loaded via an implant separately in axial compression, flexion-induced anterior impingement, and extension-induced posterior impingement, as well as for a control case loaded in compression on both ends via PMMA without an implant, totaling 48 simulations. In each simulation, a compressive displacement equivalent to 1% apparent-level strain (on a specimen-specific basis) was applied to the implant or the PMMA, depending on the model (Figure 4–1). To simulate uniform axial compression with an implant, the displacement boundary conditions were applied to a central circular region of the footplate, representing load transfer into the footplate through an insert. To simulate a scenario in which the footplate and the insert impinge following flexion or extension [14,86,91–96], the same 1% apparent-level compressive displacement was applied to a 2 mm thick, 90° arc of the footplate, representing load-transfer into the bone following impingement [166]. On the opposite side of the vertebral body, simulated layers of PMMA (elastic modulus 2.5 GPa, Poisson's ratio 0.30 [188]) were modeled to mimic the boundary conditions frequently used in *in vitro* biomechanical tests on whole-bone strength and implant subsidence [108,139,165,174].

All bone elements were assigned the same rate-independent elasto-plastic material model with homogenous isotropic tissue-level properties (elastic modulus 10.3 GPa; Poisson's ratio 0.30; tissue-level yield strains of 0.33% and -0.81% for tension and compression, respectively

[119,149]). Perfect bonding was assumed at all interfaces, thereby modeling full implant fixation in the bone.

On average, each analysis comprised approximately one hundred million degrees of freedom (range $5.8 \times 10^7 – 6.5 \times 10^8$ degrees of freedom, depending on the bone). Solving models of this size required a custom finite element code [134] including a parallel mesh partitioner and an algebraic multi-grid solver implemented on an 18-petaflop supercomputing cluster (Stampede2, Texas Advanced Computing Center, Austin, Texas). A typical analysis utilized 960 Intel Xeon Platinum 8160 processors (20 compute nodes) in parallel and four terabytes of memory. For the 48 analyses, the total single-processor-equivalent CPU time was approximately 16 years.

Outcomes

The primary outcomes were the computed yield strength of each vertebral body when loaded via an implant in each of the three loading modes, and when loaded in compression exclusively via PMMA. The yield strength was defined as the force at the intersection of the nonlinear force-deformation curve using a 0.2% offset line parallel to the curve's linear region (Figure 4–2) [135]. For each specimen, the reduction in yield strength was calculated for each implant load-case (compression, flexion, extension) relative to the same specimen loaded via PMMA in compression (i.e. the specimen-specific control). The mean reduction in yield strength was compared between the implant loading modes using a general linear regression model and the Tukey HSD post-hoc test.

A second outcome investigated the role of bone morphology on the yield strength and yield strength change relative to the specimen specific PMMA control. The independent roles of bone mineral content and each bone microarchitectural parameter were quantified using univariate linear regression, and combined effects were quantified using forward stepwise linear regression. For the latter, age plus all marginally statistically significant ($p < 0.10$) morphological parameters were sequentially added to the model to assess whether these combined measures could more fully explain the variations in yield strength compared to any explanatory variable independently. The final model only contained variables for which $p < 0.05$. To account for multi-collinearity, the significant explanatory variables with the highest cross-correlations were sequentially removed until the variance inflation factor for all variables was below five [189]. Statistical analyses were performed in JMP Pro (v. 15.0) and significance was reported for $p < 0.05$.

4.3 Results

Across all vertebrae, the yield strength of the specimens loaded exclusively via PMMA in compression (PMMA controls) varied over six-fold, consistent with wide variations in bone mineral content and microarchitecture of the specimens (yield strength range = 1.4–9.3 kN, Figure 4–3A, Table 4–1) [108].

For all bones, there was a reduction in yield strength when loaded via an implant compared to via PMMA (Figure 4–3A). The mean reduction in yield strength depended on the loading mode (Figure 4–3B): flexion and extension caused a greater mean reduction in yield

strength than axial compression ($p = 0.009$ and 0.045 for flexion and extension versus compression, respectively; Tukey HSD post hoc test; Figure 4–3B). The mean reduction in yield strength was not statistically different between flexion and extension loading ($p = 0.785$).

On average, the yield strength declined by 52 ± 14%, 66 ± 9%, and 63 ± 8% (mean ± SD) when loaded by an implant in compression, flexion-, and extension-induced impingement, respectively, relative to the PMMA controls.

Results from the univariate regression analysis show that total bone mineral content was highly associated with yield strength when the vertebrae were loaded via PMMA and via an implant ($r = 0.82$–0.93 across loading modes, $p \leq 0.001$; Table 4–2, Figure 4–4A). However, bone mineral content was not associated with the change in yield strength induced by implantation (i.e. relative to the PMMA controls, $p > 0.12$, Figure 4–4B). For an implant loaded in compression, trabecular bone volume fraction explained a substantial portion of the variation in yield strength reduction ($r = 0.87$, $p < 0.001$, Figure 4–4D).

When loaded via an implant, unlike when loaded via PMMA, the cortical mass fraction was associated with yield strength ($r = -0.58$ to -0.68, $p = 0.015$–0.046 across loading modes; Table 4–2; Figure 4–4E); in other words, when loaded via an implant, the greater the ratio of cortical bone mass to whole vertebral body mass, the lower the yield strength. Cortical mass fraction was the only parameter associated with the change in yield strength for all loading modes ($p = 0.0008$–0.036, Figure 4–4F).

After accounting for multi-collinearity, the explanatory variables included in the stepwise linear regression analysis comprised bone mineral content, age, mean trabecular thickness, mean ellipsoid factor, and cortical mass fraction. The results indicated that, when loaded via an implant, considering the combined measures of bone mineral content, trabecular thickness, and trabecular mass fraction could account for a substantial portion of the variation in yield strength ($R^2 = 0.87$–0.91 for BMC + Tb.Th + Ct.M across loading modes, $p < 0.02$ each, Figure 4–5A). In contrast, the change in yield strength was mostly associated with the cortical mass fraction alone; including other parameters in the regression model did not substantially improve the strength change predictions (Figure 4–5B).

4.4 Discussion

These results indicate that loading a vertebral body via a TDA implant causes a substantial reduction in whole-bone yield strength compared to loading the same vertebral body in compression via PMMA. The specimen-specific strength reduction was always > 30% and the mean reduction was approximately 50–65%, depending on the loading mode (flexion- and extension-induced impingement caused a greater reduction in yield strength than axial compression, though the difference was small relative to the overall strength reduction). The magnitude of the yield strength reduction also depended on the vertebral microstructure. Specifically, vertebrae with lower bone volume fractions, in addition to having lower overall yield strengths, also experienced a greater reduction in yield strength caused by implantation compared to those vertebrae with higher bone volume fractions. There was also a greater reduction in yield strength for vertebrae in which the cortical shell comprised a greater

percentage of the overall bone mass (a high cortical mass fraction) relative to those vertebrae in which the cortical shell comprised a lesser percentage of the overall bone mass. In conclusion, all vertebrae spanning the range of microstructural characteristics tested can expect a substantial reduction in yield strength when loaded via a TDA implant relative to when loaded via PMMA, but TDA disproportionally alters the yield strength for specimens with low trabecular bone volume fractions, whose bone mass is relatively dominated by the cortical shell.

This finding—that trabecular bone volume fraction and cortical mass fraction were associated with the reduction in yield strength following TDA—provides insight into the mechanisms of whole-bone failure. The reduction in yield strength increased as trabecular bone volume fraction decreased, indicating that whole-bone yield strength is much more sensitive to changes in the trabecular compartment when the bone is loaded via an implant compared to when the same bone is loaded via PMMA. Consistent with this, the reduction in yield strength was greater in those vertebrae for which the cortical bone mass represented a larger percentage of the overall bone mass, indicating that the cortical shell plays a diminished role in resisting bone failure when the vertebral body is loaded by a TDA implant. A reduced role of the cortical shell following TDA is expected since the TDA implant does not directly load the cortical shell, and a prior study [166] demonstrated that the cortical load fraction (axial force in the cortical bone relative to the overall reaction force) is diminished throughout the vertebral body following TDA. However, the current results also suggest that for implants of typical clinical size, this increased reliance on the trabecular compartment has a substantial effect on whole-bone yield strength, particularly for those patients with low trabecular bone volume fraction, whose cortical bone makes up a larger portion of their overall vertebral bone mass. Trabecular bone volume fraction and cortical mass fraction are separate microstructural measures but do not vary independently ($r = -0.82$ for the cross-correlation between BV/TV and Ct.M, $p = 0.001$); that is, a decrease in bone volume fraction implies an increase in cortical mass fraction. Thus, our results do not imply that increasing cortical bone mass alone (independently increasing Ct.M) would result in a decrease in yield strength with an implant; rather, the results indicate that yield strength is much more sensitive to changes within the trabecular compartment when the bone is loaded by an implant compared to when the same bone is loaded via PMMA. Therefore, small declines in trabecular bone volume fraction can have a magnified effect on whole-bone yield strength following TDA.

These findings both complement and extend prior studies. In a physical biomechanical experiment, Auerbach et al [139] measured the failure strength of $n = 56$ human lumbar vertebrae (mean age = 62 years) potted in PMMA and loaded to failure via TDA implants in compression: they found a significant association between failure strength and QCT-measured trabecular bone mineral density, consistent with the current results for trabecular bone volume fraction. Their mean failure force for the TDA-implanted vertebrae (2624 ± 1423 N, mean ± SD) agrees with the yield strength data for the comparable group (potted in PMMA and loaded to failure via an implant in compression) in the current study (2451 ± 1746 N): this agreement supports the current computational methodology and suggests that the limited sample size in the present study ($n = 12$) should reasonably represent typical human lumbar vertebrae over the range of vertebral morphologies tested. Yoder et al [165] also reported the vertebral failure force for elderly human lumbar vertebrae (mean age of 79 years) potted in PMMA and loaded to failure via TDA implants in compression: their results demonstrate a six-fold variation in

strength that was significantly predicted by the QCT-measured trabecular bone density, consistent with the findings here. However, the mean failure force found in that study (approximately* 1260 ± 570 N, mean ± SD) is lower than that found here—this may relate to the fact that all patients in their cohort were older than 69 years of age. The results found here extend these prior studies by demonstrating that trabecular bone volume fraction (which is proportional to QCT-measured trabecular bone mineral density) predicts not just the strength of the vertebral body when loaded via a TDA implant, but also the change in strength caused by the implant. Further, TDA reduces the strength of vertebrae with lower trabecular bone volume fractions—which already exhibit lower bone strengths—to a much greater extent than other specimens.

Enabling these findings, one strength of this study is its ability to conduct repeated yield strength measurements on the same sample: this approach is only possible with computational models due to the destructive nature of physical strength testing. The computational approach used here—including accurately modeling the complete morphometric details of the vertebral body from micro-CT image data while accounting for geometric and material nonlinearities in the mechanical response of the bone tissue—is the first of its kind in the study of TDA-implanted vertebrae. Together, the repeated-measures design and the highly specialized modeling approach enabled calculation of the specimen-specific change in strength caused by implantation, as opposed to just the difference in strength between two experimental groups—this provides key mechanistic data regarding which features of the bone are related to a strength change, which could help identify features pre-disposing a patient to subsidence.

Despite these positive aspects of the study, there are also several limitations. First, the vertebral bodies were virtually potted in PMMA instead of loaded via intervertebral discs; therefore, the data reported here better represents *in vitro* biomechanical tests rather than *in vivo* conditions. The strength of the vertebral body could be different when loaded via an intervertebral disc than when potted in PMMA, particularly if potting suppresses the high levels of tensile strain that can develop in the osseous endplate when loaded via an intervertebral disc in compression [130]. While modeling an intervertebral disc instead of PMMA would have been more realistic in terms of simulating *in vivo* behavior, the current experimental design was required due to the disc's high level of compliance relative to PMMA, requiring large displacements prior to bone failure. When accounting for geometric and material nonlinearities in models of this size (up to 66 million mesh nodes), these large displacements inhibit numerical convergence, causing prohibitive computational expense. However, a sensitivity study (Appendix 7.8) conducted on a single model indicated that the strength predictions for a disc-bone-implant model compared to a PMMA-bone-implant model differed by 10% (higher strength predictions when loaded via PMMA, consistent with tensile strain suppression). Since the effect of the implant on strength was substantially larger (33–82%), it's unlikely that the overall conclusions would change had an intervertebral disc been modeled as opposed to potting the vertebrae in PMMA.

This study is also limited in that the analysis was entirely computational and did not include any physical biomechanical testing to validate the strength predictions. Physical testing was not possible since these vertebrae were destructively tested in unrelated experiments.

* Estimated using ImageJ based on Figure 3A in [165].

However, there is substantial existing data supporting the validity of the yield strength predictions shown here (Appendix 7.9). For example, using the same finite element approach employed here—including hexahedral finite elements converted from thresholded micro-CT data (< 80 μm isotropic resolution), homogenous isotropic elastic tissue material assumptions, an elasto-plastic constitutive model, the inclusion of geometric along with material nonlinearities, tissue-level tension-compression strength asymmetry, and solved using the same parallel finite element solver—Fields et al [154] accurately predicted the experimentally-measured strength of n = 12 elderly thoracic human vertebrae loaded to failure in compression via PMMA ($R^2 = 0.85$ with Y = X type behavior). Separately, this same finite element approach accurately predicted the experimentally measured strength of n = 54 human trabecular bone cores from across anatomic sites loaded in compression ($R^2 = 0.98$) and tension ($R^2 = 0.99$) [119], as well as the strength of n = 12 proximal human femurs from elderly cadavers ($R^2 = 0.94$ with Y = X type behavior [178]). In combination, these data indicate a high-level of accuracy in bone strength predictions for this finite element approach under the unique set of assumptions used; indeed, the accuracy of this method across anatomic sites and variations in bone morphometry indicate that the dominant structural mechanisms in the bone itself are well-captured.

In modeling the bone tissue, homogenized effective trabecular tissue properties were used (elastic modulus 10.3 GPa, Poisson's ratio 0.3); these elastic constants were chosen because they were calibrated using human vertebral trabecular bone cores and a combination of micro-CT-based finite modeling and physical experiments [149]. While this approach neglects real variations in tissue mineralization, there is low inter- and intra-specimen variation in tissue mineral density amongst adult humans without metabolic bone disease [190], and variations in tissue mineral density in turn have only a modest effect (< 10%) on the apparent-level elastic properties [191]. Overall, there is extensive experimental data supporting the accuracy of yield strength predictions based on the finite element approach and modeling assumptions used here.

Despite these limitations, the current results may have clinical implications. The finding that the specimen-specific reduction in yield strength was associated with the trabecular bone volume fraction, and that small decreases in trabecular bone volume fraction can have a disproportionately large negative effect on yield strength, suggests that pre-operative assessment of bone quality should focus specifically on the trabecular centrum. DXA, the current standard for pre-operative assessment of bone mineral density prior to TDA [25], uses projectional measurements of entire vertebrae to calculate bone density, summating the cortical-rich posterior elements and osseous endplates with the trabecular centrum [169]. Particularly in presence of degenerative changes such as osteophytes, this two dimensional approach is a recognized limitation to the DXA technique [169,180,192]. The current results suggest that the problem could be magnified when load is applied via a TDA implant because when the cortical bone mass accounts for a large portion of the overall bone mass (high Ct.M), the reduction in yield strength caused by the implant is disproportionately large. It's hypothetically possible that a patient with DXA-measured bone mineral density above the osteoporotic or osteopenic range (T-score > -2.5 or -1 SD, respectively), whose density assay was skewed by large amounts of cortical bone, could have a much lower whole-bone yield strength following TDA than the DXA assay would suggest, possibly placing that patient at a much higher risk of implant subsidence. Supporting this hypothesis, Hasegawa et al [174] found that when n = 20 human lumbar vertebral bodies were loaded via a titanium elliptical interbody implant for spinal fusion (25 mm diameter), the

QCT-measured bone mineral density focused specifically on the trabecular region produced a much stronger and more statistically significant association with vertebral strength compared to DXA-measured bone mineral density. Therefore, QCT might be uniquely beneficial in the pre-operative assessment of bone quality prior to TDA surgery, since these measurements should be less sensitive to a cortex-driven overestimation of the biomechanically relevant bone mineral density. Newer tests such as a biomechanical computed tomography (BCT) strength test [180] might also offer improvements over DXA in the pre-operative assessment of bone quality prior to TDA—this topic is a promising direction for future research.

Finally, the results indicate that the reduction in yield strength is greater for an implant loaded in flexion- or extension- induced impingement than in axial compression, suggesting that impingement could increase the risk of subsidence. A recent study [11] found that subsidence frequently involves not just axially-compressive displacement (i.e. parallel subsidence) but also progressive rotational penetration of the TDA footplate into the underlying vertebral body [8,11,193], consistent with a bending-type loading mode. While bending-induced impingement is not the habitual loading case, radiographic and explant data demonstrate that impingement occurs in sagittal bending for both unconstrained and semi-constrained devices [14,86,91–96]. Analysis of retrieved implants and *in vitro* experiments suggest that large loads can be transmitted through the impinged regions during bending [14,86,94], providing support for the bending-induced impingement boundary conditions used here. Future research should be directed at whether implants could be designed to reduce the frequency or strength-reduction effects of impingement loading. Pre-clinical testing of TDA implants might also include some form of evaluation of bending-induced impingement if such loading is possible *in vivo*. As has been recommended for *in vitro* wear testing [86,94,96], *in vitro* subsidence testing for TDA implants should also include an impingement load case if the implant enables that type of loading *in vivo*.

Table 4–1. Patient demographic data, bone morphologic and microarchitectural parameters, and computed yield strength results.

	Mean	SD	Range
Demographic data			
Age (years)	71	14	51–89
Sex	N = 4 female, 8 male		
Total BMC (g)	12.7	4.8	5.6–21.5
Microarchitecture			
BV/TV	0.105	0.025	0.060–0.145
Tb.Th (mm)	0.17	0.04	0.14–0.27
Tb.Sp (mm)	1.14	0.47	0.89–2.59
Tb.EF	0.044	0.042	-0.03–0.135
Conn.D (mm^3)	3.94	1.87	1.01–6.62
Ct.Th (mm)	0.42	0.16	0.27–0.81
Ct.M	0.326	0.051	0.232–0.391
Failure force (N)			
PMMA comp.	4800	2700	1440–9290
Implant comp.	2450	1750	440–6200
Implant flexion	1590	920	420–3250
Implant extension	1790	1090	430–4020

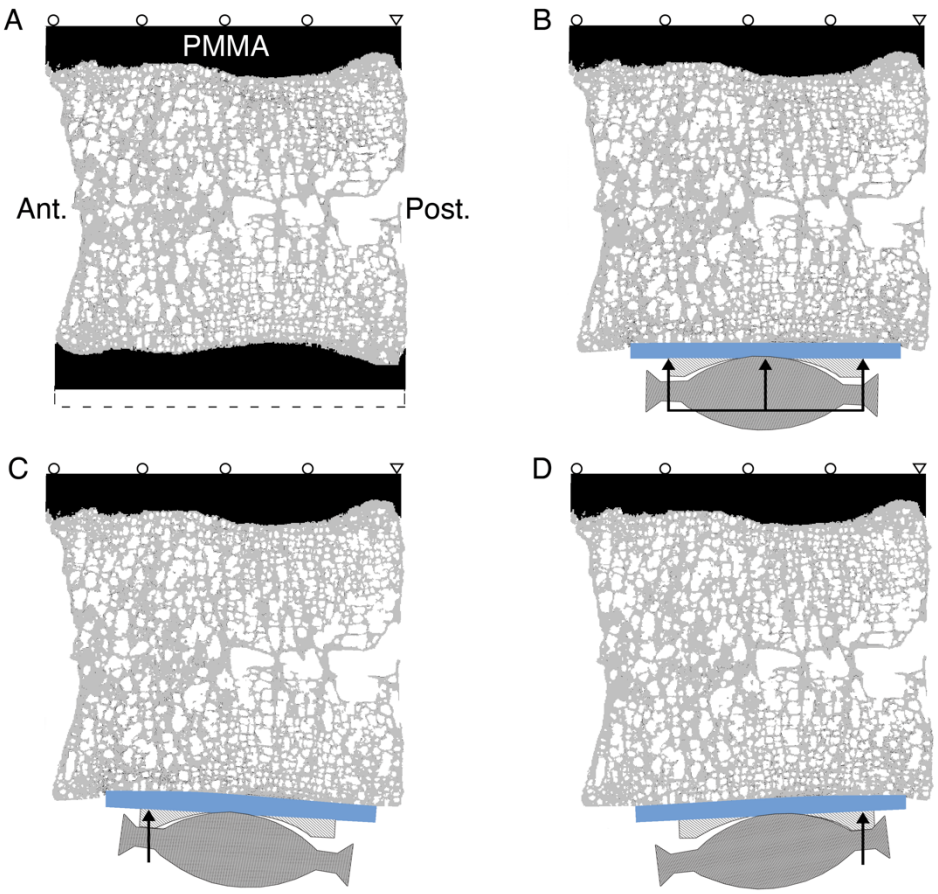

Figure 4–1. Mid-sagittal cross-section (0.5 mm thick) showing boundary conditions and magnified displaced shapes for the (A) PMMA model loaded in compression (B) TDA model loaded in compression (C) TDA model loaded in flexion-induced impingement and (D) TDA model loaded in extension-induced impingement. The implant components depicted above the footplate (blue) were not explicitly modeled but are illustrated to motivate the bending-induced impingement boundary conditions.

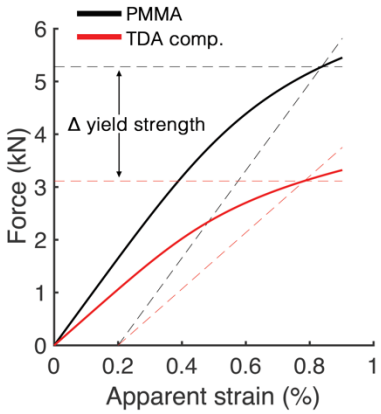

Figure 4–2. Representative force-apparent strain curve for one vertebra (BV/TV = 0.134) loaded via PMMA and via a TDA implant in compression. A 0.2% offset method was used to calculate yield strength.

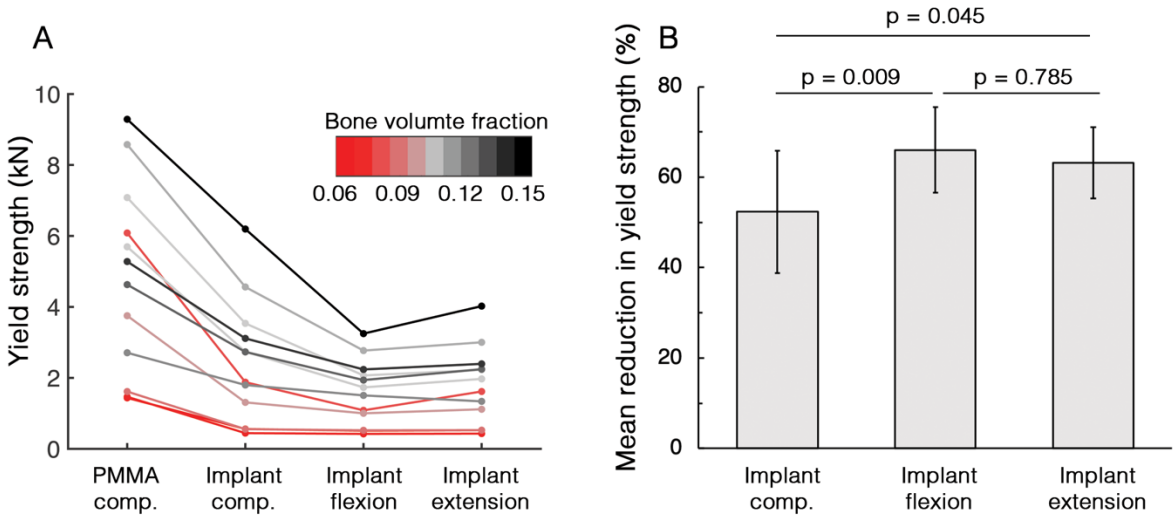

Figure 4–3. (A) Yield strength for all specimens as a function of loading mode. (B) Mean (SD) reduction in yield strength for the models loaded via a TDA implant in compression, flexion-, and extension-induced impingement relative to the same models loaded in compression via PMMA.

Table 4–2. The Pearson correlation coefficient (r) quantifying the independent association between the computed yield strength and reduction in yield strength with age, bone mineral content, and each bone microstructural parameter. The strength reduction was calculated as the relative strength change in relation to the same vertebra loaded in compression via PMMA without an implant. Bold typeface indicates $p < 0.05$.

	Load mode	BV/TV	BMC	Age	Tb.Th	Tb.Sp	Conn.D	Tb.EF	Ct.Th	Ct.M
Strength	PMMA comp.	**0.65**	**0.93**	-0.12	**0.62**	0.41	-0.27	**-0.67**	0.38	-0.44
	Implant comp.	**0.80**	**0.87**	-0.27	**0.58**	0.32	-0.22	**-0.74**	0.24	**-0.58**
	Implant flexion	**0.87**	**0.82**	-0.35	**0.58**	0.32	-0.14	**-0.75**	0.23	**-0.68**
	Implant extension	**0.84**	**0.86**	-0.23	**0.57**	0.29	-0.19	**-0.74**	0.23	**-0.61**
Strength reduction	Implant comp.	**0.87**	0.47	-0.55	0.28	0.02	0.08	**-0.59**	-0.10	**-0.83**
	Implant flexion	0.48	-0.19	-0.56	-0.08	-0.17	0.29	-0.20	-0.35	**-0.61**
	Implant extension	**0.70**	0.04	-0.43	0.04	-0.18	0.19	-0.34	-0.33	**-0.70**

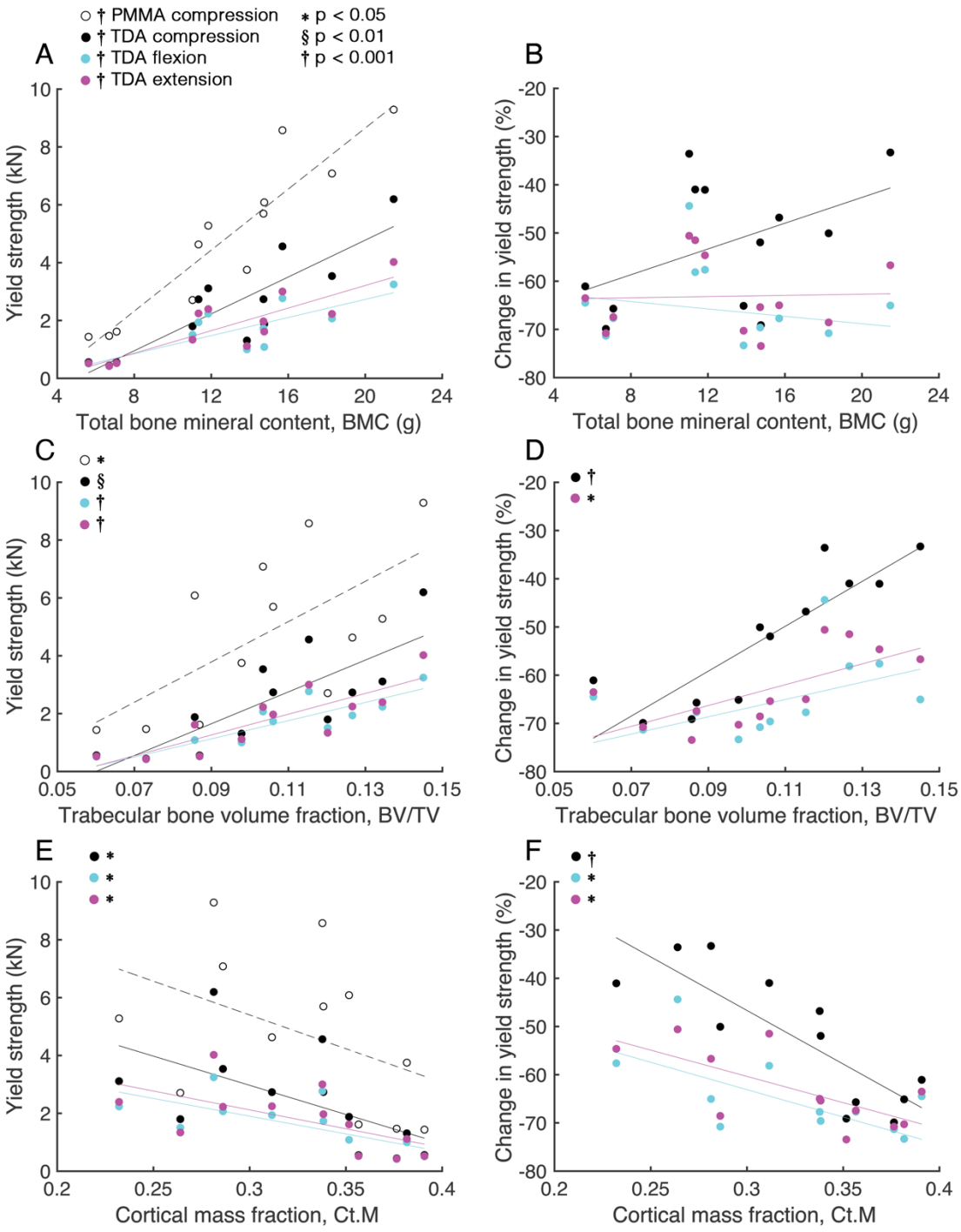

Figure 4–4. Left panel: Yield strength as a function of bone microarchitectural parameters and loading mode. Right panel: The change in yield strength for the implanted models relative to the same vertebra loaded in compression via PMMA without an implant as a function of bone microarchitectural parameters and loading mode.

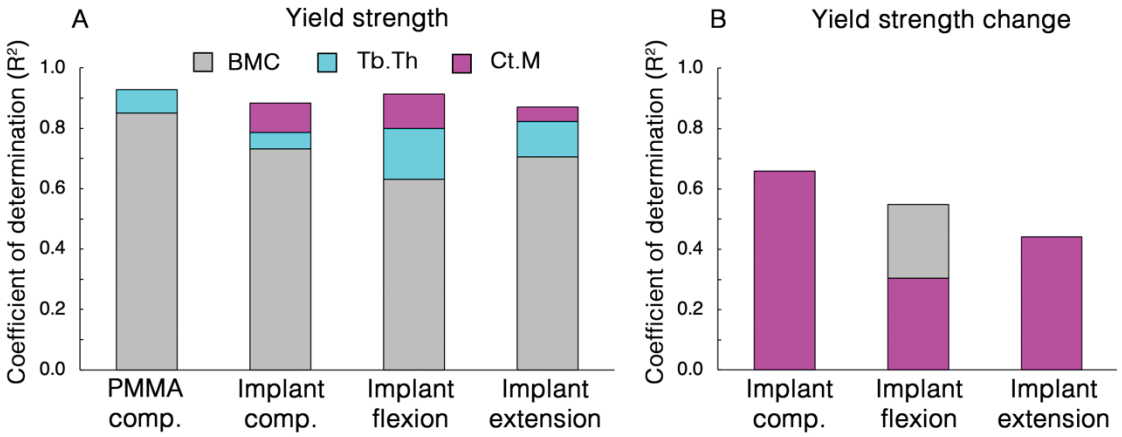

Figure 4–5. (A) When loaded via an implant, accounting for the combined effects of BMC, Tb.Th, and Ct.M improved the yield strength predictions compared to any independent explanatory parameter. (B) The strength change caused by implantation (i.e. relative to loading with PMMA without an implant) was significantly associated with Ct.M ($p \leq 0.01$ for each loading mode).

5. Conclusions

The overall goal of this research was to provide insight into the bone biomechanics of TDA-implanted vertebrae. The research investigated fundamental mechanisms by which lumbar TDA implants altered the yield strength of the vertebral body, stress in the bone tissue, and trabecular-cortical load-sharing behavior. The findings could have broad clinical and scientific implications related to pre-operative assessment of bone quality, *in vitro* test protocols for device development and regulation, the development of new implant designs, and clinical exclusion criteria. Ultimately, the hope is that this insight can be used to improve clinical outcomes for this class of device, and, in turn, contribute to the broad effort of addressing the global health burden associated with degenerative spinal pathologies.

The main conclusions and recommendations supported by this body of work are:

1. *TDA alters the way in which load is shared between cortical and trabecular compartments (Chapter 2)*

The presence of a TDA implant can substantially alter the cortical-trabecular load-sharing behavior relative to the expected physiologic load-sharing behavior. Implant size has a larger effect on the alteration in load-sharing behavior than implant material for a constant applied force. The differences in load-transfer behavior between the intact model and the implant models is much larger for bending-induced impingement than for compression. In other words, bending to the point of impingement with an implant causes much larger deviations from the natural biomechanical environment compared to compression with an implant. Specifically, sagittal bending with an implant causes local increases in stress anteriorly or posteriorly and shifts the tissue at the highest risk of failure to local regions adjacent to the impingement. This behavior is accentuated as implant size increased but does not depend much on implant material properties. Implants of typical clinical size and material underload the cortical shell in both compression and bending-induced impingement both adjacent to the implant and much deeper in the vertebral body.

2. *The whole-bone yield strength of the vertebral body is reduced when loaded by a TDA implant; the magnitude of the strength reduction depends on the vertebral microstructure (Chapters 3–4)*

Vertebrae with lower trabecular bone volume fractions, in addition to having lower overall yield strengths, also experience a greater reduction in yield strength caused by implantation compared to those vertebrae with higher bone volume fractions. The trabecular bone volume fraction and cortical mass fraction are associated with the reduction in yield strength caused by a TDA implant relative to loading the vertebral body via PMMA. Whole-bone yield strength is much more sensitive to changes within the trabecular compartment when the bone is loaded by an implant compared to when the same bone is loaded via PMMA; therefore, small declines in trabecular bone volume fraction can have a magnified effect on whole-bone yield strength post implantation. To identify those patients in whom implantation might cause disproportionate reduction in whole-bone yield strength (possibly pre-disposing those patients to implant subsidence) pre-operative assessment of bone quality should optimally

focus on the trabecular centrum. The apparent bone mineral density in the trabecular centrum may be a better measure of biomechanically relevant apparent bone mineral density compared with whole-bone measurements.

3. Impingement induced by sagittal bending (flexion or extension) increases bone stress in local regions of the vertebral body and is associated with a reduction in bone strength (Chapters 2–4)

When a TDA footplate is loaded through its anterior or posterior rim, representing load-transfer into the bone following impingement induced by flexion or extension, bone stress near the impinged region increases substantially. While the yield strength of the vertebral body is reduced when loaded via a TDA implant compared to when loaded via PMMA, this reduction is larger for flexion- and extension-induced impingement loading than for axial compression, suggesting that subsidence might be caused, in some cases, by impingement-type loading. Pre-clinical subsidence testing of TDA implants should therefore include some form of evaluation of bending-induced impingement if the implant enables this type of loading *in vivo*. This mechanistic etiologic link between implant impingement and subsidence may help explain why subsidence often involves not just axially compressive displacement (i.e. parallel subsidence) but also progressive rotational penetration of the TDA footplate into the underlying vertebral body.

The primary strength of this body of work is its application of high-resolution micro-CT imaging coupled with parallel finite element analysis and high-performance scientific computing to study of TDA-implanted vertebrae. Based on a one-to-one mapping of micro-CT voxels to finite elements, this modeling approach intrinsically incorporates the contributions of the complete morphometry of the calcified bone tissue, including the structural anisotropy and connectivity of the trabecular microstructure. For this reason, micro-CT based finite element analysis has had substantial impact on the bone biomechanics field but has not previously been applied to the study of TDA-implanted vertebrae; in this regard, the research presented here is the first study of its kind. The advantages of micro-CT based finite element analysis were leveraged by conducting controlled parameter experiments using repeated measurements of the same samples to isolate key variables such as implant size, material, and loading mode. For example, the repeated-measures experimental design enabled the calculation of a specimen-specific change in yield strength caused by implantation as opposed to a difference in strength between two experimental groups (Chapter 4). This approach is only possible with computational models due to the destructive nature of many physical biomechanical tests. The models solved here (over 1 billion degrees of freedom in some cases) are among the largest finite element problems reported in the biomechanics field: the incorporation of geometric and material nonlinearities in models of this size and structural complexity represents a significant methodological strength in this body of work.

One limitation to this work is its limited sample size (n = 12), and the fact that all experiments were based on the same cohort of vertebrae. However, the morphological and microarchitectural features of these vertebrae are consistent with studies using much larger sample sizes, and many of the reported outcomes (such as the trabecular-cortical load-sharing behavior and the computed yield strength values) are consistent with other studies on whole-bone biomechanics, suggesting that the limited sample size should reasonably represent typical

human lumbar vertebrae over the range of age and vertebral morphologies of the cohort (see Chapters 2–4 Discussion and Appendix 7.9)

This collective work is also limited in that the analysis was entirely computational and did not include any physical biomechanical testing to validate the experimental outcomes. Some outcomes, such as the maximum level of stress in the trabecular bone tissue (Chapters 2–3), are not possible to verify experimentally due to the technical challenges of measuring tissue-level stresses or strains within the bone tissue of the vertebral body. However, there is extensive experimental data supporting the accuracy of yield strength predictions based on the specialized finite element approach and unique modeling assumptions used; indeed, the accuracy of this method across anatomic sites and variations in bone morphometry indicates that the dominant structural mechanisms in the bone itself are well-captured (see Chapters 2–4 Discussion and Appendix 7.9). Further, many of the outcomes and conclusions are based on relative changes between repeated measurements from the same sample. As such, those results are less sensitive to uncertainties in model assumptions such as the elastic modulus of the bone tissue. A series of sensitivity studies included in the appendix (Appendix 7.1–7.4, 7.6–7.8) demonstrate the low sensitivity of the reported results to key modeling assumptions.

The findings from this dissertation identify promising directions for future research. Specifically, the enhanced sensitivity of vertebral yield strength to localized changes within the trabecular bone indicates that pre-operative assessment of bone quality should focus on the trabecular region: this finding illustrates the need for studies comparing the accuracy of strength predictions for vertebrae loaded by TDA implants across the available clinical modalities of assessing bone quality, such as DXA, QCT, or BCT. Additionally, whole-bone yield strength declined more when the implant was loading in flexion- or extension-induced impingement than in axial compression, indicating that subsidence could be related to impingement-type loading. Future research is therefore needed to better understand the prevalence and sequalae of impingement on the bone, and whether implants could be designed to reduce the frequency or strength-reduction effects of impingement loading. Finally, future research is required to assess how the bone tissue remodels in response to loading via an implant. The results found here suggest substantial stress re-distribution following TDA, which could alter remodeling behavior. Heterotopic ossification (pathological bone overgrowth) is frequently documented following TDA and might relate to this stress re-distribution; however, the ways in which the bone tissue remodels to accommodate loading via a TDA implant are unknown.

In closing, this dissertation elucidates fundamental mechanisms by which the vertebral bone tissue resists the loads applied by lumbar TDA implants. Overall, the results indicate that the load-transfer behavior in the underlying bone is substantially altered by TDA, causing high levels of trabecular bone stress, diminishing the role of the cortical shell, and substantially reducing the whole-bone yield strength. These findings were assessed in relationship to the vertebral bone morphology and microstructure, enabling mechanistic insight into bone sub-failure and failure behavior. In turn, this mechanistic insight was used to identify possible targets—including pre-clinical tests and implant design considerations—that might help to improve clinical outcomes for this class of device.

6. Works Cited

[1] Ravindra V, Senglaub S, Rattani A, et al. Degenerative Lumbar Spine Disease: Estimating Global Incidence and Worldwide Volume. *Glob Spine J*. 2018;8(8):784–94.

[2] Wu A, March L, Zheng X, et al. Global Low Back Pain Prevalence and Years Lived with Disability from 1990 to 2017: Estimates from the Global Burden of Disease Study 2017. *Ann Transl Med*. 2020;8(6):1–14.

[3] Rajaee S, Bae H, Kanim L, et al. Spinal Fusion in the United States: Analysis of Trends from 1998 to 2008. *Spine (Phila Pa 1976)*. 2012;37(1):67–76.

[4] World Health Organization (WHO). Ageing and Health [Internet]. 2020. Available from: https://www.who.int/news-room/fact-sheets/detail/ageing-and-health

[5] Ibrahim T, Tleyjeh I, Gabbar O. Surgical Versus Non-Surgical Treatment of Chronic Low Back Pain: A Meta-Analysis of Randomised Trials. *Int Orthop*. 2008;32(1):107–113.

[6] Sandhu F, Dowlati E, Garcia R. Lumbar Arthroplasty: Past, Present, and Future. *Neurosurgery*. 2020;86(2):155–169.

[7] Link H, Keller A. Biomechanics of Total Disc Replacement. In: Büttner-Janz K, Hochschuler S, McAfee P, editors. The Artificial Disc. Berlin, Germany: Springer; 2003. p. 33–52.

[8] Punt I, van Rijsbergen M, van Rietbergen B, et al. Subsidence of SB Charité Total Disc Replacement and the Role of Undersizing. *Eur Spine J*. 2013;22:2264–70.

[9] Punt I, Visser V, Van Rhijn L, et al. Complications and Reoperations of the SB Charité Lumbar Disc Prosthesis: Experience in 75 patients. *Eur Spine J*. 2008;17:36–43.

[10] Lu S, Sun S, Kong C, et al. Long-Term Clinical Results Rollowing Charité III Lumbar Total Disc Replacement. *Spine J*. 2018;18(6):917–25.

[11] Kitzen J, Verbiest V, Buil I, et al. Subsidence After Total Lumbar Disc Replacement is Predictable and Related to Clinical Outcome. *Eur Spine J*. 2020;29(7):1544–52.

[12] Aunoble S, Donkersloot P, Le Huec J. Dislocations with Intervertebral Disc Prosthesis: Two Case Reports. *Eur Spine J*. 2004;13(5):464–7.

[13] Mathew P, Blackman M, Redla S, et al. Bilateral Pedicle Fractures Following Anterior Dislocation of the Polyethylene Inlay of a ProDisc Artificial Disc Replacement: A Case Report of an Unusual Complication. *Spine (Phila Pa 1976)*. 2005;30(11):E311–4.

[14] Kurtz S, van Ooij A, Ross R, et al. Polyethylene Wear and Rim Fracture in Total Disc Arthroplasty. *Spine J*. 2007;7:12–21.

[15] Jin Y, Park S, Kim M, et al. An Analysis of Heterotopic Ossification in Cervical Disc Arthroplasty: A Novel Morphologic Classification of an Ossified Mass. *Spine J*. 2013;13(4):408–20.

[16] Putzier M, Funk J, Schneider S, et al. Charité Total Disc replacement: Clinical and Radiographical Results After an Average Follow-Up of 17 Years. *Eur Spine J*. 2006;15:183–95.

[17] Park S, Kang K, Shin S, et al. Heterotopic Ossification Following Lumbar Total Disc Replacement. *Int Orthop*. 2011;35(8):1197–201.

[18] McAfee P, Cunningham B, Devine J, et al. Classification of Heterotopic Ossification (HO) in Artificial Disk Replacement. *J Spinal Disord Tech*. 2003;16(4):384–9.

[19] Tortolani P, Cunningham B, Mcafee P, et al. Prevalence of Heterotopic Ossification Following Total Disc Replacement. *J Bone Jt Surg*. 2007;89-A(1):82–8.

[20] Shim C, Lee S, Maeng D, et al. Vertical Split Fracture of the Vertebral Body Following Total Disc Replacement using ProDisc. *J Spinal Disord Tech*. 2005;18(5):465–9.

[21] Datta J, Janssen M, Beckham R, et al. Sagittal Split Fractures in Multilevel Cervical Arthroplasty Using a Keeled Prosthesis. *J Spinal Disord Tech*. 2007;20(1):89–92.

[22] Tu T, Wu J, Fay L, et al. Vertebral Body Split Fracture After a Single-Level Cervical Total Disc Replacement. *J Neurosurg Spine*. 2012;16:231–5.

[23] van Den Eerenbeemt K, Ostelo R, van Royen B, et al. Total Disc Replacement Surgery for Symptomatic Degenerative Lumbar Disc Disease: A Systematic Review of the Literature. *Eur Spine J*. 2010;19(8):1262–80.

[24] Tropiano P, Huang R, Girardi F, et al. Lumbar Disc Replacement: Preliminary Results with ProDisc II After a Minimum Follow-Up Period of 1 Year. *J Spinal Disord Tech*. 2003;16(4):362–8.

[25] Büttner-Janz K, Guyer R, Ohnmeiss D. Indications for Lumbar Total Disc Replacement. *Int J Spine Surg*. 2014;8(12):1–7.

[26] Huang R, Lim M, Girardi F, et al. The Prevalence of Contraindications to Total Disc Replacement in a Cohort of Lumbar Surgical Patients. *Spine (Phila Pa 1976)*. 2004;29(22):2538–41.

[27] Wong D, Annesser B, Birney T, et al. Incidence of Contraindications to Total Disc Arthroplasty: A Retrospective Review of 100 Consecutive Fusion Patients with a Specific Analysis of Facet Arthrosis. *Spine J*. 2007;7(1):5–11.

[28] Chin K. Epidemiology of Indications and Contraindications to Total Disc Replacement in an Academic Practice. *Spine J*. 2007;7(4):392–8.

[29] Jacobs W, van der Gaag N, Kruyt M, et al. Total Disc Replacement for Chronic Low-Back Pain. *Spine (Phila Pa 1976)*. 2012;38(1):24–36.

[30] Jacobs W, van der Gaag N, Tuschel A, et al. Total Disc Replacement for Chronic Back Pain in the Presence of Disc Degeneration. *Cochrane Database Syst Rev*. 2012;9:1–61.

[31] Zigler J, Gornet M, Ferko N, et al. Comparison of Lumbar Total Disc Replacement With Surgical Spinal Fusion for the Treatment of Single-Level Degenerative Disc Disease: A Meta-Analysis of 5-Year Outcomes From Randomized Controlled Trials. *Glob Spine J*. 2018;8(4):413–23.

[32] Hicks G, Morone N, Weiner D. Degenerative Lumbar Disc and Facet Disease in Older Adults: Prevalence and Clinical Correlates. *Spine (Phila Pa 1976)*. 2009;34(12):1301–6.

[33] Bartel D, Davy D, Keaveny T. Tissue Mechanics II: Soft Tissue. In: Orthopedic Biomechanics: Mechanics and Design in Musculoskeletal Systems. Upper Saddle River, NJ: Pearson Prentice Hall Bioengineering; 2006. p. 121–167.

[34] Adams M, Roughley P. What is Intervertebral Disc Degeneration, and What Causes It? *Spine (Phila Pa 1976)*. 2006;31(18):2151–61.

[35] Adams M, Lama P, Zehra U, et al. Why Do Some Intervertebral Discs Degenerate, When Others (In the Same Spine) Do Not? *Clin Anat*. 2015;28(2):195–204.

[36] Videman T, Battie M, Parent E, et al. Progression and Determinants of Quantitative Magnetic Resonance Imaging Measures of Lumbar Disc Degeneration: A Five-Year Follow-up of Adult Male Monozygotic Twins. *Spine (Phila Pa 1976)*. 2008;33(13):1484–90.

[37] Feng C, Liu H, Yang M, et al. Disc Cell Senescence in Intervertebral Disc Degeneration: Causes and Molecular Pathways. *Cell Cycle*. 2016;15(13):1674–84.

[38] Adams M, Freeman B, Morrison H, et al. Mechanical Initiation of Intervertebral Disc Degeneration. *Spine (Phila Pa 1976)*. 2000;25(13):1625–36.

[39] Antoniou J, Steffen T, Nelson F, et al. The Human Lumbar Intervertebral Disc: Evidence for Changes in the Biosynthesis and Denaturation of the Extracellular Matrix with Growth, Maturation, Ageing, and Degeneration. *J Clin Invest*. 1996;98(4):996–1003.

[40] Nerlich A, Schleicher E, Boos N. Immunohistologic Markers for Age-Related Changes of Human Lumbar Intervertebral Discs. *Spine (Phila Pa 1976)*. 1997;22(24):2781–2795.

[41] Videman T, Battié M, Gill K, et al. Magnetic Resonance Imaging Findings and Their

Relationships in the Thoracic and Lumbar Spine: Insights Into the Etiopathogenesis of Spinal Degeneration. *Spine (Phila Pa 1976)*. 1995;20(8):928–935.

[42] Battié M, Videman T, Parent E. Lumbar Disc Degeneration: Epidemiology and Genetic Influences. *Spine (Phila Pa 1976)*. 2004;29(23):2679–90.

[43] Videman T, Battie M, Gibbons L, et al. Associations Between Back Pain History and Lumbar MRI Findings. *Spine (Phila Pa 1976)*. 2003;28(6):582–8.

[44] Jacobs W, Tulder M, Arts M, et al. Surgery Versus Conservative Management of Sciatica Due to a Lumbar Herniated Disc: A Systematic Review. *Eur Spine J*. 2011;20(4):513–22.

[45] Cheng B, Welch W. Biomechanics of Nonfusion Devices: Novel Testing Techniques, Standards, and Implications for Future Devices. In: Yue J, Bertagnoli R, McAfee P, An H, editors. Motion Preservation Surgery of the Spine. Philadelphia, PA: Saunders; 2008. p. 45–51.

[46] Eck J, Sharan A, Ghogawala Z, et al. Guideline Update for the Performance of Fusion Procedures for Degenerative Disease of the Lumbar Spine. Part 7: Lumbar Fusion for Intractable Low-Back Pain Without Stenosis or Spondylolisthesis. *J Neurosurg Spine*. 2014;21(1):42–7.

[47] White A, Panjabi M. Biomechanical Considerations in the Surgical Management of the Spine. In: Clinical Biomechanics of the Spine. 2nd ed. Philadelphia, PA: J.B. Lippincott Company; 1990. p. 511–634.

[48] Mussano F, Ciccone G, Ceccarelli M, et al. Bone Morphogenetic Proteins and Bone Defects: A Systematic Review. *Spine (Phila Pa 1976)*. 2007;32(7):824–30.

[49] Rihn J, Kirkpatrick K, Albert T. Graft Options in Posterolateral and Posterior Interbody Lumbar Fusion. *Spine (Phila Pa 1976)*. 2010;35(17):1629–39.

[50] Highsmith J, Tumialán L, Rodts G. Flexible Rods and the Case for Dynamic Stabilization. *Neurosurg Focus*. 2007;22(1):1–5.

[51] Evans J. Biomechanics of Lumbar Fusion. *Clin Orthop Relat Res*. 1985;193:38–46.

[52] Mirza S, Deyo R. Systematic Review of Randomized Trials Comparing Lumbar Fusion Surgery to Nonoperative Care for Treatment of Chronic Back Pain. *Spine (Phila Pa 1976)*. 2007;32(7):816–23.

[53] Mannion A, Brox J, Fairbank J. Comparison of Spinal Fusion and Nonoperative Treatment in Patients with Chronic Low Back Pain: Long-Term Follow-Up of Three Randomized Controlled Trials. *Spine J*. 2013;13(11):1438–48.

[54] Yavin D, Clark C, Isaacs A, et al. Lumbar Fusion for Degenerative Disease: A Systematic

Review and Meta-Analysis. *Neurosurgery*. 2018;80(5):701–15.

[55] Moore K, Pinto M, Butler L. Degenerative Disc Disease Treated With Combined Anterior and Posterior Arthrodesis and Posterior Instrumentation. *Spine (Phila Pa 1976)*. 2002;27(15):1680–6.

[56] Greiner-Perth R, Boehm H, Allam Y, et al. Reoperation Rate After Instrumented Posterior Lumbar Interbody Fusion: A Report on 1680 Cases. *Spine (Phila Pa 1976)*. 2004;29(22):2516–20.

[57] Chow D, Luk K, Evans J, et al. Effects of Short Anterior Lumbar Interbody Fusion on Biomechanics of Neighboring Unfused Segments. *Spine (Phila Pa 1976)*. 1996;21(5):549–555.

[58] Axelsson P, Johnsson R, Strömqvist B. The Spondylolytic Vertebra and Its Adjacent Segment: Mobility Measured Before and After Posterolateral Fusion. *Spine (Phila Pa 1976)*. 1997;22(4):414–417.

[59] Cegoñino J, Calvo-Echenique A, Pérez-Del Palomar A. Influence of Different Fusion Techniques in Lumbar Spine Over the Adjacent Segments: A 3D Finite Element Study. *J Orthop Res*. 2015;33(7):993–1000.

[60] Weinhoffer S, Guyer R, Herbert M, et al. Intradiscal Pressure Measurements Above an Instrumented Fusion. *Spine (Phila Pa 1976)*. 1995;20(5):526–531.

[61] Levin D, Hale J, Bendo J. Adjacent Segment Degeneration Following Spinal Fusion for Degenerative Disc Disease. *Bull NYU Hosp Jt Dis*. 2007;65(1):29–36.

[62] Hilibrand A, Robbins M. Adjacent Segment Degeneration and Adjacent Segment Disease: The Consequences of Spinal Fusion? *Spine J*. 2004;4(Suppl. 6):190–4.

[63] Dekutoski M, Schendel M, Ogilvie J, et al. Comparison of In Vivo and In Vitro Adjacent Segment Motion After Lumbar Fusion. *Spine (Phila Pa 1976)*. 1994;19(15):1745–51.

[64] Park P, Garton H, Gala V, et al. Adjacent Segment Disease After Lumbar or Lumbosacral Fusion: Review of the Literature. *Spine (Phila Pa 1976)*. 2004;29(17):1938–44.

[65] McKenzie A. The Basis for Motion Preservation Surgery. In: Yue J, Bertagnoli R, An H, editors. Motion Preservation Surgery of the Spine. Philadelphia, PA: Saunders; 2008. p. 3–10.

[66] Mathews H, LeHuec J, Friesem T, et al. Design Rationale and Biomechanics of Maverick Total Disc Arthroplasty with Early Clinical Results. *Spine J*. 2004;4(Suppl. 6):S268–75.

[67] Huang R, Girardi F, Cammisa F, et al. The Implications of Constraint in Lumbar Total Disc Replacement. *J Spinal Disord Tech*. 2003;16(4):412–7.

[68] Galbusera F, Bellini C, Zweig T, et al. Design Concepts in Lumbar Total Disc Arthroplasty. *Eur Spine J*. 2008;17(12):1635–50.

[69] Abi-Hanna D, Kerferd J, Phan K, et al. Lumbar Disk Arthroplasty for Degenerative Disk Disease. *World Neurosurg*. 2018;109:188–96.

[70] Serhan H, Mhatre D, Defossez H, et al. Motion-Preserving Technologies for Degenerative Lumbar Spine. *Int Soc Adv Spine*. 2011;5(3):75–89.

[71] Rundell S, Auerbach J, Balderston R, et al. Total Disc Replacement Positioning Affects Facet Contact Forces and Vertebral Body Strains. *Spine (Phila Pa 1976)*. 2008;33(23):2510–7.

[72] Rousseau M, Bradford D, Bertagnoli R, et al. Disc Arthroplasty Design Influences Intervertebral Kinematics and Facet Forces. *Spine J*. 2006;6:258–66.

[73] Siemionow K, Hu X, Lieberman I. The Fernstrom Ball Revisited. *Eur Spine J*. 2012;21(3):443–8.

[74] Büttner-Janz K. History. In: Büttner-Janz K, Hochschuler S, McAfee P, editors. The Artificial Disc. Berlin, Germany: Springer; 2003. p. 1–10.

[75] Link H. Disc Arthroplasty and the Relationship Between Anerior and Posterior Vertebral Elements. In: Büttner-Janz K, Hochschuler S, McAfee P, editors. The Artificial Disc. Berlin, Germany: Springer; 2003. p. 53–61.

[76] Borkowski P, Marek P, Krzesiński G, et al. Finite Element Analysis of an Elastomeric Artificial Disc in Lumbar Spine. *Acta Bioeng Biomech*. 2012;14(1):59–66.

[77] Rischke B, Ross R, Jollenbeck B, et al. Preclinical and Clinical Experience with a Viscoelastic Total Disc Replacement. *SAS J*. 2011;5(4):97–107.

[78] Singh K, Vaccaro A, Albert T. Assessing the Potential Impact of Total Disc Arthroplasty on Surgeon Practice Patterns in North America. *Spine J*. 2004;4(Suppl. 6):S195–201.

[79] Hart R, DePasse J, Daniels A. Failure to Launch: What the Rejection of Lumbar Total Disk Replacement Tells us about American Spine Surgery. *Clin Spine Surg*. 2017;30(6):E759–64.

[80] Nie H, Chen G, Wang X, et al. Comparison of Total Disc Replacement with Lumbar Fusion: A Meta-Analysis of Randomized Controlled Trials. *J Coll Physicians Surg Pakistan*. 2015;25(1):60–7.

[81] Yajun W, Yue Z, Xiuxin H, et al. A Meta-Analysis of Artificial Total Disc Replacement Versus Fusion for Lumbar Degenerative Disc Disease. *Eur Spine J*. 2010;19(8):1250–61.

[82] Rao M, Cao S. Artificial Total Disc Replacement Versus Fusion for Lumbar Degenerative Disc Disease: A Meta-Analysis of Randomized Controlled Trials. *Arch Orthop Trauma Surg*. 2014;134(2):149–58.

[83] Wei J, Song Y, Sun L, et al. Comparison of Artificial Total Disc Replacement Versus Fusion for Lumbar Degenerative Disc Disease: A Meta-Analysis of Randomized Controlled Trials. *Int Orthop*. 2013;37(7):1315–25.

[84] Tropiano P, Huang R, Girardi F, et al. Lumbar Total Disc Replacement: Seven to Eleven-Year Follow-Up. *J Bone Jt Surg*. 2005;87A(3):490–6.

[85] Siepe C, Heider F, Wiechert K, et al. Mid- to Long-Term Results of Total Lumbar Disc Replacement. *Spine J*. 2014;14(8):1417–31.

[86] Kurtz S, Siskey R, Ciccarelli L, et al. Retrieval Analysis of Total Disc Replacements: Implications for Standardized Wear Testing. *J ASTM Int*. 2006;3(6):53–64.

[87] van Ooij A, Kurtz S, Stessels F, et al. Polyethylene Wear Debris and Long-Term Clinical Failure of the Charité Disc Prosthesis. *Spine (Phila Pa 1976)*. 2007;32(2):223–9.

[88] Lebl D, Cammisa F, Girardi F, et al. In Vivo Functional Performance of Failed Prodisc-L Devices. *Spine (Phila Pa 1976)*. 2012;37(19):E1209-17.

[89] Kurtz S, Patwardhan A, MacDonald D, et al. What is the Correlation of In Vivo Wear and Damage Patterns with In Vitro TDR Motion Response? *Spine (Phila Pa 1976)*. 2008;33(5):481–9.

[90] Baxter R, MacDonald D, Kurtz S, et al. Severe Impingement of Lumbar Disc Replacements Increases the Functional Biological Activity of Polyethylene Wear Debris. *J Bone Jt Surg*. 2013;75(95):e75(1-9).

[91] Austen S, Punt I, Cleutjens J, et al. Clinical, Radiological, Histological and Retrieval Findings of Activ-L and Mobidisc Total Disc Replacements: A Study of Two Patients. *Eur Spine J*. 2012;21(Suppl 4):S513–20.

[92] Käfer W, Clessienne C, Däxle M, et al. Posterior Component Impingement After Lumbar Total Disc Replacement. *Spine (Phila Pa 1976)*. 2008;33(22):2444–9.

[93] Grupp T, Yue J, Garcia R, et al. Evaluation of Impingement Behaviour in Lumbar Spinal Disc Arthroplasty. *Eur Spine J*. 2015;23:2033–46.

[94] Siskey R, Peck J, Mehta H, et al. Development of a Clinically Relevant Impingement Test method for a Mobile Bearing Lumbar Total Disc Replacement. *Spine J*. 2016;16(9):1133–42.

[95] Rundell S, Day J, Isaza J, et al. Lumbar Total Disc Replacement Impingement Sensitivity to Disc Height Distraction, Spinal Sagittal Orientation, Implant Position, and Implant Lordosis. *Spine (Phila Pa 1976)*. 2012;37(10):E590–8.

[96] Rundell S, Day J, Isaza J, et al. Derivation of Clinically Relevant Boundary Conditions Suitable for Evaluation of Chronic Impingement of Lumbar Total Disk Replacement. *J ASTM Int*. 2011;8(5):73–94.

[97] Choma T, Miranda J, Siskey R, et al. Retrieval Analysis of a ProDisc-L Total Disc Replacement. *J Spinal Disord Tech*. 2009;22(4):290–6.

[98] Semitela A, Fonseca F, Completo A. Experimental Evaluation of Vertebral Strain in Lumbar Total Disc Replacement. *Exp Mech*. 2020;60:119–28.

[99] Marieb E, Wilhelm P, Mallatt J. Bones and Skeletal Tissues. In: Human Anatomy. 7th ed. Glenview, IL: Pearson Education; 2014. p. 123–149.

[100] Kennedy O, Majeska R, Schaffler M. Form and Function of Bone. In: O'Keefe R, Jacobs J, Chu C, Einhorn T, editors. Orthopaedic Basic Science. 4th ed. Rosemont, IL: American Academy of Orthopaedic Surgeouns; 2013. p. 149–183.

[101] Currey J. The Structure of Bone Tissue. In: Bones: Structure and Mechanics. 2nd ed. Princeton, NJ: Princeton University Press; 2002. p. 3–26.

[102] Bartel D, Davy D, Keaveny T. Tissue Mechanics I: Bone. In: Orthopedic Biomechanics: Mechanics and Design in Musculoskeletal Systems. Upper Saddle River, NJ: Pearson Prentice Hall Bioengineering; 2006. p. 71–120.

[103] Currey J. The Mechanical Properties of Bone. In: Bones: Structure and Mechanics. 2nd ed. Princeton, NJ: Princeton University Press; 2002. p. 55–123.

[104] Hernandez C. Cancellous Bone. In: Murphy W, Black J, Hastings G, editors. Handbook of Biomaterial Properties. 2nd ed. New York, NY: Springer Nature; 2016. p. 15–21.

[105] Guo XE. Mechanical Properties of Cortical Bone and Cancellous Bone Tissue. In: Cowin S, editor. Bone Mechanics Handbook. 2nd ed. Boca Raton, FL: CRC Press; 2000. p. 10:1-10:23.

[106] Yang H, Jekir M, Davis M, et al. Effective Modulus of the Human Intervertebral Disc and its Effect on Vertebral Bone Stress. *J Biomech*. 2016;49(7):1134–40.

[107] Yang H, Nawathe S, Fields A, et al. Micromechanics of the Human Vertebral Body for Forward Flexion. *J Biomech*. 2012;45(12):2142–8.

[108] Fields A, Eswaran S, Jekir M, et al. Role of Trabecular Microarchitecture in Whole-Vertebral Body Biomechanical Behavior. *J Bone Miner Res*. 2009;24(9):1523–30.

[109] Bayraktar H, Morgan E, Niebur G, et al. Comparison of the Elastic and Yield Properties of Human Femoral Trabecular and Cortical Bone Tissue. *J Biomech*. 2004;37(1):27–35.

[110] Keaveny T, Guo E, Wachtel E, et al. Trabecular Bone Exhibits Fully Linear Elastic Behavior and Tields at Low Strains. *J Biomech*. 1994;27(9).

[111] Oftadeh R, Perez-Viloria M, Villa-Camacho J, et al. Biomechanics and Mechanobiology of Trabecular Bone: A Review. *J Biomech Eng*. 2015;137(1):1–15.

[112] Keaveny T, Morgan E, Yeh O. Bone Mechanics. In: Kurtz M, editor. The Standard Handbook of Biomedical Enginering and Design. McGraw-Hill; 2004. p. 43.

[113] Fields A, Lee G, Liu S, et al. Influence of Vertical Trabeculae on the Compressive Strength of the Human Vertebra. *J Bone Miner Res*. 2011;26(2):263–9.

[114] Christen P, Ito K, Ellouz R, et al. Bone Remodelling in Humans is Load-Driven But Not Lazy. *Nat Commun*. 2014;5:1–5.

[115] Hughes J, Popp K, Yanovich R, et al. The Role of Adaptive Bone Formation in the Etiology of Stress Fracture. *Exp Biol Med*. 2017;242(9):897–906.

[116] Doube M. The Ellipsoid Factor for Quantification of Rods, Plates, and Intermediate Forms in 3D Geometries. *Front Endocrinol (Lausanne)*. 2015;6(15):1–5.

[117] Salmon P, Ohlsson C, Shefelbine S, et al. Structure Model Index Does Not Measure Rods and Plates in Trabecular Bone. *Front Endocrinol (Lausanne)*. 2015;6(Oct.):1–10.

[118] Niebur G, Feldstein M, Yuen J, et al. High-Resolution Finite Element Models with Tissue Strength Asymmetry Accurately Predict Failure of Trabecular Bone. *J Biomech*. 2000;33(12):1575–83.

[119] Bevill G, Eswaran S, Gupta A, et al. Influence of Bone Volume Fraction and Architecture on Computed Large-Deformation Failure Mechanisms in Human Trabecular Bone. *Bone*. 2006;39(6):1218–25.

[120] Silva M, Wang C, Keaveny T, et al. Direct and Computed Tomography Thickness Measurements of the Human, Lumbar Vertebral Shell and Endplate. *Bone*. 1994;15(4):409–14.

[121] Ritzel H, Amling M, Pösl M, et al. The Thickness of Human Vertebral Cortical Bone and Its Changes in Aging and Osteoporosis: A Histomorphometric Analysis of the Complete Spinal Column from Thirty-Seven Autopsy Specimens. *J Bone Miner Res*. 1997;12(1):89–95.

[122] Mosekilde L. Vertebral Structure and Strength In Vivo and In Vitro. *Calcif Tissue Int*.

1993;53(Suppl. 1):121–6.

[123] Sandino C, McErlain D, Schipilow J, et al. The Poro-Viscoelastic Properties of Trabecular Bone: A Micro Computed Tomography-Based Finite Element Study. *J Mech Behav Biomed Mater*. 2015;44:1–9.

[124] Verhulp E, van Rietbergen B, Müller R, et al. Indirect Determination of Trabecular Bone Effective Tissue Failure Properties Using Micro-Finite Element Simulations. *J Biomech*. 2008;41(7):1479–85.

[125] Ladd A, Kinney J, Haupt D, et al. Finite-Element Modeling of Trabecular Bone: Comparison with Mechanical Testing and Determination of Tissue Modulus. *J Orthop Res*. 1998;16(5):622–8.

[126] Hou F, Lang S, Hoshaw S, et al. Human Vertebral Body Apparent and Hard Tissue Stiffness. *J Biomech*. 1998;31(11):1009–15.

[127] Issever A, Walsh A, Lu Y, et al. Micro-Computed Tomography Evaluation of Trabecular Bone Structure on Loaded Mice Tail Vertebrae. *Spine (Phila Pa 1976)*. 2003;28(2):123–8.

[128] Keaveny T, Morgan E, Niebur G, et al. Biomechanics of Trabecular Bone. *Annu Rev Biomed Eng*. 2001;3:307–333.

[129] Eswaran S, Gupta A, Keaveny T. Locations of Bone Tissue at High Risk of Initial Failure During Compressive Loading of the Human Vertebral Body. *Bone*. 2007;41(4):733–9.

[130] Fields A, Lee G, Keaveny T. Mechanisms of Initial Endplate Failure in the Human Vertebral Body. *J Biomech*. 2010;43(16):3126–31.

[131] Hughes T. The Finite Element Method: Linear Static and Dynamic Finite Element Analysis. Mineola, NY: Dover Publications; 2000.

[132] Niebur G, Yuen J, Hsia A, et al. Convergence Behavior of High- Resolution Finite Element Models of Trabecular Bone. *J Biomech Eng*. 1999;121(6):629–35.

[133] Ladd A, Kinney J. Numerical Errors and Uncertainties in Finite-Element Modeling of Trabecular Bone. *J Biomech*. 1998;31(10):941–5.

[134] Adams M, Bayraktar H, Keaveny, et al. Ultrascalable Implicit Finite Element Analysis in Solid Mechanics with Over Half a Billion Degrees of Freedom. In: Proceedings of the ACM/IEEE SC2004 Conference: High Performance Networking and Computing. 2004. p. 1–15.

[135] Nawathe S, Yang H, Fields A, et al. Theoretical Effects of Fully Ductile Versus Fully Brittle Behaviors of Bone Tissue On the Strength of the Human Proximal Femur and Vertebral Body. *J Biomech*. 2015;48(7):1264–9.

[136] Texas Advanced Computing Cetner at the University of Texas at Austin. System Overview [Internet]. Stampede2 User Guide. p. 1–24. Available from: https://portal.tacc.utexas.edu/user-guides/stampede2

[137] Bertagnoli R, Yue J, Nanieva R, et al. Lumbar Total Disc Arthroplasty in Patients Older Than 60 Years of Age: A Prospective Study of the ProDisc Prosthesis with 2-year Minimum Follow-Up Period. *J Neurosurg Spine*. 2006;4(2):85–90.

[138] Reilly D, Burstein A. The Elastic and Ultimate Properties of Compact Bone Tissue. *J Biomech*. 1975;8(6):393–405.

[139] Auerbach J, Ballester C, Hammond F, et al. The Effect of Implant Size and Device Keel on Vertebral Compression Properties in Lumbar Total Disc replacement. *Spine J*. 2010;10(4):333–40.

[140] Tan J, Bailey C, Dvorak M, et al. Interbody Device Shape and Size Are Important to Strengthen the Vertebra-Implant Interface. *Spine (Phila Pa 1976)*. 2005;30(6):638–44.

[141] Legrand E, Chappard D, Pascaretti C, et al. Trabecular Bone Microarchitecture, Bone Mineral Density, and Vertebral Fractures in Male Osteoporosis. *J Bone Miner Res*. 2000;15(1):13–9.

[142] Eswaran S, Gupta A, Adams M, et al. Cortical and Trabecular Load Sharing in the Human Vertebral Body. *J Bone Miner Res*. 2006;21(2):307–14.

[143] Jaramillo J, Yue J. Disc Space Preparation Techniques for Lumbar Disc Arthroplasty. In: Yue J, Bertagnoli R, McAfee P, An H, editors. Motion Preservation Surgery of the Spine. Philadelphia, PA: Saunders; 2008. p. 305–8.

[144] Geisler F. Surgical Technique of Lumbar Artificial Disc Replacement with the Charité Artificial Disc. *Neurosurgery*. 2005;56:46–57.

[145] Dey D, Rothenberg E, Sundh V, et al. Height and Body Weight in Elderly Adults: A 21-Year Population Study on Secular Trends and Related Factors in 70-Year-Olds. *J Gerontol*. 2001;56A(12):780–4.

[146] Dreischarf M, Shirazi-Adl A, Arjmand N, et al. Estimation of Loads on Human Lumbar Spine: A Review of In Vivo and Computational Model Studies. *J Biomech*. 2016;49(6):833–45.

[147] Adams M, Pollintine P, Tobias J, et al. Intervertebral Disc Degeneration Can Predispose to Anterior Vertebral Fractures in the Thoracolumbar Spine. *J Bone Miner Res*. 2006;21(9).

[148] Rohlmann A, Claes L, Bergmann G, et al. Comparison of Intradiscal Pressures and Spinal

Fixator Loads for Different Body Positions and Exercises. *Ergonomics*. 2001;44(8):781–94.

[149] Bevill G, Eswaran S, Farahmand F, et al. The Influence of Boundary Conditions and Loading Mode on High-Resolution Finite Element-Computed Trabecular Tissue Properties. *Bone*. 2009;44(4):573–8.

[150] Dooris A, Goel V, Grosland N, et al. Load-Sharing Between Anterior and Posterior Elements in a Lumbar Motion Segment Implanted with an Artificial Disc. *Spine (Phila Pa 1976)*. 2001;26(6):E122–9.

[151] Pruitt L, Chakravartula A. Orthopedics. In: Mechanics of Biomaterials. New York, NY: Cambridge University Press; 2011. p. 416–76.

[152] Gstoettner M, Denise H, Liebensteiner M, et al. Footprint Mismatch in Lumbar Total Disc Arthroplasty. *Eur Spine J*. 2008;17:1470–5.

[153] ASTM. ASTM F2423 −11: Standard Guide for Functional, Kinematic, and Wear Assessment of Total Disc Prostheses 1. *ASTM Int*. 2016.

[154] Fields A, Nawathe S, Eswaran S, et al. Vertebral Fragility and Structural Redundancy. *J Bone Miner Res*. 2012;27(10):2152–8.

[155] Iatridis J, Setton L, Weidenbaum M, et al. Alterations in the Mechanical Behavior of the Human Lumbar Nucleus Pulposus with Degeneration and Aging. *J Orthop Res*. 1997;15:318–22.

[156] Jiang G, Luo J, Pollintine P, et al. Vertebral Fractures In the Elderly May Not Always Be "Osteoporotic." *Bone*. 2010;47(1):111–6.

[157] Farooq N, Park J, Pollintine P, et al. Can Vertebroplasty Restore Normal Load-Bearing to Fractured Vertebrae? *Spine (Phila Pa 1976)*. 2005;30(15):1723–30.

[158] Bonnheim N, Verbiest V, Wu T, et al. Total Disc Replacement Implants Affect Load-Transfer Throughout the Vertebral Body With and Without Endplates. In: Orthopedic Research Society Conference. Austin, TX; 2019.

[159] Moon S, Yoder J, Wright A, et al. Evaluation of Intervertebral Disc Cartilaginous Endplate Structure Using Magnetic Resonance Imaging. *Eur Spine J*. 2013;22(8):1820–8.

[160] Berg-Johansen B, Han M, Fields A, et al. Cartilage Endplate Thickness Variation Measured by Ultrashort Echo-Time MRI is Associated with Adjacent Disc Degeneration. *Spine (Phila Pa 1976)*. 2018;43(10):E592–600.

[161] White A, Panjabi M. Physical Properties and Functional Biomechanics of the Spine. In: Clinical Biomechanics of the Spine. 2nd ed. Philadelphia, PA: J.B. Lippincott Company;

1990. p. 1–83.

[162] Choi K, Goldstein S. A Comparison of the Fatigue Behavior of Human Trabecular and Cortical Bone Tissue. *J Biomech*. 1992;25(12):1371–81.

[163] van Ooij A, O C, Verbout A. Complications of Artificial Disc Replacement: A Report of 27 Patients with the SB Charité Disc. *J Spinal Disord Tech*. 2003;16(4):369–83.

[164] de Haro Estrada J, Fernandez J, Garnier J, et al. Bilateral Fracture of L5 Pedicles in a Patient with Total Disc Replacement of L5–S1: A Case Report. *Coluna/Columna*. 2014;13(2):153–5.

[165] Yoder J, Auerbach J, Maurer P, et al. Augmentation Improves Human Cadaveric Vertebral Body Compression Mechanics for Lumbar Total Disc Replacement. *Spine (Phila Pa 1976)*. 2010;35(9):E325–31.

[166] Bonnheim N, Keaveny T. Load-Transfer in the Human Vertebral Body Following Lumbar Total Disc Arthroplasty: Effects of Implant Size and Stiffness in Axial Compression and Forward Flexion. *JOR Spine*. 2020;3(e1078):1–10.

[167] Yue J. Considerations for Spinal Arthroplasty in Elderly and Osteoporotic Patients. In: Yue J, Bertagnoli R, McAfee P, An H, editors. Motion Preservation Surgery of the Spine. Philadelphia, PA: Elsevier Inc.; 2008. p. 720–724.

[168] Closkey R, P R, Lee C, et al. Mechanics of Interbody Spinal Fusion: Analysis of Critical Bone Graft Area. *Spine (Phila Pa 1976)*. 1993;18(8):1011–5.

[169] Ward R, Roberts C, Bencardino J, et al. ACR Appropriateness Criteria® Osteoporosis and Bone Mineral Density. *J Am Coll Radiol*. 2017;14(5):S189–202.

[170] Gornet M, Burkus J, Dryer R, et al. Lumbar Disc Arthroplasty with MAVERICK Disc Versus Stand-Alone Interbody Fusion: A Prospective, Randomized, Controlled, Multicenter Investigational Device Exemption Trial. *Spine (Phila Pa 1976)*. 2011;36(25):E1600–11.

[171] Blumenthal S, McAfee P, Guyer R, et al. A Prospective, Randomized, Multicenter Food and Drug Administration Investigational Device Exemptions Study of Lumbar Total Disc Replacement With the CHARITÉ Artificial Disc Versus Lumbar Fusion: Part 1: Evaluation of Clinical Outcomes. *Spine (Phila Pa 1976)*. 2005;30(14):1565–1575.

[172] Sasso R, Foulk D, Hahn M. Prospective, Randomized Trial of Metal-on-Metal Artificial Lumbar Disc Replacement: Initial Results for Treatment of Discogenic Pain. *Spine (Phila Pa 1976)*. 2008;33(2):123–31.

[173] McAfee P. The Indications for Lumbar and Cervical Disc Replacement. *Spine J*. 2004;4(6 Suppl.):S177–81.

[174] Hasegawa K, Abe M, Washio T, et al. An Experimental Study on the Interface Strength Between Titanium Mesh Cage and Vertebra in Reference to Vertebral Bone Mineral Density. *Spine (Phila Pa 1976)*. 2001;26(8):957–63.

[175] Schindelin J, Arganda-Carreras I, Frise E, et al. Fiji: An Open-Source Platform for Biological-Image Analysis. *Nat Methods*. 2012;9(7):676–82.

[176] Doube M, Kłosowski M, Arganda-Carreras I, et al. BoneJ: Free and Extensible Bone Image Analysis in ImageJ. *Bone*. 2010;47(6):1076–9.

[177] Pruitt L, Chakravartula A. Metals for Medical Implants. In: Mechanics of Biomaterials: Fundamental Principles for Implant Design. New York, NY: Cambridge University Press; 2011. p. 26–69.

[178] Nawathe S, Akhlaghpour H, Bouxsein M, et al. Microstructural Failure Mechanisms in the Human Proximal Femur for Sideways Fall Loading. *J Bone Miner Res*. 2014;29(2):507–15.

[179] Yue J, Lawrence J. Indications and Contraindications for Lumbar Nonfusion Surgery. In: Yue J, Bertagnoli R, McAfee P, An H, editors. Motion Preservation Surgery of the Spine. Philadelphia, PA: Elsevier Inc.; 2008. p. 75–9.

[180] Keaveny T, Clarke B, Cosman F, et al. Biomechanical Computed Tomography Analysis (BCT) for Clinical Assessment of Osteoporosis. *Osteoporos Int*. 2020;31(6):1025–48.

[181] Zigler J, Delamarter R, Spivak J, et al. Results of the Prospective, Randomized, Multicenter Food and Drug Administration Investigational Device Exemption Study of the ProDisc®-L Total Disc Replacement Versus Circumferential Fusion for the Treatment of 1-Level Degenerative Disc Disease. *Spine (Phila Pa 1976)*. 2007;32(11):1155–62.

[182] Berg S, Tullberg, Branth B, et al. Total Disc Replacement Compared to Lumbar Fusion: A Randomised Controlled Trial with 2-Year Follow-Up. *Eur Spine J*. 2009;18(10):1512–9.

[183] Delamarter R, Bae H, Pradhan B. Clinical Results of ProDisc-II Lumbar Total Disc Replacement: Report From the United States Clinical Trial. *Orthop Clin North Am*. 2005;36(3 Spec. Iss.):301–13.

[184] World Health Organization. Scientific Group on the Assessment of Osteoporosis At Primary Health Care Level [Internet]. Summary Meeting Report. Brussels, Belgium; 2004. Available from: http://www.who.int/chp/topics/Osteoporosis.pdf

[185] Guyer R, McAfee P, Hochschuler S, et al. Prospective Randomized Study of the Charité Artificial Disc: Data From Two Investigational Centers. *Spine J*. 2004;4(Suppl. 6):S252–9.

[186] Steffen T, Tsantrizos A, Aebi M. Effect of Implant Design and Endplate Preparation on the Compressive Strength of Interbody Fusion Constructs. *Spine (Phila Pa 1976)*. 2000;25(9):1077–84.

[187] Kitzen J, Schotanus M, van Kuijk S, et al. Long-Term Clinical Outcome of the Charité III Total Lumbar Disc Replacement. *Eur Spine J*. 2020;29(7):1527–35.

[188] Lewis G. Properties of Acrylic Bone Cement: State of the Art Review. *J Biomed Mater Res*. 1997;38(2):155–82.

[189] Montgomery D, Runger G. Multiple Linear Regression. 5th ed. Applied Statistics and Probability for Engineers. Hoboken, NJ: John Wiley & Sons; 2011. 502 p.

[190] Roschger P, Gupta H, Berzlanovich A, et al. Constant Mineralization Density Distribution in Cancellous Human Bone. *Bone*. 2003;32(3):316–23.

[191] van Der Linden J, Birkenhäger-Frenkel D, Verhaar J, et al. Trabecular Bone's Mechanical Properties are Affected by its Non-Uniform Mineral Distribution. *J Biomech*. 2001;34(12):1573–80.

[192] Rand T, Seidl G, Kainberger F, et al. Impact of Spinal Degenerative Changes on the Evaluation of Bone Mineral Density with Dual Energy X-Ray Absorptiometry (DXA). *Calcif Tissue Int*. 1997;60(5):430–3.

[193] Lee C, Chung S, Oh S, et al. Significance of Angular Mismatch Between Vertebral Endplate and Prosthetic Endplate in Lumbar Total Disc Replacement. *J Spinal Disord Tech*. 2011;24(3):183–8.

[194] Kopperdahl D, Morgan E, Keaveny T. Quantitative Computed Tomography Estimates of the Mechanical Properties of Human Vertebral Trabecular Bone. *J Orthop Res*. 2002;20(4):801–5.

7. Appendix

7.1 Assessing the impact of a higher fidelity implant model on load-sharing outcomes (Chapter 2)

To assess the impact of footplate protrusions (such as spikes or teeth to facilitate fixation into the vertebral body) on the load-sharing outcomes, a sensitivity study was conducted in which six 1.5 mm wide by 3 mm deep cylindrical protrusions were added to the medium size, metallic implant loaded in compression and flexion. The protrusions were added in an elliptical pattern resembling that of the Charité implant. Relative to the medium size, metallic implant without protrusions, the cortical load-fraction varied by a maximum of 1.9% at any axial location and the high-risk tissue volume varied by a maximum of 2.7% at any A/P location (Figure 7–1). The 98th percentile of axial stress varied by a maximum of 1.8% and the amount of bone tissue with von Mises stress changes greater than ± 50% varied by a maximum of 1.0%. Thus, the addition of small protrusions resembling the spikes or teeth present on clinically used implants should have an insignificant effect on the reported results and would not alter the conclusions.

7.2 Assessing the sensitivity of load-sharing outcomes to uncertainties in bone tissue elastic modulus (Chapter 2)

To account for uncertainty in the assumption of bone tissue material properties (elastic modulus of 10.3 GPa, Poisson's ratio 0.30), a sensitivity study was conducted using the intact model in which bone tissue was modeled using another possible physiologic value of material properties (elastic modulus 18.5 GPa, Poisson's ratio 0.30 [142]). The load-sharing outcomes were insensitive to the choice of bone tissue material properties over the range tested. The cortical load-fraction varied by a maximum of 0.5% and the high-risk tissue volume varied by a maximum of 1% at any axial location (Figure 7–1). Thus, the error of the load-sharing estimates with respect to the choice of bone tissue elastic modulus are negligible.

7.3 Assessing the impact of a higher fidelity implant model on the maximum stress levels (Chapter 3)

Using the same methodology as described in section 7.1, a sensitivity study was conducted on a higher fidelity implant model to assess the impact of footplate protrusions on the maximum stress outcome. Here, a specimen with an intermediate bone volume fraction (BV/TV = 0.106) was loaded via an implant in axial compression and forward flexion using the native micro-CT resolution of 37 μm. Relative to models loaded in the same way but without implant protrusions, the high stress level varied by a maximum of 4% at any axial location—A, B, or C—and the high-risk tissue volume varied by a maximum 0.1% at any A/P location in the vertebral body. Thus, the addition of small protrusions resembling the spikes or teeth present on clinically used implants should have an insignificant effect on the reported results and would not alter the conclusions.

7.4 Assessing the sensitivity of the maximum stress levels to uncertainties in bone tissue elastic modulus (Chapter 3)

To account for uncertainty in our assumption of bone tissue material properties (elastic modulus of 10.3 GPa, Poisson's ratio of 0.30), we performed a sensitivity study on one specimen using another possible physiologic value of bone tissue material properties (elastic modulus 18.5 GPa, Poisson's ratio of 0.30 [142]). The specimen had an intermediate bone volume fraction (BV/TV = 0.106) and was loaded via a TDA implant in uniform compression. For the constant 800 N applied force, the stress outcomes were insensitive to the choice of bone tissue material properties: the high stress level varied by a maximum of 2.7 MPa at any axial location (A, B, or C) and the high-risk tissue volume varied by a maximum of 0.1% at any A/P location in the vertebral body. Thus, the error of our outcomes with respect to the choice of bone tissue elastic modulus are negligible.

7.5 Estimating QCT-measured volumetric bone mineral density from micro-CT-measured trabecular bone volume fraction (Chapter 3)

To estimate the QCT-measured volumetric bone mineral density from the micro-CT-measured bone volume fraction, I first calculated the apparent density (ρ_{app}) of the internal trabecular region used to measure bone volume fraction by multiplying the bone volume fraction by the assumed wet-tissue density (ρ_{tissue} = 1.9 g/cm^3) [105]. Then, I used linear regression data derived from Kopperdahl et al [194] (found in their Table 1) relating apparent density to QCT-measured volumetric bone mineral density (vBMD g/cm^3) measured using a hydroxyapatite calibration phantom (vBMD = $0.6594 \times \rho_{app}$ - 0.0193).

7.6 Assessing the impact of a higher fidelity implant model on yield strength predictions (Chapter 4)

To assess the impact of footplate protrusions (such as spikes or teeth to facilitate fixation into the vertebral body) on the yield strength outcomes, a sensitivity study was conducted in which six 1.5 mm wide by 3 mm deep cylindrical protrusions were added to the implant footplate of one model (BV/TV = 0.120), then loaded in compression and flexion-induced impingement. The protrusions were added in an elliptical pattern resembling that of the Charité implant.

For the TDA implant loaded in compression, the difference in yield strength between a footplate with and without protrusions was 1.7% (31 N). For the TDA implant loaded in flexion-induced impingement, this difference was 2.2% (32 N). Therefore, the difference in yield strength caused by the addition of footplate protrusions was small and would not alter the conclusions.

7.7 Assessing the impact of finite element size on yield strength predictions (Chapter 4)

To assess the sensitivity of the yield strength prediction to the finite element edge length, a sensitivity study was conducted on a single bone loaded by a TDA implant in compression (BV/TV = 0.120). The yield strength predictions were compared between a model using element edge-lengths lengths of 37 μm (the native scan resolution) versus using a coarsened model with 74 μm element edge lengths. The difference in computed yield strengths between these models

was 0.3% (5 N), suggesting that modeling the bone at the native scan resolution would not appreciably alter yield strength predictions when load is applied via a TDA implant.

7.8 Assessing the impact of modeling an intervertebral disc instead of PMMA on yield strength predictions (Chapter 4)

To assess the impact of loading the vertebral body via a intervertebral disc-like material opposite a TDA implant instead of potting the vertebral body in PMMA, a sensitivity study was conducted in which the solid layers previously defined as PMMA were re-defined to have the elastic properties of a material with the effective (homogenized) elastic properties resembling an intervertebral (elastic modulus 8 MPa, Poisson ratio 0.45 [106]).

Relative to the TDA-bone-PMMA model, the TDA-bone-disc model exhibited a reduction in yield strength of 9.8% (307 N). While this is not a negligible change, it's much lower than the effect of the implant on yield strength (reduction of 33–82%) and would therefore not likely alter the conclusions.

7.9 Experimental data supporting the validity of the micro-CT-based finite element approach

Extensive experimental data collected by others support the accuracy of yield strength predictions of human bone using the finite element approach employed here. For example, Fields et al [154] accurately predicted the experimentally-measured strength of n = 12 elderly thoracic human vertebrae loaded to failure in compression via PMMA ($R^2 = 0.85$ with Y = X type behavior) using the same finite element approach—including hexahedral finite elements converted from thresholded micro-CT data, homogenous isotropic elastic tissue material assumptions, an elasto-plastic constitutive model, the inclusion of geometric along with material nonlinearities, tissue-level tension-compression strength asymmetry, and solved using the same parallel finite element solver (Figure 7–2A). Separately, this same finite element approach accurately predicted the experimentally measured strength of n = 12 proximal human femurs from elderly cadavers ($R^2 = 0.94$ with Y = X type behavior [178], Figure 7–2B), as well as n = 54 human trabecular bone cores from across anatomic sites loaded in compression ($R^2 = 0.98$) and tension ($R^2 = 0.99$) [119] (Figure 7–2C, D). In combination, these data indicate a high-level of accuracy in bone strength predictions for this finite element approach under the unique set of assumptions used; indeed, the accuracy of this method across anatomic sites and variations in bone morphometry indicates that the dominant structural mechanisms in the bone itself are well-captured.

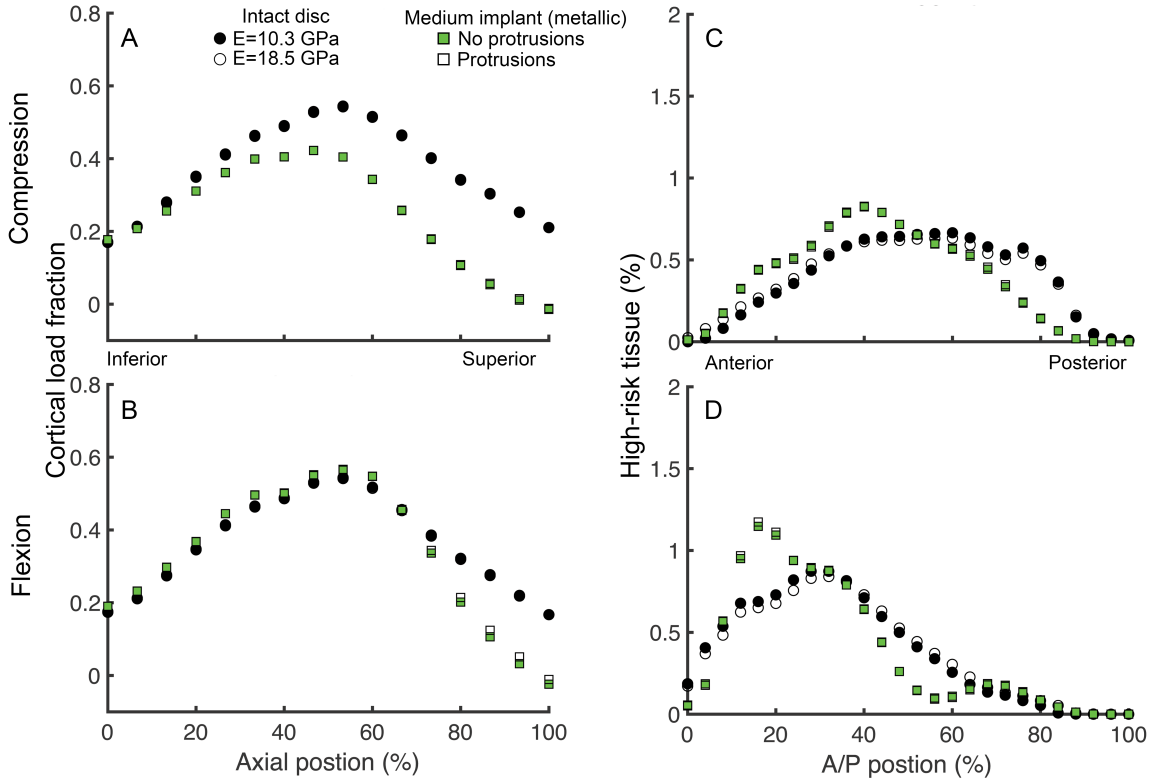

Figure 7–1. The cortical load fraction (left) and high-risk tissue volume (right) were not sensitive to the choice of tissue material properties within a realistic physiologic range or the addition of small implant protrusions.

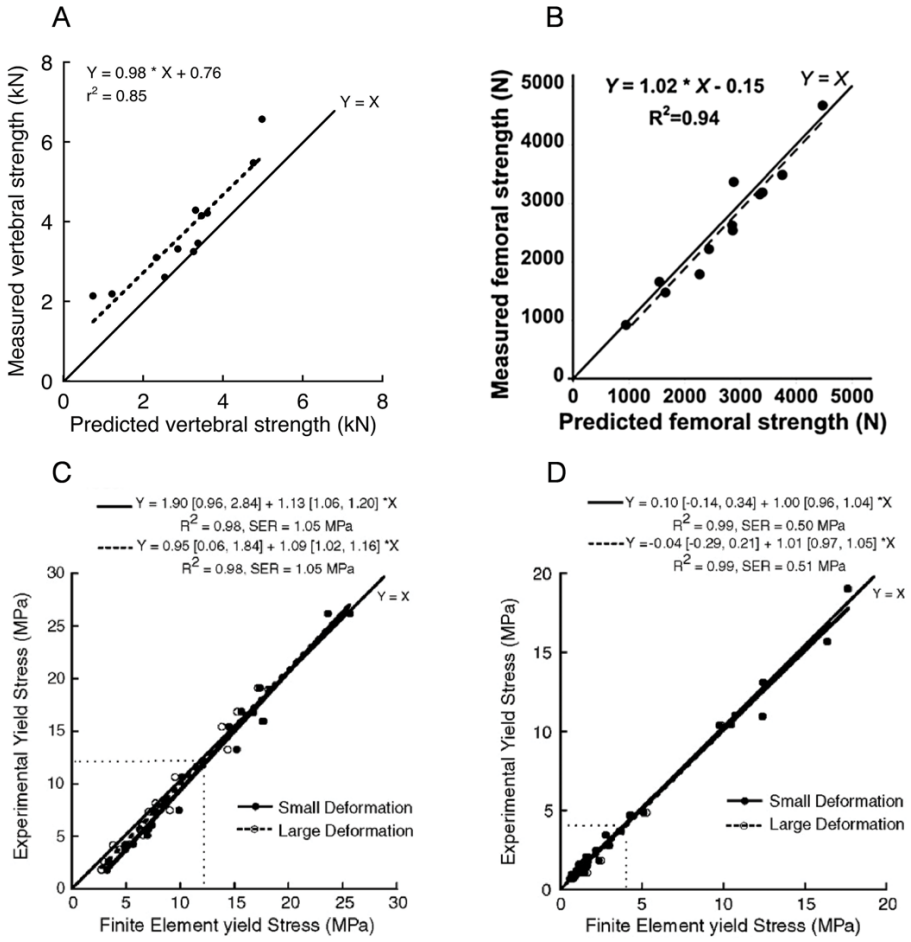

Figure 7–2. Supporting data collected by others demonstrating that the specialized micro-CT based finite element approach used here accurately predicted experimentally-measured strength of (A) n = 12 human thoracic vertebrae [154]; (B) n = 12 human proximal femurs [178]; and n = 54 human trabecular bone cores from across anatomic sites tested in compression (C) and tension (D) [119].